SILICON OXIDATION BY ATOMIC AND MOLECULAR OXYGEN

by

Maja Kisa

Dipl. Ing. Inorganic Chemical Engineering, University of Belgrade, 1998

Submitted to the Graduate Faculty of

the School of Engineering in partial fulfillment

of the requirements for the degree of

Master of Science in Materials Science and Engineering

University of Pittsburgh

2004

UNIVERSITY OF PITTSBURGH

SCHOOL OF ENGINEERING

This thesis was presented

by

Maja Kisa

It was defended on

February 3, 2004

and approved by

Dr. J. Blachere, Associate Professor Emeritus, Materials Science and Engineering

Dr. J. Wiezorek, Assistant Professor, Materials Science and Engineering

Thesis Advisor: Dr. J.C. Yang, Assistant Professor, Materials Science and Engineering

SILICON OXIDATION BY ATOMIC AND MOLECULAR OXYGEN

Maja Kisa, MS

University of Pittsburgh, 2004

Atomic oxygen is the most hazardous species of molecules present in the Low Earth Orbit causing failure of the material in space. This study was undertaken to examine the differences in the oxidation of silicon by molecular and atomic oxygen. Hypotheses about the effects of reactive atomic oxygen on the oxidation mechanism of silicon and formed oxide microstructure are presented. The oxides created with atomic and molecular oxygen were studied via Rutherford Backscattering (RBS), High-Resolution Transmission Electron Microscopy (HRTEM), Selected Area Electron Diffraction (SAED), Electron-Energy Loss Spectroscopy (EELS), X-ray Photoelectron Scattering (XPS) and Atomic Force Microscopy (AFM).

The results obtained in the experiments are discussed and the possible effects of atomic oxygen on the oxidation mechanism and microstructure formation are inferred. An oxidation model based on thermionic emission is presented as a model for the oxidation by atomic oxygen.

TABLE OF CONTENTS

LIST OF TABLES .... **VII**

LIST OF FIGURES .... **VIII**

PREFACE .... **XII**

1.0 INTRODUCTION **1**

2.0 BACKGROUND **3**

2.1 LOW EARTH ORBIT (LEO) ENVIRONMENT 3

2.2 MATERIALS PROTECTION FROM ATOMIC OXYGEN 4

2.3 WHAT IS KNOWN ABOUT ATOMIC OXYGEN? 7

2.4 SILICON OXIDATION 11

2.4.1 Deal –Grove Oxidation Model 12

2.4.2 Other Alternative Models of Oxidation 16

3.0 STATEMENT OF OBJECTIVES **28**

4.0 EFFECT OF 5eV ATOMIC OXYGEN ON Si OXIDATION **29**

5.0 SILICON-SINGLE CRYSTAL OXIDATION-EXPERIMENTAL PROCEDURE **36**

5.1 ATOMIC OXYGEN SOURCES 36

5.1.1 Laser Detonation Source (LDS) 36

5.1.2 O_2^+ Source 38

5.2 SILICON SURFACE CLEANING 39

5.3 Si - SINGLE CRYSTAL OXIDATION IN LDS 41

5.3.1 Native oxide removal procedure prior to oxidation 41

5.3.2 Oxidation conditions 42

5.4 Si- SINGLE CRYSTAL OXIDATION BY O_2 42
5.4.1 Native oxide removal procedure prior to oxidation 42
5.4.2 Oxidation conditions 43
5.5 Si -SINGLE CRYSTAL OXIDATION IN O_2^+SOURCE 44
5.5.1 Native oxide removal procedure prior to oxidation 44
5.5.2 Oxidation conditions 44

6.0 CHARACTERIZATION TECHNIQUES AND RESULTS 46
6.1 RUTHERFORD BACKSCATTERING SPECTROMETRY (RBS) 46
6.1.1 Rutherford Backscattering Spectroscopy (RBS)-Results 48
6.2 TRANSMISSION ELECTRON MICROSCOPY (TEM) 51
6.2.1 Electron-Specimen Interactions 51
6.2.2 TEM components 56
6.2.3 Major TEM techniques 60
6.2.4 TEM Sample Preparation-Experimental 60
6.3 HIGH RESOLUTION TRANSMISSION ELECTRON MICROSCOPY (HRTEM) 61
6.3.1 High Resolution Transmission Electron Microscopy (HRTEM) - Results 63
6.4 SELECTED AREA ELECTRON DIFFRACTION (SAED) 71
6.4.1 Selected Area Electron Diffraction (SAED) – Results 74
6.5 ELECTRON ENERGY LOSS SPECTROSCOPY (EELS) 76
6.5.1 Scanning Transmission Electron Microscopy (STEM) Spectrum Imaging (SI) 78
6.5.2 Electron Energy Loss Spectrum 79
6.5.3 Electron Loss Near Edge fine Structure (ELNES) 83
6.5.4 EELS Spectra Processing 86
6.5.5 EELS Acquisition Conditions and Spectra Processing-Experimental 90
6.5.6 Electron Energy Loss Spectroscopy (EELS) – Results 92
6.5.6.1 Spectrum Imaging –Results 92
6.5.6.2 $SiL_{2,3}$ Energy Loss Near Edge Structure (ELNES) -Results 98
6.5.6.3 OK Energy Loss Near Edge Structure (ELNES) -Results 106

6.5.6.4 EELS Quantification -Results 108

6.6 ATOMIC FORCE MICROSCOPY (AFM) 110

6.6.1 Atomic Force Microscopy (AFM) – Results 111

6.7 X-RAY PHOTOELECTRON SPECTROSCOPY (XPS) 116

6.7.1 X-Ray Photoelectron Spectroscopy (XPS) - Results 117

7.0 DISCUSSION 123

8.0 CONCLUSIONS 134

9.0 FUTURE WORK 137

BIBLIOGRAPHY 138

LIST OF TABLES

Table 1. SiO_2 phases………………………………………………………………………. 33

Table 2. Experimental conditions…………………………………………………………….. 45

Table 3. Calculated oxide thicknesses using RBS spectra……………………………………….50

Table 4. Mean square roughness values as determined by AFM……………………………… 115

LIST OF FIGURES

Figure 1. Exterior surface of a spacecraft in the cross-section view 5

Figure 2. Adsorption probabilities for atomic and molecular oxygen (a) for zero oxygen coverages as a function of substrate temperature, and (b) for different oxygen coverages on different substrate temperatures [8]. 7

Figure 3. Coverage dependence on exposure for atomic and molecular oxygen on Si(100) substrate at 300K [9]. 9

Figure 4. Oxide thickness versus fluence for atomic oxygen oxidation of H-terminated Si(100) at 297K . The hyperthermal atomic oxygen beam had three different translation energies: 1.6eV, 3.6eV and 4.6eV [10]. 10

Figure 5. Model for silicon oxidation [13]... 13

Figure 6. Schematic of the ion removal from the metal surface [20]. 20

Figure 7. Schematic drawing of the charged species moving during thermal oxidation [21]. 21

Figure 8. Schematic representation of fluxes for thermionic emission model [28]..................... 25

Figure 9. Parameters that define short and intermediate range of order [35]. 31

Figure 10. Schematic of Laser Detonation Atomic Oxygen Source... 37

Figure 11. Schematic of O_2^+ source. 38

Figure 12. RBS spectra from Tandetron accelerator recorded from a) Si(100) oxidized in LDS b) Si(111) oxidized in LDS c) Si(100) oxidized in O_2^+ source and d) Si(100) oxidized in O_2, used for calibration. 49

Figure 13. Possible electron-matter interactions [59]. 52

Figure 14. Schematic of scattering process [60]. 53

Figure 15. Block diagram of the main components of TEM with STEM capabilities [61]. 57

Figure 16. Cross-sectional HRTEM micrographs of the silicon oxide layer formed on Si(100) oxidized by a) atomic oxygen b) molecular oxygen. 63

Figure 17. 3D view of cross-sectional HRTEM micrographs of the silicon oxide layer formed on Si(100) oxidized by a) atomic oxygen b) molecular oxygen 64

Figure 18. Intensity profiles and Fourier transforms obtained from cross-sectional HRTEM micrographs of the silicon oxide layer formed on Si(100) oxidized by atomic oxygen. 65

Figure 19. Intensity profiles and Fourier transforms obtained from cross-sectional HRTEM micrographs of the silicon oxide layer formed on Si(100) oxidized by molecular oxygen.. 66

Figure 20. Cross-sectional HRTEM micrographs of the silicon oxide layer formed on Si(111) oxidized by a) atomic oxygen b) molecular oxygen. 67

Figure 21. 3D view of cross-sectional HRTEM micrographs of the silicon oxide layer formed on Si(111) oxidized by a) atomic oxygen b) molecular oxygen. 68

Figure 22. Intensity profiles and Fourier transforms obtained from cross-sectional HRTEM micrographs of the silicon oxide layer formed on Si(111) oxidized by atomic oxygen. 69

Figure 23. Intensity profiles and Fourier transforms obtained from cross-sectional HRTEM micrographs of the silicon oxide layer formed on Si(111) oxidized by molecular oxygen.. 70

Figure 24. Ewald sphere construction [60]. 72

Figure 25. (a)Plan-view HRTEM micrographs and corresponding SAED pattern of the silicon oxide layer formed on Si(100) oxidized by molecular oxygen (b) Intensity profile taken across the diffraction pattern. 74

Figure 26. (a) Plan-view HRTEM micrographs of the silicon oxide layer formed on Si(100) oxidized by atomic oxygen (b) Intensity profile taken across the diffraction pattern. 75

Figure 27. (a) Plan-view HRTEM micrographs of the silicon oxide layer formed on Si(111) oxidized by atomic oxygen (b) Intensity profile taken across the diffraction pattern. 75

Figure 28. STEM analyses with Spectrum Imaging (SI). 79

Figure 29. Characteristic EELS spectrum of SiO_2 as-acquired containing the most intense zero-loss peak, low-loss and high-loss region characterized with core-loss edges 82

Figure 30. Molecular orbital (MO) diagram for SiO_2. 84

Figure 31. As - recorded EELS spectrum and background fitting to $SiL_{2,3}$ edge. 91

Figure 32. Overall background subtracted EELS spectra obtained from Si(100) oxidized by atomic oxygen. 93

Figure 33. Overall background subtracted EELS spectra obtained from Si(100) oxidized by molecular oxygen. 94

Figure 34. Characteristic core-loss ionization $SiL_{2,3}$ edge for Si(100) oxidized by atomic oxygen. 95

Figure 35. Characteristic core-loss ionization OK edge for Si(100) oxidized by atomic oxygen. 95

Figure 36. Characteristic core-loss ionization $SiL_{2,3}$ edge for Si(100) oxidized by molecular oxygen. 96

Figure 37. Characteristic core-loss ionization OK edge for Si(100) oxidized by molecular oxygen. 97

Figure 38. Si(100) oxidized by molecular oxygen (a) Annular dark field image (b) $SiL_{2,3}$ background stripped edge recorded in Si bulk, Si/SiO_2 interface and oxide bulk. 98

Figure 39. Si(100) oxidized by atomic oxygen (a) Annular dark field image (b) $SiL_{2,3}$ background stripped edge recorded in Si bulk, Si/SiO_2 interface and oxide bulk. 99

Figure 40. Si(111) oxidized by atomic oxygen (a) Annular dark field image (b) $SiL_{2,3}$ background stripped edge recorded in Si bulk, Si/SiO_2 interface and oxide bulk. 99

Figure 41. ELNES comparison of $SiL_{2,3}$ edges of Si(100) oxidized by atomic and molecular and Si(111) oxidized by atomic oxygen with results of Garvie et al. 101

Figure 42. $SiL_{2,3}$ ELNES obtained from Si(100) oxidized by molecular oxygen. 103

Figure 43. $SiL_{2,3}$ ELNES obtained from Si(100) oxidized by atomic oxygen. 103

Figure 44. $SiL_{2,3}$ ELNES obtained from Si(111) oxidized by atomic oxygen. 104

Figure 45. $SiL_{2,3}$ EELS spectra obtained from the Si/SiO_2 interface by Batson. The probe positions are indicated on the left micrograph [84]. 104

Figure 46. OK ELNES obtained in the bulk oxide and at the Si/oxide interface from Si(100) oxidized by molecular oxygen. 106

Figure 47. OK ELNES obtained in the bulk oxide and at the Si/oxide interface from Si(100) oxidized by atomic oxygen. 107

Figure 48. OK ELNES obtained in the bulk oxide and at the Si/oxide interface from Si(111) oxidized by atomic oxygen. 107

Figure 49. EELS quantification shows relative % contents of Si and O across the Si/oxide interface for Si(100) oxidized by atomic oxygen. 109

Figure 50. EELS quantification shows relative % contents of Si and O across the Si/oxide interface for Si(100) oxidized by molecular oxygen. 109

Figure 51. AFM image of Si(100) oxidized by molecular oxygen at 220°C; RMS≅0.830nm. .. 112

Figure 52. AFM image of Si(100) oxidized by atomic oxygen at 220°C ;RMS≅1.536nm. 113

Figure 53. AFM image of Si(111) oxidized by molecular oxygen at 220°C; RMS≅0.479nm. .. 114

Figure 54. AFM image of Si(111) oxidized by atomic oxygen at 220°C; RMS≅3.681nm. 114

Figure 55. AFM image of Si(100) oxidized by O_2^+ at 25°C; RMS≅ 66.25 nm. 115

Figure 56. XPS spectrum obtained from Si(100) oxidized by atomic oxygen at 220°C. 118

Figure 57. Si^{4+} and Si^{0} valence states observed in XPS spectrum obtained from Si(100) oxidized by atomic oxygen at 220°C in LDS. 118

Figure 58. XPS spectrum obtained from Si(111) oxidized by atomic oxygen at 220°C in LDS.119

Figure 59. Si^{4+} and Si^{0} valence states observed in XPS spectrum obtained from Si(111) oxidized by atomic oxygen at 220°C in LDS. 119

Figure 60. XPS spectrum obtained from Si(100) oxidized in O_2^+ source at 25°C........ 120

Figure 61. Si^{4+}, Si^{2+}/Si^{3+} and Si^{0} valence states observed in XPS spectrum obtained from Si(100) oxidized in O_2^+ source at 25°C........ 120

Figure 62. Schematic of initial oxidation steps of Si(100) surface by molecular oxygen [91]. . 129

Figure 63. Schematic of initial oxidation steps of Si(100) surface by hyperthermal atomic oxygen........ 131

Figure 64. Comparison of initial oxidation steps of Si(100) surface by (a) molecular oxygen (b) hyperthermal atomic oxygen........ 132

PREFACE

Thanks to my thesis advisor, Dr. Judith Yang for supervision, financial support and all the help in the previous years. The funding for this research is provided from AFOSR through MURI. I wish to thank Dr. Minton, (Montana State University), Dr. Popova, (University of Chicago), and Dr.Yates (Surface Chemistry Department, University of Pittsburgh) for the oxidation of silicon samples by atomic oxygen in their equipment. From the CMM, at Urbana Champaign, I am grateful to Dr. Haash, Dr.Averback and Dr.Williams, for their help. I am especially thankful to Dr. Twesten, for helping with the experiments, as well as for his advice and expertise. Thanks to my committee members, Dr. Jean Blachére and Dr. Jörg Wiezorek, for taking the time to review this thesis. Thanks to Dr. Goldman for his constant help to improve my English, and for reading this thesis. Thanks to Dr. Zhou, my group college, for his help in many occasions. Thanks to Cole Van Ormer and Fengting Xu from MSE Department for their help. I wish to thank my husband, Predrag, for being a great companion, for his constant support, encouragement and countless discussions, even in the middle of the night. I also want to thank my family for their love, encouragement and support. Although they are across the ocean, they are with me always. Most of all, I want to thank my dear dad, who was always so proud of me, with all his hart, and who believed that I can achieve anything. He gave me the strength for everything I accomplished and he will always be with me. This could not have been achieved without him. This work is dedicated to my beloved father, Драгољуб Ранђеловић, and to my husband, Predrag Kisa.

Драги мој тата, хвала ти за све што си учинио, што си увек веровао у мене и поносио се. Овај рад је посвећен теби и Пеђи. Остајеш заувек са мном. Твој Маки.

1.0 INTRODUCTION

The overall goal of this research is to gain fundamental understanding of the degradation mechanisms of semiconductors in the low earth orbit (LEO) conditions. Single-crystals of silicon with two different orientations, (100) and (111), were chosen as a model semiconductor material.

Kapton and FEP Teflon polymers are used in the construction of solar array blankets and easily erode when exposed to reactive atomic oxygen. Depending on the altitude, time of the day and season, atomic oxygen flux and temperature change. Constant thermal cycling, ultraviolet radiation and debris impacts additionally influence the material failure rate. The larger erosion caused by the impacting atomic oxygen will cause the effect of secondary factors to be more serious. A thin film of silica is used as the protective coating.

Since hyperthermal atomic oxygen (AO) is the primary species causing rapid degradation of materials in LEO, the focus of this thesis project is the effect of AO on Si oxidation. Results from the oxides grown by using AO species were compared with the oxides that were thermally grown on Si. The oxides were characterized with with a wide variety of experimental techniques, including Rutherford Backscattering (RBS), High-Resolution Transmission Electron Microscopy (HRTEM), Selected Area Electron Diffraction (SAED), Electron-Energy Loss Spectroscopy (EELS), X-ray Photoelectron

Scattering (XPS) and Atomic Force Microscopy (AFM). A model based on thermionic emission will be presented to explain the differences between the oxidation mechanisms of Si by atomic and molecular oxygen.

2.0 BACKGROUND

2.1 LOW EARTH ORBIT (LEO) ENVIRONMENT

Space vehicles in the low earth orbit are exposed to a harsh environment that can significantly increase their failure rate. The low earth orbit ranges from 200 to 700 km in altitude, with average surface temperatures that vary between 200 and 400K. Atomic oxygen is considered to be the most hazardous factor causing corrosion and degradation of the spacecraft materials, acting either alone or in synergy with other components, such as erosion, ultraviolet radiation, solar irradiation, electron and proton exposures and fluctuations in temperature. Atomic oxygen is the result of the photodissociation of molecular oxygen in the upper atmosphere of the Earth by solar photons which have a wavelength shorter than 2430 A^o [0, 2]. The oxygen reasocciation rates are much lower than the dissociation rates, due to the low vacuum in LEO. The number density of AO at approximately 250km altitude is 10^9 atoms cm^{-3}, corresponding to the density of residual gas in vacuum of 10^{-7} Torr [3]. Therefore, a high concentration of AO exists, which increases with decreasing altitude. As a direct consequence of the high velocity of orbiting spacecrafts (8km/sec at 250km altitude), the atomic oxygen flux is high (10^{14} atoms $cm^{-2}sec^{-1}$) and has a kinetic energy of about 5eV.

Hyperthermal AO is difficult to produce on Earth. However, in the past several years, a number of ground based laboratories have been established, using different types of atomic oxygen - producing devices broadly grouped into plasma and neutral beam sources. These ground level laboratories had been established for the obvious reason of the high cost of material testing in the real LEO environment.

2.2 MATERIALS PROTECTION FROM ATOMIC OXYGEN

Protection of spacecraft material from atomic oxygen attack can be achieved by overlaying thin-film metal or semiconductor oxides or other protective coatings, as shown in Figure 1. Polymeric materials such as Kapton or FEP Teflon are used in the construction of solar array blankets. Polymeric materials are readily oxidized when exposed to the LEO atomic oxygen and gradual reduction in thickness takes place as a result of the formation of volatile products [4]. Surface degradation of polymers caused by atomic oxygen lowers the thermal blanket performance. A current issue is the need to protect these polymeric materials from erosion without affecting their functional properties such as thermal emmitance and solar absorptance.

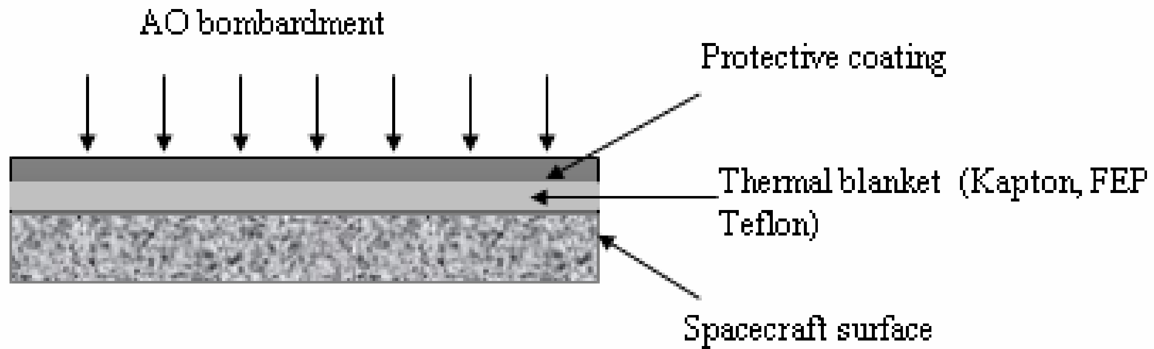

Figure 1. Exterior surface of a spacecraft in the cross-section view

Protective coatings are required to be durable in the presence of atomic oxygen as well as sufficiently thick to prevent oxidation of underlying material since oxide must form a diffusion barrier to atomic oxygen. The thickness of the protective coating is an important factor in predicting AO diffusion through the coating and eventually reaching the polymer surface causing degradation of the thermal blanket. On the other hand, the coating must be thin enough not to affect functional properties of the underlying material –solar absorptance and thermal emittance. Extensive mass loss and morphology change into the "carpet-like" structure of polymeric film are evident under the AO exposure [5].

Oxide coating uniformity is critical since small pinholes in the coating lead to the erosion of the underlying material due to its direct contact with atomic oxygen; therefore, coating perfection is of great importance [6]. In the low earth orbit, impacting atomic oxygen gains its energy from the spacecraft's orbital velocity, but there is also a distribution of atomic oxygen impact energies as a result of the atomic oxygen thermal velocity and orbital inclination. The flux of AO impacting the spacecraft surface is dependent on the altitude, solar activity, time of day and season of the year. The fluence of AO impacting the spacecraft surface is dependent upon the integrated flux over the

duration of arrival. It was concluded that orientation of the spacecraft surface relative to the ram AO arrival determines AO fluence.

As the illustration of protective coating’s importance one can consider degradation of unprotected Kapton. For 15-year exposure duration, unprotected Kapton will show 1.2 mm thickness loss. That is much more than the desired solar array blanket thickness of 0.05mm. There was much more effort toward identification of an alternative protective coating than toward the replacing of Kapton [5].

Materials that are considered as the potential candidates for the protective coatings include SiO_2, Al_2O_3, silicones, Al and indium tin oxide. The reasons for the imperfections forming in the protective coatings can be very different. Some of the examples are: contamination of the surface prior to the thin film deposition, microscopic undulations on the polyamide surface, abrasion during handling or processing, micrometeoroid and debris impact while in orbit. Currently, 600-1300A^o thick SiO_x ($1.9 < x < 2.0$) sputter-deposited coatings are used for thermal blanket protection from the atomic oxygen. This type of coating shows good adhesion to the substrate as well as a small number of defects and imperfections [7].

A SiO_x protective coating can be directly deposited on the polymers, or Si can be deposited and oxidation by AO allowed. We have chosen the latter case, since it can be applied both on Si as base material for semiconductor devices and for solar cell applications.

2.3 WHAT IS KNOWN ABOUT ATOMIC OXYGEN?

Kinetics of adsorption of atomic oxygen on Si(100) was investigated by Engstrom et al. using XPS and probability of adsorption of atomic oxygen as a function of substrate temperature, coverage and beam translation energy [8] . Figure 2 shows the adsorption probability of atomic and molecular oxygen on the Si(100) substrate.

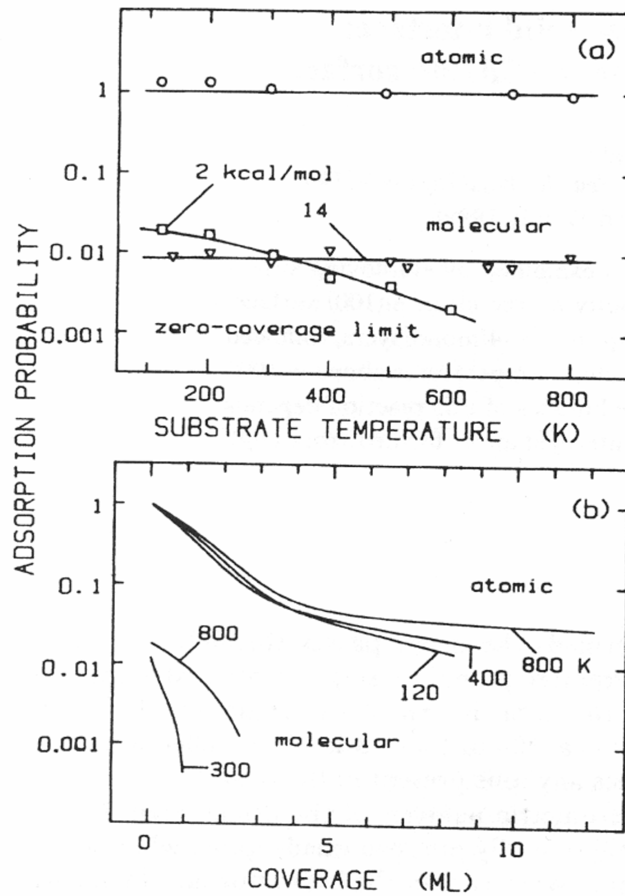

Figure 2. Adsorption probabilities for atomic and molecular oxygen (a) for zero oxygen coverages as a function of substrate temperature, and (b) for different oxygen coverages on different substrate temperatures [8].

Adsorption probability of molecular oxygen is dependent on both incident beam energy and substrate temperature, and ranges from 0.002-0.04. In contrast, atomic oxygen adsorption probability is not affected by the substrate temperature, angle of incidence and incident beam energy, it is 1.00 (for substrate temperature 120-800K) as can be seen in Figure 2-a. This finding indicates a facile, direct adsorption of atomic oxygen on the exposed material. The oxygen coverage of the substrate plays a significant role in the adsorption probability of atomic and molecular oxygen. This is shown in Figure 2-b, by Engstrom et al. [8]. It can be seen that the adsorption probability for atomic oxygen is much greater than that for molecular oxygen for all coverages. For atomic oxygen, there is a rapid decrease in adsorption probability as the coverage increases to 3-4 monolayers (ML) (1ML=$6.8x10^{14}$ atoms cm^{-2}). After this coverage is reached, there is slower adsorption of atomic oxygen and the rate of oxidation begins to be dependent on the substrate temperature; e.g., it increases as the temperature rises. This point at 3-4ML is defined as the break in the atomic oxygen kinetics. For molecular oxygen there are also two stages of adsorption, but the transition occurs near 1ML. Figure 3 below shows coverage (ML) that can be achieved by atomic and molecular oxygen oxidation when certain exposure (ML) to these oxidizing species is applied.

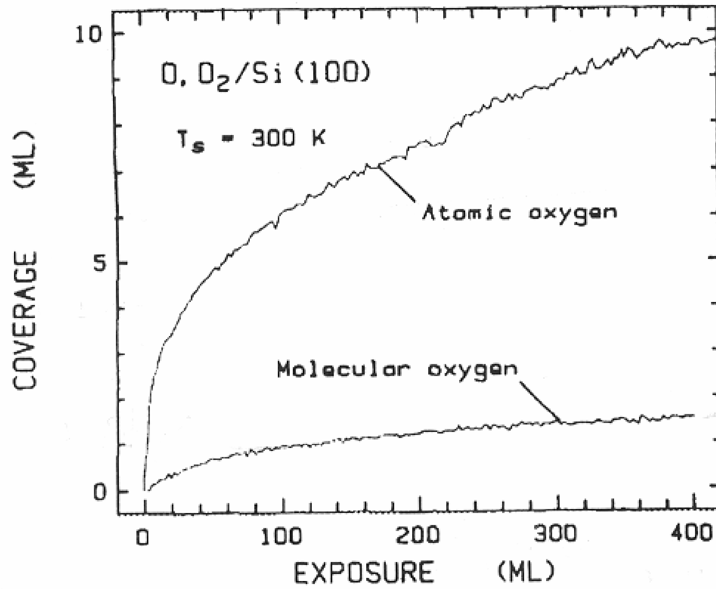

Figure 3. Coverage dependence on exposure for atomic and molecular oxygen on Si(100) substrate at 300K [9].

Molecular oxygen shows a two step reaction, with initial, fast step that reaches its completition around 1ML and saturates at ~1.5ML. On the other hand, for atomic oxygen the fast step of adsorption reaches its completition near 3-4ML and it is followed by the slower step, which does not saturate, even at coverages of 10ML and greater. In the second, slow regime of adsorption, chemisorption is not direct. Most probably it involves transport through the oxide film to the underlying Si(100) substrate. This two-stage oxidation by atomic oxygen shows similarities with the well-known Deal-Grove oxidation model which is applied to the thick oxide growth and will be described in some details in chapter 2.4.1. [9].

The oxide thickness dependence on the atomic oxygen fluence is shown in Figure 4.

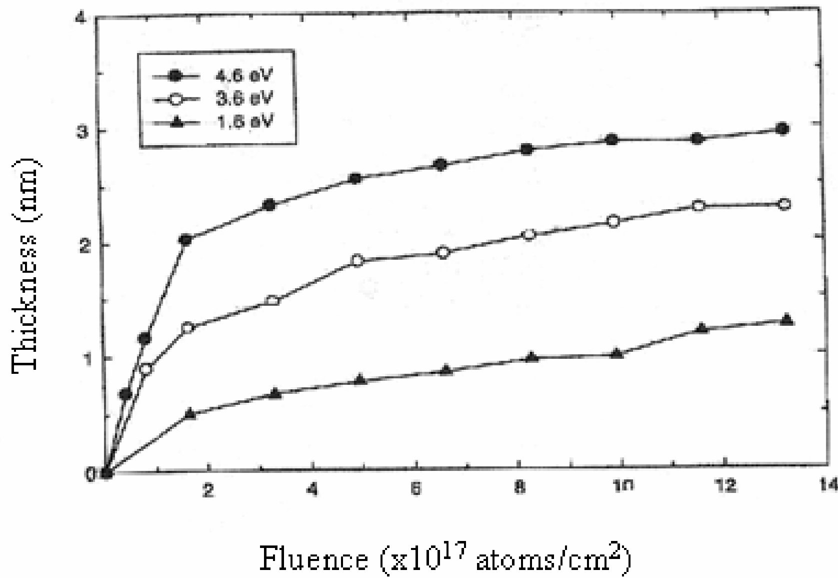

Figure 4. Oxide thickness versus fluence for atomic oxygen oxidation of H-terminated Si(100) at 297K . The hyperthermal atomic oxygen beam had three different translation energies: 1.6eV, 3.6eV and 4.6eV [10].

One intriguing observation, from Figure 4, is that H-terminated Si(100) surface can be oxidized by atomic oxygen even at the temperatures as low as room temperature. Previous studies have shown that HF-cleaned Si surface (Si surface with H-termination) oxidation does not proceed quickly even at 400°C, as compared to the clean surface with dangling bonds [11]. As mentioned before, two step processes are characteristic for the oxidation by atomic oxygen for all three oxidation curves shown on the Figure 4. Tagawa et al. found that the transition from the fast to slow oxidation stage is at the oxide thickness of one or two atomic layers (~2nm). Oxidation with dangling bonds at the surface region as well as backbond oxidation is the mechanism of the atomic oxygen fast oxidation stage on the Si substrate. Similarly to the previous investigators, they found that the slow stage is transportation of oxidants in the SiO_2 layer. These investigators also found that 5eV atomic oxygen produces stoichiometric, bulk-like SiO_2, and mainly the

presence of the Si^{4+} oxidation state with only a few percent of suboxides [12]. Engstrom et al. reported that oxidation of Si(100) by energetic atomic oxygen, but only of 0.16eV, kinetic energy, produced a large amount of suboxides which in XPS showed that the SiO_2 bulk signal was not the major peak in the analyses [12]. Based on previous research, it can be concluded that formation of bulk-like, stoichiometric silica is assisted by the high kinetic energies of the AO.

2.4 SILICON OXIDATION

When exposed to oxygen, the surface of the silicon oxidizes forming silicon dioxide (SiO_2), which is a high quality electrical insulator. The oxidizing species for two types of oxidation are pure oxygen and water vapor, and the chemical reactions for these cases are either

$Si + O_2 \rightarrow SiO_2$ for "dry" oxidation or

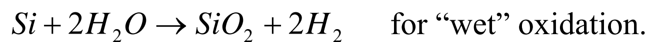

$Si + 2H_2O \rightarrow SiO_2 + 2H_2$ for "wet" oxidation.

Oxide growth kinetics for "wet" oxidation are about 10 times faster than for the case of "dry" oxidation.

Oxide growth kinetics can be divided into several steps. Initially, a surface reaction is responsible for the oxide growth, but with time, as the oxide thickness increases, arriving oxygen molecules must diffuse through the growing silica layer to reach the silicon surface where the reaction occurs.

Oxide growth depends on the Si substrate orientation, e.g., Si(111) surface oxidizes 1.7 x more rapidly than the Si(100) surface.

Surface preparation and cleaning prior to oxidation directly affects the Si/SiO_2 interface characteristics and consequent oxide growth. The Deal-Grove oxidation model introduces a linear constant reaction rate at the Si/SiO_2 interface and this rate can be influenced by the surface preparation (e.g., available Si bonds in the Si substrate can be highly reactive - so-called "dangling" bonds - or they can be passivated with the hydrogen or some other atoms, depending on the cleaning procedure). Doping of Si influences only the interface reaction. There is an increase in the linear rate constant for heavily doped Si, while the parabolic rate constant is not affected significantly.

2.4.1 Deal –Grove Oxidation Model

Thermal oxidation of single crystal silicon is commonly represented by the Deal-Grove oxidation model that can be used to explain both "dry" and "wet" oxidation. The Deal-Grove model is generally valid for both "dry" and "wet" oxidation, in the range of temperatures 700-1300°C and partial pressures between 0.2 and 1 atm for the thickness of the oxides, 0.03-2 microns [13]. In the experimental part of this work it will be shown that investigated oxides are much thinner, but the brief overview of the Deal-Grove model will be given here, since it represents the basis and gives an understanding of the processes involved in the oxidation mechanism. Further modifications and some other alternative models will be presented in order to approach more closely to the desired experimental conditions used in this research.

The Deal-Grove oxidation model can be explained using Figure 5, where symbols are as follows:

C_g = oxidant molecules concentration in the bulk gas (O_2)

C_s = oxidant molecules concentration in the layer immediately adjacent to the oxide surface

C_o = equilibrium oxidant molecules concentration at the oxide surface

C_i = oxidant molecules concentration at the Si/SiO_2 interface

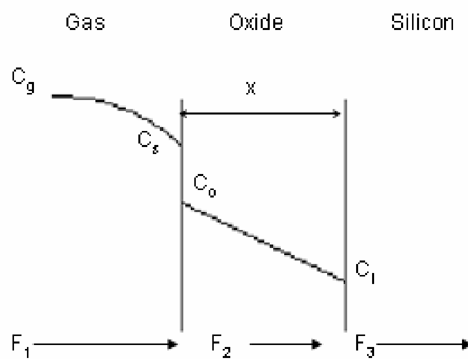

Figure 5. Model for silicon oxidation [13].

C_g>C_s because the oxidant is depleted on the oxide surface and C_s >C_o due to the oxygen solubility limits in SiO_2.

F_1= flux of the oxidant species from gas to the gas-oxide interface

F_2= flux of the oxidant species from gas-oxide to the oxide-Si interface (or flux through the oxide layer)

F_3= flux of the oxidant species to the oxide-Si interface (or oxidant flux consumed by reaction at the Si/SiO_2 interface)

Flux is represented as the number of molecules per unit area and unit time, and fluxes are given as:

$$F_1 = h_g (C_g - C_s) \qquad \text{(Equation 1)}$$

where h_g=gas phase mass transfer coefficient [cm/sec]

The expression for the flux F_2 is known as Fick's law of solid-state diffusion and a concentration gradient is responsible for the flux of oxidant through the oxide.

Using the ideal gas law and Henry's law,

$$C_g = \frac{n}{V} = \frac{p_g}{kT} = \frac{C^*}{H}\left(\frac{1}{kT}\right) \qquad \text{(Equation 2)}$$

where C^* = equilibrium bulk concentration of oxidant in oxide and Henry's law constant.

Similarly, $C_s = \frac{n_s}{V} = \frac{p_s}{kT} = \frac{C_o}{H}\left(\frac{1}{kT}\right)$ (Equation 3)

where C_o = oxidant concentration just inside the oxide surface.

So, $F_1 = h(C^* - C_o)$ (Equation 4)

where $h = \frac{h_g}{HkT}$ (Equation 5)

$$F_2 = -D\frac{dC}{dx} \cong D\frac{(C_o - C_i)}{x} \qquad \text{(Equation 6)}$$

where D =the diffusivity of the oxidant molecule in SiO_2 [cm^2/sec] (diffusion coefficient) and x= oxide thickness

Oxidant reacts with Si following 1st order reaction:

$$F_3 = k_s C_i \qquad \text{(Equation 7)}$$

where k_s= rate constant of silicon oxidation at Si/SiO_2 interface [cm^2/sec]

At steady-state, after the initial oxide thickness x_i growth, three fluxes are equal $F_1=F_2=F_3=F$ resulting in $F = \dfrac{k_s C^*}{1 + k_s/h \; + k_s x/D}$ (Equation 8)

The expression for the rate of oxide growth is:

$$\frac{dx}{dt} = \frac{F}{N_1} \qquad \text{(Equation 9)}$$

where N_1= number of molecules of oxidant incorporated into a unit volume of the oxide layer.

Evans [14] originally developed a linear-parabolic equation, which is obtained as a solution when $x=x_i$ and $t=0$:

$$x^2 + Ax = B(t + \tau) \qquad \text{(Equation 10)}$$

$$A \cong 2D\left(\frac{1}{k_s} + \frac{1}{h}\right) \qquad \text{(Equation 11)}$$

$$B \cong \frac{2DC^*}{N_1} \qquad \text{(Equation 12)}$$

$$\tau = \frac{x_i^2 + Ax_i}{B} \qquad \text{(Equation 13)}$$

x_i = the thickness of the initial oxide layer that is formed by other mechanisms not included in the Deal-Grove model (e.g space charges).

If the oxide thickness or times are small, a linear rate law is found:

$$x \cong \frac{B}{A}(t + \tau) \qquad \text{(Equation 14)}$$

$t << A^2/4B$

and B/A=linear rate constant

This regime is known as reaction-controlled and it is determined by the reaction rate of the oxidant with silicon on the Si/SiO_2 interface.

If the oxide thickness or times are larger - a parabolic law is obtained:

$$x^2 \cong Bt \qquad \text{(Equation 15)}$$

where $t >> A^2/4B$ and $t >> \tau$ and B= parabolic rate constant

This regime is known as diffusion-controlled.

The main limitation of the Deal-Grove oxidation model is its validity for shorter oxidation times since it predicts greater oxide thickness than was experimentally found (for $t \to 0$, $x \to 250A^o$). To explain thin oxide formation, the overview of the other oxidation models is given.

2.4.2 Other Alternative Models of Oxidation

It is very difficult and sometimes even impossible to know if the proposed model and the parameters involved are correct. The reason for presenting oxidation models other than the generally accepted Deal-Grove model is to provide better agreement with the experiment and to approach more closely to the real conditions. There are many factors involved in the composition and defects present in the thin films- and these factors could be surface orientation, surface preparation, impurities, etc. These various factors make low-temperature oxidation still an unexplored field, but progress is made starting from the single-crystal films in order to reduce the influence of the substrate factors.

According to a number of models, after an oxide layer covers a substrate surface, both electrons and ions transport through the film or reaction at the interface defines the

reaction rate. Wagner mechanism for parabolic oxidation proposes that mass transport involves diffusion, which is driven by the chemical gradient across the oxide film.

The oxide structural effect model was proposed by Revesz et al. [15]. Gas permeability studies indicated the presence of microchannels (diameter < $50A^o$) in thermally grown SiO_2. Also, it was noticed that etching of oxide films proceeds in non-homogeneous manner. It was proposed that the transport processes in noncrystalline silicon oxide are usually affected by specific defect structure of the oxide. This oxide film is usually amorphous and can contain some structural micro-heterogeneities, which can provide high diffusivity paths for the diffusing species. Oxidizing species might diffuse preferentially along the channels present in the oxide structure. The large thickness in the initial oxidation regime may be due to the relative easy migration of oxygen along channels in the oxide.

This model could be able to explain parabolic regime and its enhancement for both MO and AO, since it provides high-diffusivity paths. If the oxide structure is more ordered and almost polycrystalline at some locations in the oxide, that could affect parabolic rate. The diffusion of MO will occur very slowly, since it is a larger species. Also, the diffusion of MO occurs through the amorphous media - there are no high diffusivity paths, resulting in sluggish diffusion. The diffusion of AO will be affected by the smaller oxidizing species movement and also by the structural characteristics of the oxide formed.

Stress effect models propose that there is a demand for extra space due to the volume expansion during oxidation. This can be satisfied only at high temperatures, when the network can rearrange by viscous flow. At the lower temperatures the network is not

able to rearrange fast enough, resulting in residual stress and strain in the oxide film. The stress effects can affect the kinetics of thermal silicon oxidation, particularly in the initial stages. There is a controversy whether the stress affects the interface reaction, or the diffusion process. The intrinsic stress in the oxide is due to the increase in molar volume during the conversion of Si into SiO_2. Due to the fact that the oxide is constrained by the substrate surface, the volume required for the oxide to grow must be obtained in the direction normal to the silicon substrate surface. If temperature is below 950^oC, viscous flow is not possible and additional volume cannot be obtained. This results in development of an intrinsic stress. At a high temperature, larger that 950^oC, oxide can easily flow in the direction normal to the substrate surface, and the volume required can be obtained.

Irene proposed that the interface reaction is affected by the stress developed in the oxide [16]. Due to the lack of viscous flow, the Si atoms available on the interface for the reaction are reduced and the reaction is inhibited. Inability of the oxide to obtain the necessary molar volume in the normal direction will screen other Si atoms on the surface from reacting. The effective concentration of Si available for the reaction is controlled by the rate at which Si can viscously relax and reduce screening effects.

Two models propose that stress affects the diffusion process, rather than the reaction at the interface. Doremus [17] proposes that the linear part does not represent the reaction at the interface, but instead arises from strain in the oxide. The diffusion of the oxidizing species is the only parameter that controls the oxidation rate according to this model. The other model, given by Fargeix [18], introduces the stress effect directly into the parabolic rate constant of the Deal-Grove model.

The Interfacial layer model proposes that there is an oxygen –diffused zone near the Si/SiO_2 interface [19]. Oxidizing species diffuse into the Si substrate under the following conditions:

-the diffusivity of oxidizing species is high

-the concentration (or partial pressure) of the oxidizing species at the interface is high-this occurs only for the very thin oxide films

The flux of oxidizing species is very high if the film is very thin, thus leading to the formation of the diffused-zone. Instead of reaction at the interface, homogeneous reaction occurs in the oxygen-diffused zone in Si, resulting in enhancement in the oxidation rate. Once the oxide film becomes thick enough, the diffusion through the film will be reduced and all the oxidizing species will be consumed by the interfacial oxidation. There will be no more diffusion into the Si substrate. The oxygen-diffused zone thickness depends on the oxide thickness, oxygen diffusivity into Si, oxygen partial pressure, oxygen concentration in Si, temperature and Si crystal orientation. Three processes occur in the series during the oxidation: diffusion of oxygen through the thin gas film, diffusion of oxygen through the oxide film and the reaction at the silicon surface. Each of these three processes can be considered as the rate-limiting step.

The Cabrera-Mott model is widely accepted when low-temperature oxidation conditions are considered. This model describes ionic transport mechanism which is enhanced due to the induced E field [20]. The Cabrera-Mott model proposed cation diffusion, represented in Figure 6.

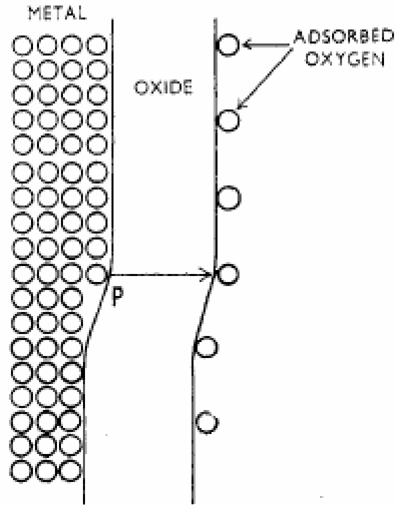

Figure 6. Schematic of the ion removal from the metal surface [20].

The ion is removed from its original position P on the metal surface layer and placed into an interstitial position of the oxide. These two steps are known as the process of solution of the ion in the oxide. An inverse logarithmic growth rate is predicted by the following expression:

$$1/X = A - B\ln t \qquad \text{(Equation 16)}$$

where, X is the oxide film thickness, A and B are the fit parameters and t is time.

Generally, movement of charged species (anions) must be compensated with the movement of the other charged species (electrons) in the opposite direction, so that the electro- neutrality is preserved. During the early oxidation stages, an ion moves across the oxide to reach (neutralize) an opposite charge ion and to react forming oxide, causing the field at the oxide surface to immediately decrease until another ion is created on the surface of the oxide. It is apparent that the other charged species (electrons) must move at

the same time through the oxide, just in the opposite direction. Thermionic emission or tunneling can be a way to transport electrons across the interface [21].

Figure 7 describes the movement of different charged species through the oxide scale.

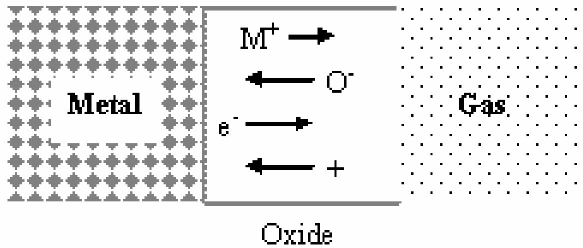

Figure 7. Schematic drawing of the charged species moving during thermal oxidation [21].

Low-temperature oxidation can be limited by the electronic or ionic species transport. Mott proposed an electron model, which postulates that the rate-determining step is tunneling through the oxide scale [22, 23]. A direct logarithmic rate equation is proposed for the growth of oxide films.

Cabrera and Mott [20] proposed that ion –diffusion processes are rate limiting and this was reiterated by Fehlner and Mott [24]. The ionic and electronic currents are present at the same time and electrons and ions can neutralize each other for certain distances, as given by Cabrera and Mott. Their theory assumes adsorption of oxygen atoms at the surface of the oxide and easy passing of electronic species across the oxide in order to

equilibrate metal and absorbed oxygen. Anions are formed and subsequently the electric field, which gives rise to the ions transfer through the oxide film.

Previously, ion movement was thought to be the rate-limiting, parabolic process. The Cabrera-Mott model proposed that dissolution of anions at the oxide/gas interface (linear or inverse logarithmic) or dissolution of cations at the at the metal/oxide interface are actually the rate limiting processes.

Fromhold [25] showed that electron tunneling in a one step tunneling process occurs easily up to an oxide thickness of ~30A^{o}. The field lowers the activation energy for the ion movement and therefore the oxide can continue to grow at low temperature. The Debye length for oxides at room temperature is 0.1-1 micron and Cabrera-Mott [20] showed that ions and electrons can neutralize each other for distances greater than the Debye length. So, in the case of thin films and for T=300-500°C, these two currents can be considered independently. It is important to distinguish between the two different mechanisms for the electron transport, tunneling and thermionic emission. An incident electron with the energy below the height of a potential barrier of limited thickness has a finite probability of penetrating the barrier. Particles that have penetrated the barrier in this manner are said to have tunneled through the barrier as opposed to having been excited over the top of the barrier. A thermionic emission becomes a more likely mechanism for the electron transport when the oxide thickness exceeds 20-30A^{o}, since electron tunneling is very difficult. The region in the film thickness where electron tunneling and thermal emission occur simultaneously to an appreciable extent is limited. The tunneling current is extremely large for very thin films, thinner than 20A^{o}, but decreases sharply for larger thickness. The exact transitional thickness depends on the

metal-oxide work function. The barrier to electron injection to the metal/oxide interface is ~1eV, so thermionic emission cannot occur easily at low temperatures while tunneling is essentially independent of temperature. For the case of thicker films, the scattering prevents the thermionically emitted electrons from traversing the oxide in one step process. An electron concentration gradient is established and both ionic and electronic currents are diffusion controlled [20, 25].

The thermionic emission oxidation model for the oxidation of Si by O_2

As mentioned before, the Deal-Grove oxidation model is not valid for the oxide thickness less than 250A^o. Low temperature oxidation of silicon by O_2 follows a linear to parabolic oxidation model. Transition from the linear to parabolic regime occurs at ~1ML for $O_{2.}$ Parabolic step saturates at ~1.5ML [9].

Here we will focus on the initial, linear regime of oxidation. Commonly, low temperature oxidation of silicon is considered to be a field driven process. Thin film growth is based on ionic and electronic transport, which occurs simultaneously during the oxidation process [20, 25, 26].

Electrons can traverse the oxide film either by thermionic emission from the metal to the conduction levels of the oxide or by tunneling. As a consequence, the potential V is established between the metal and oxygen adsorbed on the oxide surface. It was assumed that the oxygen atoms are adsorbed on the oxide surface and electronic species pass rapidly through the oxide layer by tunneling to establish equilibrium between the metal and adsorbed oxygen. This creates anions and electric field, which facilitates transport of ions across the oxide film.

The thermionic emission model, as proposed by Irene et al., assumes that the rate-limiting step is electron flux from Si to SiO_2 [27, 28]. These authors determined that thermionic electron flux from Si to SiO_2 is proportional to the oxide growth rate and that the key step in the interface reaction is emission of electrons from Si to SiO_2. The electron flux from Si to SiO_2 by the thermionic emission is given by the Richardson-Dushman equation:

$$F_{et} = AT^2 \exp(-\chi_0 / kT) \qquad \text{(Equation 17)}$$

where A is Richardson constant, T is temperature in K, χ_0 is barrier height (from the Fermi level to vacuum, for metals). This can be adjusted further for a Si/SiO_2 interface, since there are several energy levels on which electrons are available for transfer into the vacuum. If an electron is emitted from the valence band 4.25eV is required, while for emission from the intrinsic Fermi level of Si and from the conduction band 3.7eV and 3.15eV are needed respectively. Figure 8 represents a schematic drawing of the fluxes for the thermionic emission model. We believe this model describes our experimental results better than the other oxidation models.

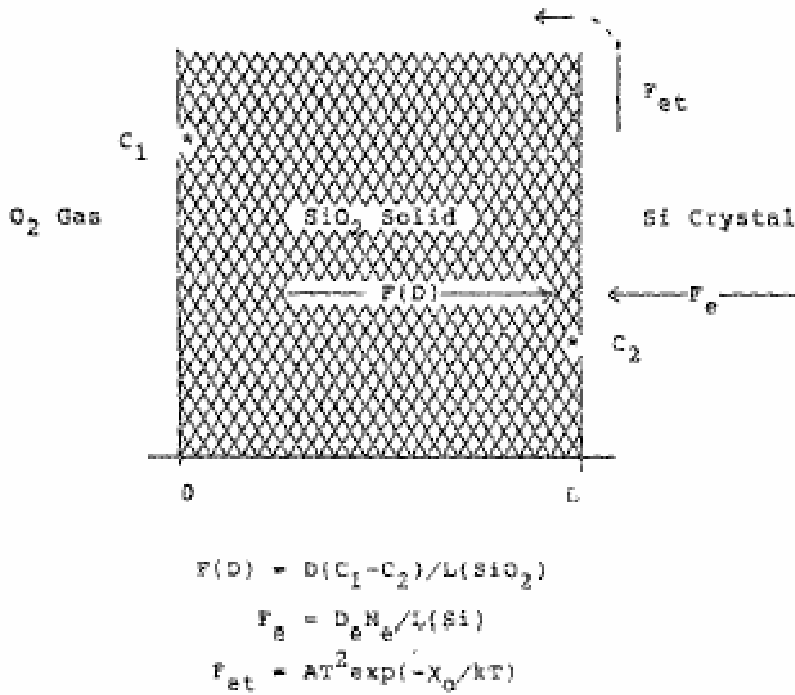

Figure 8. Schematic representation of fluxes for thermionic emission model [28].

Three fluxes should be considered:

Diffusive flux of oxidant:

$$F_d = D(C_1 - C_2)/L_{(SiO_2)} \qquad \text{(Equation 18)}$$

where D is the diffusivity of oxidizing species, C_1 is its concentration at the gas/oxide interface and C_2 is the concentration at the oxide/Si interface. L_{SiO2} is the oxide thickness. The electron flux to the Si surface is given by the following equation:

$$F_e = D_e N_e / L_s \qquad \text{(Equation 19)}$$

where D_e is electron diffusivity and it is given by the equation:

$$D_e = \mu_e (kT/e) \qquad \text{(Equation 20)}$$

where N_e is electron concentration, μ_e is electron mobility and L_s is the distance into the bulk Si from the Si/oxide interface.

The rate limiting flux is proposed to be flux of electrons by thermionic emission since it was found that electron flux F_e is 10^6 times greater than the oxidation rate even as deep in the Si substrate as 10^3 nm. Thermionic electron flux is found to be proportional to the oxidation rate. This flux is equated to the observed oxidation flux (SiO_2 flux) and value of χ_0 was calculated. The obtained value of about 3eV, which corresponds to the barrier between Si and SiO_2 conduction bands, showed that thermionic flux is really rate limiting step.

Oxidation steps for the oxidation of Si by O_2, as determined by Irene et al., are:

1. e^- (conduction band of Si) $\rightarrow$ e^- (Si surface)
2. e^- (Si surface) $\rightarrow$ e^- (free in SiO_2)
3. e^- (in SiO_2) $+O_2$ (from diffusion) $\rightarrow$ O_2^-
4. $O_2^- \rightarrow O^- + O$
5. Si^+ (at Si surface) $+O^- + O \rightarrow SiO_2$

Step 1 is the flux of electrons to the Si surface

Step 2 is emission of electrons over the energy barrier-rate limiting

Step 3 is electron attachment to O_2

Step 4 is decomposition of O_2^- into neutral and charged species

Step 5 is reaction of atomic and charged species.

Oxide formation at low temperature depends on electron supply and $\sim 10^{15}$ cm^{-2} surface electron states on Si surface are available, thus enabling forming of small oxide

thickness (5-20A^o). Surface states containing trapped electrons are not available any more after the initial oxide formation (native oxide formation); therefore rate of the oxidation process decreases. In order to continue the oxidation process a higher temperature must be employed to achieve thermionic emission.

In the first stage trapped electrons are used and this is similar to the native oxide formation. After the first step of oxide formation, all the trap electrons in the surface states are used and ~ 10 A^o oxide is formed. Further growth of the oxide film is enabled by tunneling process, which is temperature independent. When the oxide thickness reaches 20A^o, tunneling process becomes very difficult since it is limited by the oxide film thickness. Silica layer continues to grow by thermionic emission mechanism [25]. Thermionic emission helps electrons to overcome energy barrier and to transfer from the Si to SiO_2 conduction band. This is referred as the step 2 in thermionic emission model and it is considered to be the rate-limiting step. Electronic transfer from the Si to SiO_2 conduction band by thermionic emission on 220° C appears to be very sluggish. Released electrons are attached to the O_2 molecule and in the step 4 O_2^- ion decomposes into the O^- ion and neutral O atom. These species are monoatomic and more mobile than O_2. Therefore, it will diffuse very fast to reach Si/SiO_2 interface to react with the Si^+ cations. Once the all electrons from the Si conduction band are used, the dissociation of O_2 on the SiO_2 surface will become very difficult. There will be no more dissociation of the O_2^- on the SiO_2 surface. Consequently, for the oxide to continue to grow, O_2 must diffuse. This slow diffusion process causes parabolic regime.

3.0 STATEMENT OF OBJECTIVES

The objective of this study was to investigate the oxidation of silicon-single crystals by atomic and molecular oxygen and to understand the differences in the oxidation mechanisms and formed oxide structures. There is a lack of information about the oxidation behavior of atomic oxygen, although it is known that it is a highly reactive species.

The reaction of 5.1eV atomic oxygen with the materials can be quite different from the reaction of molecular oxygen. The oxidation mechanism could be altered and can have an impact on the oxide structure created. The structure of the oxide formed by atomic oxygen is very likely to differ from the structure of amorphous silica usually formed by thermal oxidation.

4.0 EFFECT OF 5eV ATOMIC OXYGEN ON Si OXIDATION

The transition from the linear to parabolic regime in the oxidation of Si by AO occurs at ~3-4ML. It was determined that the parabolic oxidation step does not saturate even at 10ML for the oxidation by AO [9].

We propose that 5eV hyperthermal AO reacts with the silicon surface differently than O_2. Hypotheses for the Si oxidation by AO will be given here:

Hypothesis I

The thickness of the oxide formed by AO oxidation should increase as compared to the oxide thickness created by O_2.

Previous investigators found that ultra-violet illumination produced increase in the oxide thickness for 50 % [20]. Increase in oxide thickness was explained by the increase of the field in the oxide layer. The field was increased since more electrons were ejected from the metal to the adsorbed oxygen.

The increased oxide thickness due to atomic oxygen species was noted by Tagawa et al., who examined the kinetics of hyperthermal atomic oxygen, produced by a laser detonation source, on Si(100) by XPS. These investigators reported the formation of a 1.75nm thick oxide layer at the temperature of 493K and time of 7h with a flux of 2.6×10^{13} atoms $cm^{-2} sec^{-1}$ [5, 10].

The oxide thickness determination is crucial in order to conclude regarding the possible oxidation mechanisms. We used two different methods, RBS and HRTEM to determine the oxide thickness precisely.

Hypothesis II

AO should form less random and more homogeneous silicon-oxide microstructure.

Previous investigators noticed that ozone formed more ordered aluminum oxide on Al substrate [29]. Si oxidized by ozone showed homogeneous structure from the Si/SiO_2 interface to the oxide surface, as confirmed by the constant etching rate with HF solution through the oxide layer [30].

Since ozone dissociates on atomic and molecular oxygen, we expect similar behavior for the oxidation of Si by 5eV atomic oxygen. The oxide formed by atomic oxygen should be more ordered and more homogeneous as compared to the oxide created by O_2 oxidation.

A short description of the range of order will be given in the following text, in order to distinguish between “more” and “less” ordered structures. Also, the overview of silica allotropic modifications will be presented.

Amorphous material is characterized by non-periodic or non-regular arrangement of its atoms. Zachariasen [31] proposed that the atoms in the vitreous solids are linked by the same forces as the atoms in crystalline structures. He came to the conclusion that the extended three-dimensional structure of vitreous materials must be similar to the structure of crystals, but with the lack of periodicity and is disordered. The basic building block or unit is the same both for vitreous and crystalline silica and that is the SiO_4 tetrahedron, as

first proposed by Mozzi and Warren 1969 [32]. This was confirmed later, by Bell and Dean in 1972 and Gerber and Himmel in 1986 [33, 34].

The degree of ordering in the non-crystalline materials is defined by short-range order (SRO), intermediate or median and long-range order (LRO). Short-range order is common in vitreous structures since it refers to the first coordination sphere and nearest neighbors [35, 36, 37].

As mentioned above, the structure of silica is such that four oxygen atoms are tetrahedrally coordinated around each Si atom and whether it is amorphous, vitreous or crystalline depends on the Si-O bond length and O-Si-O angle and the range of order. Wright [35] defined several parameters that define median or short-range order. These parameters are: bond length (d), tetrahedral angle (φ), intertetrahedral bond angle (α), bond torsion angles (δ_1 and δ_2) and coordination number (n).

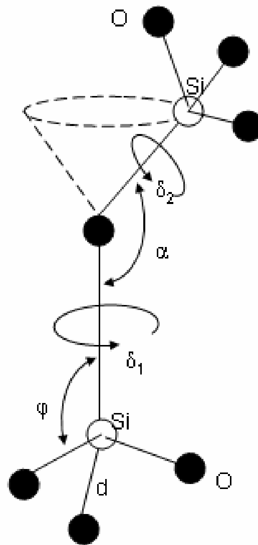

Figure 9. Parameters that define short and intermediate range of order [35].

Bond length d, coordination number n and tetrahedral angle φ, define the SiO_4 tetrahedron, while intertetrahedron bond angle α, and the bond torsion angles δ_1 and δ_2, define the connection of SiO_4 tetrahedral building units. The variations in the parameters defining tetrahedron unit are very small in different silicate glasses. Therefore, this basic unit is almost the same in vitreous and crystalline silica. What is very different in various silica glasses, are parameters that define interconnection of SiO_4 tetrahedrons [32]. These parameters, α, δ_1 and δ_2, are very different for the vitreous and crystalline silica.

Median range of order refers to the radial distance of 10-20A^o, thus extended beyond the adjacent tetrahedra. If there is such a range of order, there are structural features that one can observe-those are chains or rings originated from the way of tetrahedral interconnecting.

There is no long-range order in vitreous structure [33, 38]; this kind of order defines larger groups of building units than what can be observed in intermediate range order. The arrangement of these groupings is periodic and symmetric and features occur at the scale larger than 10-20A^o. This range of order is characteristic of crystalline structure. If there is some short-range order (SRO), but lack of long-range order (LRO) in the non-crystalline solid, it is defined as vitreous; if it lacks (SRO) or it is very limited, the non-crystalline solid is called amorphous [39].

Depending on the pressure and temperature during crystallization of the silica, different minerals can be formed. There are many crystalline forms of SiO_2, called allotropes, and some of them are: α-quartz, β-quartz, α-crystoballite, β-crystoballite, α-tridymite, β- tridymite, coesite, stishovite, lechatelierite and keatite. Prefix α in all these

polymorphs refers to the low temperature form while β refers to the high temperature form of the allotrope. The alpha polymorph is stable at the room temperature. Creating of β polymorphs requires heat and with the cooling, they transform into their alpha phase. Table 1 gives silica forms along with their crystal structure and the temperatures at which they exist.

Table 1. SiO_2 phases [40].

Mineral	Crystal System	Stable at T (^{o}C)
α-quartz	Trigonal	Room T-573
β-quartz	Hexagonal	>573
α-tridymite	Orthorhombic	<870
β- tridymite	Hexagonal	>870
α-cristobalite	Tetragonal	<268
β- cristobalite	Isometric	>268
Coesite	Monoclinic	Intense T and pressure (~2.3-7.8GPa)
Stishovite	Tertragonal	Intense T and pressure (~7.8 GPa)
Lechatelierite	Amorphous	
Keatite	Tetragonal	

Alpha-quartz is the most stable and common form of SiO_2, usually found at room temperature. α-tridymite and α-cristobalite do not occur as the stable phases, and can only be found as metastable phases that are converted to the stable forms of SiO_2 under certain pressures and temperatures. Only the α-quartz, β-quartz and tridymite can actually exist

as a stable phase under the room temperature conditions [40]. Coesite, stishovite and lechatelierite are very rare, natural forms of SiO_2 that are created under the conditions of extreme temperature and pressure. They can be found in the crater impact sites which possess huge temperature and pressure at the moment when meteorites struck the earth. Keatite is a synthetic SiO_2 form.

High–temperature oxidation of metals usually creates polycrystalline oxides, but SiO_2 formed by high temperature oxidation is non-crystalline. Low-temperature Si oxidation also forms non-crystalline oxides. Vitreous or non-crystalline thin films are very important materials in metal passivation.

Hypothesis III

The thickness of an interfacial region consisting of suboxides, SiO_x $(x<+4)$, formed by AO should be reduced. O_2 produces a 0.2-1nm region consisting of suboxides (from Si^o to Si^{4+}).

The reduction in the Si/SiO_2 interface thickness of sub-oxide region and clear presence of only Si^{4+} valence state for Si(100) oxidized by ozone was noted by other investigators. Ichimura et al. noted by XPS, second harmonic generation (SHG) and medium ion scattering spectroscopy (MEIS), that the ozone created Si/SiO_2 interface is very thin or almost non-existent, as opposed to the ~0.2-1nm thick interface transition layer formed when the oxide is thermally grown in molecular oxygen. They also found that suboxides formation was greatly suppressed [30].

The oxide created by ozone was etched off and surface roughness measured by scanning tunneling microscopy (STM) [41]. It was determined that the silicon/oxide

interface has less than 0.2nm root-mean-squared roughness. The interface formed was determined to be abrupt. Based on this, we expect flat and abrupt Si/SiO_2 interface to be formed by 5eV atomic oxygen.

5.0 SILICON-SINGLE CRYSTAL OXIDATION-EXPERIMENTAL PROCEDURE

5.1 ATOMIC OXYGEN SOURCES

The production of 5eV neutral atomic oxygen with the flux corresponding to that in low earth orbit atmosphere is critical for ground-based simulation of LEO conditions.

In order to simulate 5eV hyperthermal atomic oxygen in an LEO environment, atomic oxygen sources are used. Currently several types of atomic oxygen sources are in use: plasma source, RF source, beam/surface interaction based source and source based on the laser breakdown phenomena. Atomic oxygen sources differ in spreads of atomic oxygen energy and percent of produced atomic oxygen and consequently, some of them are more or less efficient.

Within the course of experiments, two atomic oxygen sources were used to oxidize Si-single crystals by reactive atomic oxygen, Laser Detonation Source and O_2^+ source.

5.1.1 Laser Detonation Source (LDS)

Laser Detonation Source (LDS) is used to simulate oxidation by hyperthermal 5eV atomic oxygen in LEO conditions. This AO source uses the laser breakdown phenomenon and was originally invented by Physical Sciences Inc (PSI) [42, 43]. CO_2

laser with 5-10 $Jpulse^{-1}$ and pulsed supersonic valve (PSV) are used in LDS. After pure oxygen gas introduction by (PSV) into the conical nozzle, the laser light was focused on the nozzle throat where it initiates plasma and heats it to more than 20000K. Due to the high temperature and high-density plasma expansion and consequent detonation, cold gas remains thermomolecular collision rate, which is dropped so low that the atomic species are frozen in the emerging beam. A quadruple mass spectrometer (QMS) is installed in the beam line in order to characterize produced AO beam by measuring time of flight (TOF) distribution [5].

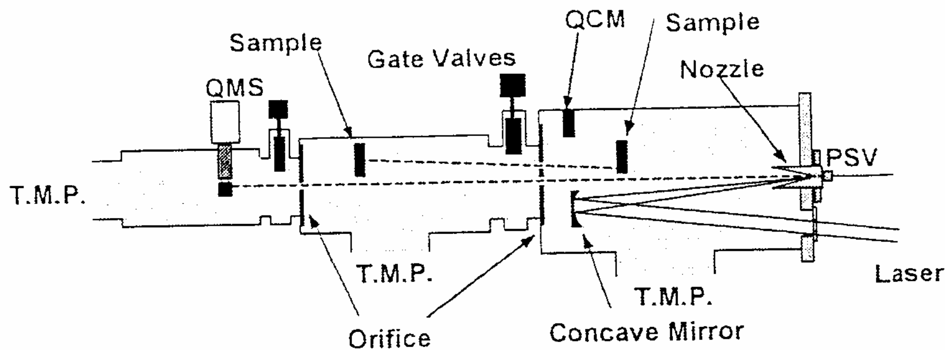

Figure 10. Schematic of Laser Detonation Atomic Oxygen Source.

This type of atomic oxygen source can produce both atomic and molecular oxygen with the O/O_2 concentration ratio of 0.5-3. By adjusting the distance from nozzle to the sample, an atomic oxygen flux higher than 10^{15} atoms cm^{-2} sec^{-1} could be achieved [3].

5.1.2 O_2^+ Source

This source was developed by John Yates and Irene Popova in the Surface Chemistry Department, at the University of Pittsburgh [44]. The source is based on the O_2^+ ions acceleration and their neutralization when they reach the surface of the material.

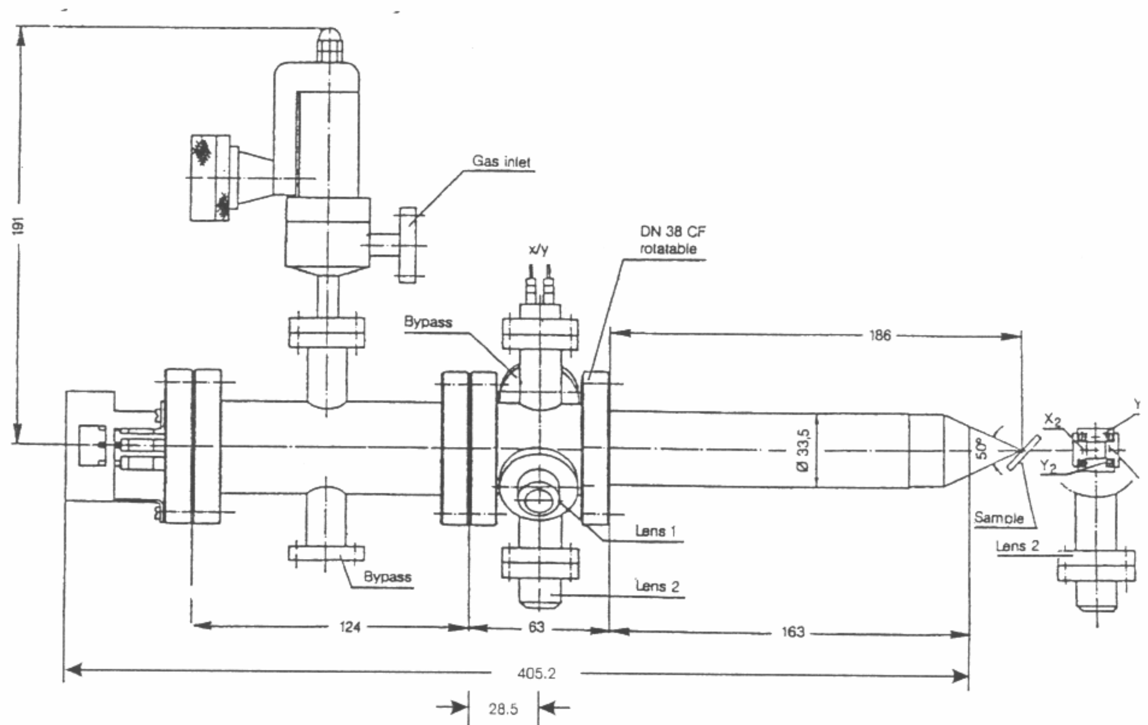

Figure 11. Schematic of O_2^+ source.

The O_2^+ ion is neutralized by the interaction with the surface and O-O bond dissociates producing 2O atoms. With the rapid deacceleration of O_2^+ ions which carry high kinetic energy, the excess kinetic energy is shared between 2O atoms on the target material surface.

5.2 SILICON SURFACE CLEANING

As mentioned in the Deal-Grove oxidation model, surface properties prior to oxidation affect the interface reaction and, consequently, the linear constant rate, B/A. A literature search has been done in order to gain understanding of Si surface properties and oxidation dependence on cleaning methods. There is a multitude of silicon native oxide removing procedures. In a very broad and general way, they can be categorized in the three following methods:

a) Chemical / aqueous etching involving HF, NH_4F or their buffered solutions

b) Thermal etching / annealing where samples are heated by resistance or otherwise to approximately 1050^oC, so that the following reaction occurs:

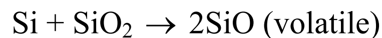

$$Si + SiO_2 \rightarrow 2SiO \text{ (volatile)}$$

c) Mixed methods that involve both chemical and thermal etching along with intermittent UV irradiation, SiH_2 irradiation, thermal oxidation or aqueous oxidation.

Different native oxide removal procedures will influence forming Si/SiO_2 interface and consequent oxide growth in a different way. For example, without UV irradiation, the organic contamination layer present on the native oxide cannot be removed and, consequently, after etching in HF, the surface which has $Si\text{-}CH_2$ bonds is obtained. These bonds are hard to remove even at very high temperatures. Due to this, the cleaning procedure called UV/HF cleaning was developed. The native wafer is cleaned

with UV and the oxide layer is removed by HF solution. H or F termination of Si-dangling bonds is also achievable by varying chemical or thermal treatment [45, 46].

It is also found that there is a difference between the Si/SiO_2 interface for the HF-cleaned Si versus Si surface obtained by repeated Ar ion sputtering and annealing. The thickness of the Si/SiO_2 interface for HF cleaned sample is about twice the thickness as that for a Si surface obtained by the thermal annealing method. The interface becomes broader because the presence of Si-C and Si-H bonds at the interface causes restriction of the oxidation which consequently increases the portion of Si^{2+} and Si^{3+} at the interface.

One of the commonly used procedures for native oxide removal from the Si surface is the RCA etch. The details and exact RCA procedure will be given in the experimental part of this thesis. In short, chemical oxidation of native oxide by sequential peroxide solution is followed by the oxide removal in HF solution. The final consequence of this method is hydrogen (H) - terminated Si surface. Therefore, this method doesn't allow silicon reactive dangling bonds to exist. The initial step is actually F termination of Si dangling bonds, but as Si-F bond is ionic and highly polarized, it allows the HF insertion into the Si-Si bond. Therefore, surface Si is bonded to F while second layer Si is bonded to H. The final step is removal of the Si surface atom in the form of SiF_4, thus resulting in H terminated Si surface [46].

With the thermal annealing procedure, very reactive dangling bonds are produced. SiO_2 is removed from some portions of the surface while the remaining portions are unaffected [47, 48].

5.3 Si - SINGLE CRYSTAL OXIDATION IN LDS

5.3.1 Native oxide removal procedure prior to oxidation

Single crystal silicon (100) and (111) oriented were obtained from MTI Corporation [49]. Samples for AO exposure were cut from double-side polished, boron type doped wafers 4 inch in diameter with resistivity 10-50 ohm cm, thickness 0.5mm and average surface roughness 10 A^o (by AFM).

Experimental procedure consisted of several steps:

1. Samples were cut by diamond scriber from the same single crystal wafer both for AO and MO exposure. All samples were square shaped with the same dimensions (8.5x8.5mm) with diagonal approximately 12mm.
2. Square shaped Si(100) and Si(111) samples were cleaned just prior to exposure in order to remove native SiO_2.

   Prior to AO oxidation, Si samples were cleaned using HF dip. Samples were immersed in 5% aqueous HF for 2min, afterwards specimens were rinsed in deionized water (DI) for 1min and finally blown dry with high purity nitrogen. This type of cleaning procedure produces an atomically rough surface with H-terminated Si-dangling bonds which prevents natural oxide formation for about 10 min. Diffusion of oxygen atoms in the bulk Si is restricted, Si/SiO_2 interface becomes broader and oxidation is very slow even at higher temperatures [46, 50, 51, 52, 53]. In

HF cleaning procedures, rinsing in DI water was done in order to decrease organic contamination during dilution of HF as well as to decrease the residual F on the Si surface.

3. Etched square shaped samples were exposed to AO.

5.3.2 Oxidation conditions

Laser Detonation Source (LDS) at Montana State University (MSU) was used for AO oxidation. The fraction AO in the beam was 70% with mean energy of the hyperthermal AO approximately 5.1eV. Erosion rate of Kapton "witness" sample was used to measure atomic oxygen fluence. The batch of 4 Si samples was loaded in a reaction chamber for the duration of 6.94h at 493K and average flux, 3.2 $x10^{15}$ atoms cm^{-2} sec^{-1}. A total of 50000 pulses with 2 pulses per second were used.

5.4 Si- SINGLE CRYSTAL OXIDATION BY O_2

5.4.1 Native oxide removal procedure prior to oxidation

1. Samples dimensions (20mmx10mm) were cut by diamond scriber from the same single crystal wafer for MO exposure.
2. Prior to MO oxidation, Si samples were cleaned using the RCA etch. Samples were ultrasonically cleaned first with ethanol for 5min, and then with DI water for an additional 5min. Samples were then dipped into 2% HF solution at room temperature

(296K) for 10 sec and dipped into $NH_4OH:H_2O_2$ = 1:1 solution at 353K for 10 min. Additional steps were performed by dipping in DI water for 1 min, 2% HF solution for 10 sec and finally, dipping in DI water for 5 sec. These steps were repeated 3 times.

The consequence of the RCA cleaning procedure is H-terminated Si surface causing Si surface passivity and preventing natural oxide formation for about 10 min in O_2. In both HF and RCA cleaning procedures, rinsing in DI water was done in order to decrease organic contamination during dilution of HF as well as to decrease the residual F on the Si surface [5, 46].

3. Etched square shaped samples were exposed to MO.

5.4.2 Oxidation conditions

Oxidation with MO was performed in a conventional clam-shell, one zone Lybold furnace with a mullite tube controlled by a Eurotherm PID controller. Samples were loaded vertically into the Al_2O_3 boats with the Si surface of interest perpendicular to the MO flow. The temperature was ramped to 493K and P_{O2} of 1atm for 48 hrs.

5.5 Si -SINGLE CRYSTAL OXIDATION IN O_2^+SOURCE

5.5.1 Native oxide removal procedure prior to oxidation

A thermal annealing procedure was used prior to oxidation in order to remove native oxide from the Si surface [47, 50]. This was done in the following steps:

-Heating 900-950K overnight to outgas

-Annealing to 1420-1450K for 30-60sec

-Quick cooling to 1000-1100K

-Holding at that temperature for 120 sec

- Cooling down to 300K at a slow rate of 2K/sec

It was impossible to make a TEM sample out of this material. The reason for that is a flash anneal treatment at 1400K which creates large, pyramidal protrusions on the surface [48, 55]. This is confirmed by other authors, who saw etch pits by SEM. They suggested a flash anneal at 950^oC that produces a chemically clean surface, but with impurities such as C and O [56].

These protrusions are the most probable reason why, after this cleaning procedure, electron transparent area cannot be obtained.

5.5.2 Oxidation conditions

Oxidation was performed in an O_2^+ ion source, at room temperature (25^oC). Flux was $2.55 x 10^{13}$ atoms cm^{-2} sec^{-1} and the exposure duration was 2 hrs.

Table 2 summarizes experimental conditions for all samples as far as native oxide removal and oxidation conditions are concerned.

Table 2. Experimental conditions.

Sample	Cleaning method	Oxidizing species	Exposure time (hrs)	Flux (at/cm^{2}sec)	Temperature (oC)	Equipment
Si(100) p-type	HF	Atomic Oxygen (AO)	6.94	3.2 x 10^{15}	220	Laser Detonation Source (LDS)
Si(111) p-type	HF	AO	6.94	3.2 x 10^{15}	220	(LDS)
Si(100) p-type	Thermal annealing	O_2^+	2	2.55 x 10^{13}	25	O_2^+ Ion Source
Si(100) p-type	RCA	O2	48	pO_2 =1 atm	220	Furnace
Si(111) p-type	RCA	O2	48	pO_2 =1 atm	220	Furnace
Si(100) n-type		O2	19	pO_2 =1 atm	800	Furnace

After oxidation was performed, samples were placed in separate sample boxes and kept in a desiccator until the characterization procedure.

6.0 CHARACTERIZATION TECHNIQUES AND RESULTS

The silicon oxides created by atomic and molecular oxygen species were characterized by different techniques: Rutherford Backscattering (RBS), High-Resolution Transmission Electron Microscopy (HRTEM), Selected Area Electron Diffraction (SAED), Electron-Energy Loss Spectroscopy (EELS), X-Ray Photoelectron Scattering (XPS) and Atomic Force Microscopy (AFM). The description of the characterization methods used will be given in following chapters.

Experiments were planned carefully in a manner that non-destructive characterization methods were used first since the amount of samples oxidized with atomic oxygen was limited. Experimental data and results will be presented and the comparison with the relevant previous work done in this area will be given.

6.1 RUTHERFORD BACKSCATTERING SPECTROMETRY (RBS)

RBS method is based on the collisions between atomic nuclei. It measures the number and the energy of the backscattered ions in the beam after the collision with the atoms in

the near-surface area of the specimen. RBS typically uses high energy (1-3.4MeV) He ions.

The beam consists of the monoenergetic and collimated alpha particles impacting the target under the 90° angle. For the case when the sample is very thin, the beam can be transmitted with almost no or very small energy losses. For the thicker samples, the only scattered particles that can be detected are those which are scattered backwards by angles more than 90° relative to the incident beam direction.

These alpha particles are ^4He nuclei, which are generated in the ion source. They gain energy by acceleration in the accelerator. Series of devices collimate or focus the beam and select a particular type of particle and energy by filtering. After that, the beam goes into the scattering chamber eventually impacting the target or the sample to be analyzed. He ions penetrate up to 2 microns into the sample and during this process the ions lose energy continuously through the series of electronic scattering events. When the ion collides with the nucleus, it is backscattered with a discrete, large energy loss, which is characteristic for a particular atom. Continuous energy losses define depth of traveling of the ion through the material. Based on this, the elemental composition and depth distribution of certain elements can be determined.

Electrical signals are generated by some of the backscattered particles caught by the detector. The final output is a backscattered spectrum. The detection limit ranges from few parts per million (ppm) for heavy elements to a few percent for light elements. Depth resolution is ~2nm near the sample surface [57].

The RBS technique was used for precise measurements of the silicon oxide thickness. Use of such a method is very important since we predict that atomic oxygen

forms thicker oxide than the molecular oxygen. Determination of the exact oxide thickness is crucial in concluding about the possible oxidation mechanisms.

6.1.1 Rutherford Backscattering Spectroscopy (RBS)-Results

Rutherford Backscattering Spectroscopy was utilized in order to measure the thickness of the thin silica films non-destructively. The lower limit of this method for thin films thickness measurement is ~10A^o. The RBS experiments were performed on a Tandetron accelerator using 3.01 MeV He^{++} beam with a 3mm diameter spot. Spectra were acquired with a beam to detector angle of 15° and a beam to sample normal angle of 0°. The computer software SPECON V 1.54 enabled us to convert and process data obtained in RBS measurements [58].

Total SiO_2 concentration (molecules cm^{-2}) was obtained and then converted into the SiO_2 layer thickness by assuming a SiO_2 atomic density of 2.27x10^{22} molecules cm^{-3} [49]. The thickness of the silica was determined by using following formula:

$$(Nt)_i = (A_i / H_{Si})(\sigma_{Si} / \sigma_o)(E / [\varepsilon]_{Si}^c) \quad \text{(Equation 21)}$$

where

$(Nt)_i$= number of SiO_2 cm^{-2}

A_i = total number of counts integrated over the oxygen signal

H_{Si} = scattering yield from the Si substrate

σ_{Si} / σ_o = scattering cross section ratio for Si and O

E = channel width (energy / channel)

$[\varepsilon]_{Si}^c$ = stopping cross section factor of Si

Given in Figure 12 are RBS spectra recorded for the Si –single crystal samples oxidized with different species.

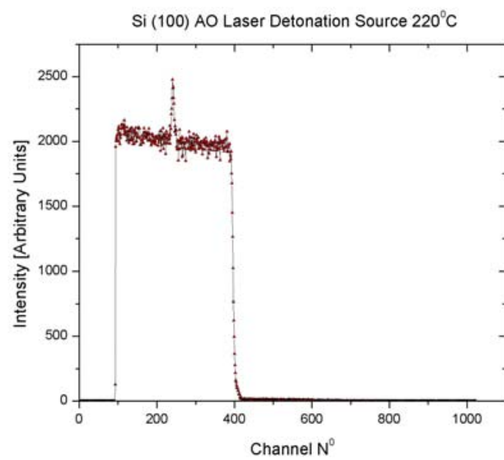

a)

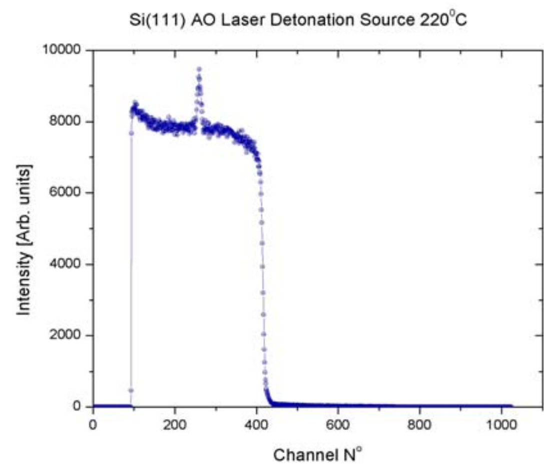

b)

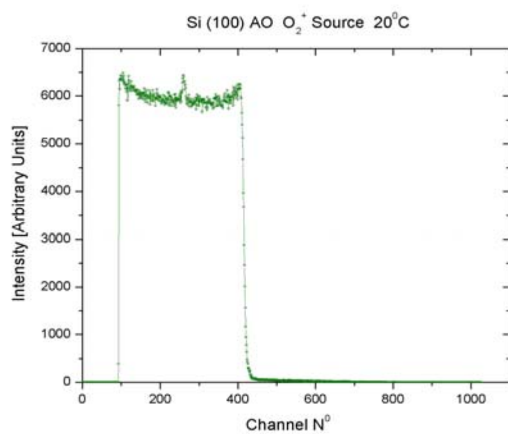

c)

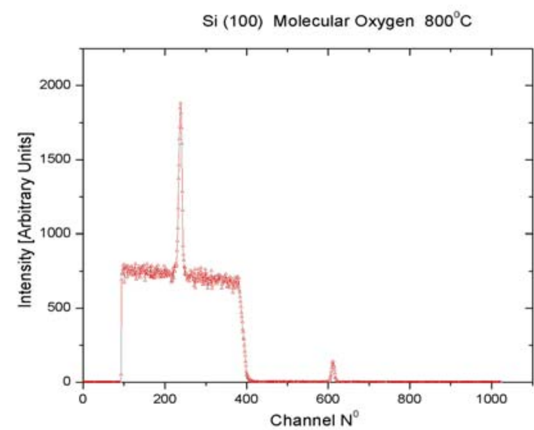

d)

Figure 12. RBS spectra from Tandetron accelerator recorded from a) Si(100) oxidized in LDS b) Si(111) oxidized in LDS c) Si(100) oxidized in O_2^+ source and d) Si(100) oxidized in O_2, used for calibration.

For the silica thin layer thicknesses, determination of A_i, which represents the total number of counts integrated over the oxygen signal and H_{Si}, representing scattering yield from the Si substrate was done from the collected RBS spectra. Example of thickness calculation for Si(111) oxidized by atomic oxygen in LDS:

A_i = 15305.9 counts; H_{Si} = 7200 counts (from figure 12-b)

E=4.75 eV/channel σ_O / σ_{Si} =6.53

$[\varepsilon]_{Si}^c$ =77x10^{15} eVcm^2 (determined by linear extrapolation for 3 MeV, from table VIII, page 366 of [57].

Using equation 21 and assuming SiO_2 atomic density of 2.27x10^{22} molecules cm^{-3}, silica layer thickness is calculated:

$$t_{SiO_2} = 8.73x10^{-7}\,cm = 87.3A^o$$

Table 3 gives calculated oxide layer thicknesses from the RBS spectrums shown in the Figure 12.

Table 3. Calculated oxide thicknesses using RBS spectra.

Sample	**Thickness (A^o)**
Si(100) AO (LDS)	58.3
Si(111) AO (LDS)	87.3
Si(100) O_2^+	27.8
Si(100) O_2	748

Thick silica (~80nm) on Si substrate was used as a standard to calibrate the number of SiO_2 per square centimeter (Figure 12-d) [57].

From the RBS spectrum of Si(100) (Figure 12-a) and Si(111) (Figure 12-b) oxidized in atomic oxygen (LDS), oxide thickness of 5.8nm and 8.7nm were determined, respectively, which is in very good agreement with the oxide thickness of 5-6nm for Si(100) and 7-8nm for Si(111) measured by HRTEM (Figure 16-a and 20-a, respectively). The silica thickness of 28 A^o was calculated from the RBS spectrum of Si(100) oxidized in O_2^+ source (Figure 12-c) while Si(100) oxidation for 19hrs at 800^oC created 748 A^o thick oxide (Figure 12-d).

6.2 TRANSMISSION ELECTRON MICROSCOPY (TEM)

6.2.1 Electron-Specimen Interactions

In Transmission Electron Microscopy, acceleration of electrons up to very high energy and voltages levels, generally few hundreds keV is done. Such fast electrons can cause many interactions when focused on a material. Different types of signals are obtained: X-rays, light, Auger electrons, etc.

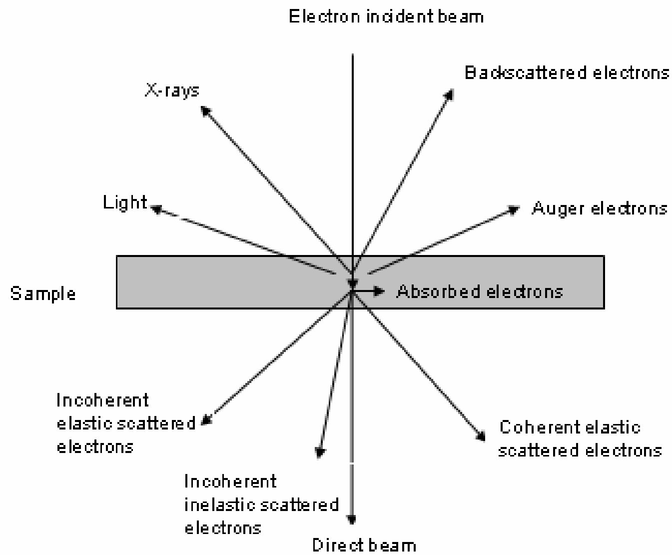

Figure 13. Possible electron-matter interactions [59].

Beam electrons experience several different main phenomena while traveling through the specimen:

1. They can pass straight through the specimen without interaction, thus forming the undeflected transmitted beam. There is no information about the sample associated with these electrons.

2. Electrons can interact with the sample –**scattering phenomena**

The wave originated from the distant electron source is considered as a planar wave while the wave scattered from an atom has spherical geometry.

Scattering

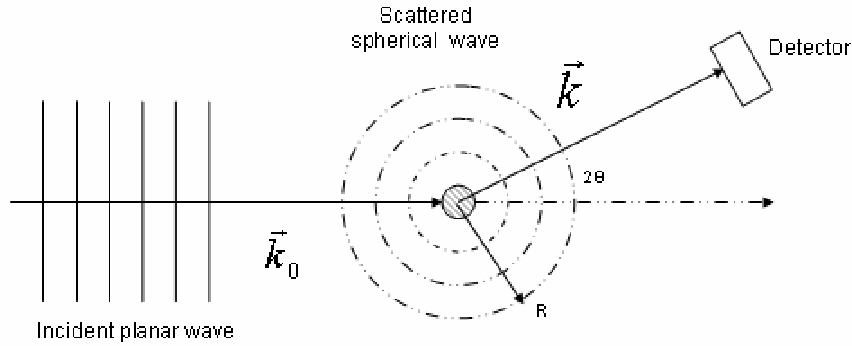

Figure 14. Schematic of scattering process [60].

Planar wave is given by:

$$\Psi_0 = A_0 e^{2\pi i \vec{k}_O \vec{r}} e^{-i\omega t} \qquad \text{(Equation 22)}$$

For a spherical scattered wave, we have:

$$\Psi_s = \frac{A_0 f'}{R} e^{2\pi i \vec{k}\vec{R}} e^{-i\omega t} \qquad \text{(Equation 23)}$$

where k_o and k are incident and scattered outgoing wave vectors, ω is wave frequency and f' represents scattering length (amplitude).

$$\left|\vec{k}_o\right| = \frac{1}{\lambda} \qquad \text{(Equation 24)}$$

where λ is the wavelength of the incident electron beam.

It can be seen that for small λ, the incident wave vector k_o becomes very large, causing Ewald sphere to become almost flat. This effect is particularly important in TEM since it provides planar sectioning through the reciprocal space.

f' represents the strength of the scattering process.

$$f_e^{'} = \frac{e^2}{mc^2} p$$ (Equation 25)

where $\frac{e^2}{mc^2}$ = 2.82x10^{-13} cm – "classical radius of the electron"

p is polarization factor given by:

$$p = \left(\frac{1 + \cos^2 2\theta}{2} \right)^{1/2}$$ (Equation 26)

Scattering amplitude is given by the formula:

$$f_e(\vec{k}) = \frac{2\pi me}{h^2} \int \rho(\vec{r}) e^{2\pi i \vec{k}\vec{r}} d\tau_r$$ (Equation 27)

$\rho(\vec{r})$ defines the amount of electrons in $d\tau_r$ volume element, or electron density

Intensity scattered into detector:

$$I_s = \Psi_s \Psi_s^* = |\Psi_s|^2 = \frac{f_e^{'} A_o^2}{R^2} = \frac{KI_o}{R^2} = \left(\frac{1 + \cos^2 2\theta}{2} \right)$$ (Equation 28)

where I_o is the intensity of the incident beam and $K = \left(\frac{e^2}{mc^2} \right)^2$

3. In the case of coherent scattering, constructive or destructive interference takes place depending on the relationship between the phases of the scattered and incident waves.

$$\Psi_{coh} = \sum_{r_j} \psi_{r_j}$$ (Equation 29)

Ψ_{coh} = total scattered wave amplitude resulting from summation of the wavelets amplitudes ψ_{r_j} .

r_j= location in the specimen from which the wavelets is scattered

Total coherent intensity I_{coh} is defined as:

$$I_{coh} = \left| \sum_{r_j} \psi_{r_j} \right|^2 = \Psi^*_{coh} \Psi_{coh} \quad \text{(Equation 30)}$$

4. In incoherent scattering, scattered and incident wavelets do not preserve phase relationships; therefore, there is no destructive or constructive interference.

The total incoherently scattered intensity I_{incoh}, is created by adding incident and scattered wavelets intensities I_{r_j}, not their phase amplitudes.

$$I_{incoh} = \sum_{r_j} I_{r_j} = \sum_{r_j} \left| \Psi_{r_j} \right|^2 \quad \text{(Equation 31)}$$

Elastic scattering arises mostly due to the Coulomb interaction between the incident electron and the nucleus. Energy-loss via kinetic energy transfer is negligible since the target atom is far more massive than the scattered electron [59]. It conserves kinetic energy of the wave after scattering.

5. Inelastically scattered electrons loose energy due to the Coulomb interactions with the atomic electron and are concentrated in the range of smaller scattering angles. Coherent elastic scattering is useful for diffraction experiments and allows investigation of the internal structure of the materials.

Incoherent inelastic scattering is used in the spectroscopy methods (EDS and EELS).

The other two scattering phenomena possibilities are coherent inelastic and incoherent elastic scattering. Scattering cross-section σ is the key quantity in both inelastic and elastic scattering and is defined as probability of an interaction between the incident and atomic electron to occur.

$$\sigma = \frac{n_s}{n_t n_i} \qquad \text{(Equation 32)}$$

where n_s is the number of scattering events per unit area, n_t is the number of target atoms per unit area and n_i is the number of incident electrons per unit area.

6.2.2 TEM components

TEM incorporates very powerful methods that allow microstructural and analytical material characterization. Intensity of the electrons transmitted through the specimen is seen as an image in TEM. TEM is composed of following sections: illumination system, imaging system and detection system.

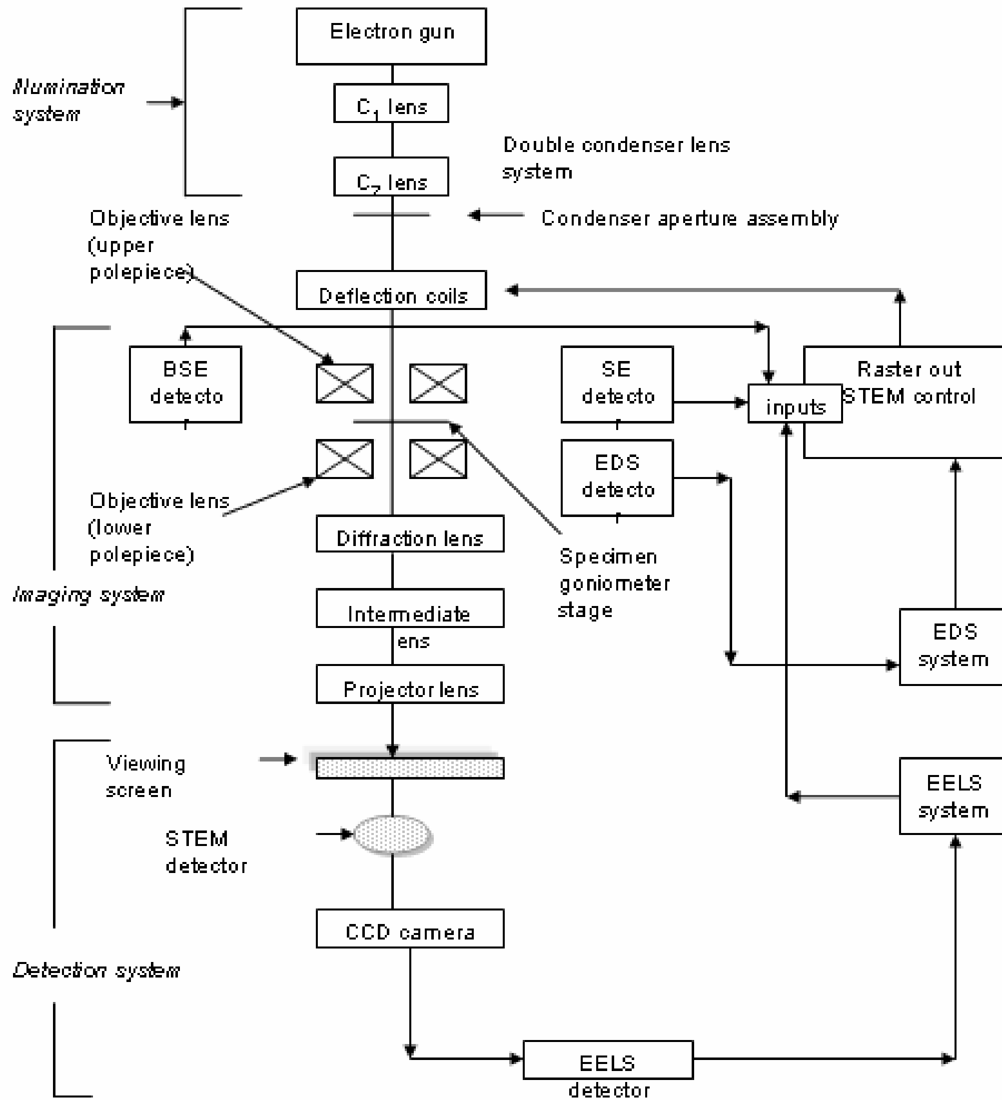

Figure 15. Block diagram of the main components of TEM with STEM capabilities [61].

Illumination system

The electron gun provides a monochromatic electron beam. There are several different gun types used in TEM. Thermionic electron guns (triode guns) consist of the filament, Wehnelt cap and the anode. The filament can be tungsten wire or LaB6.

Schottky and field emission guns use typically tungsten filament and cold field emitter and requires 10^{-8}Pa vacuum while Schottky needs 10^{-6} Pa.

The illuminating stage or pre-specimen lenses. Condensor lens 1 is positioned close to an anode in order to create parallel incident electron beam and very fine probe on the surface. Condensor lens 1 is followed by the first condenser aperture, which captures electrons that deviate largely from the optical axis. Diameter of the crossover formed by the condenser lens 1 can be decreased by strong excitation of that lens. In order to decrease further the probe size, second lens known as condensor 2 is added. A pair of condenser lenses act to illuminate the specimen with a parallel beam of electrons. Condenser lens 1 is usually kept at some setting recommended by the manufacturer. The angle of beam convergence and consequently the beam coherence is adjustable by using smaller condenser lens 2 aperture.

Imaging system

Objective lens characterized by the magnetic field and sample immersed in it. This lense is used to further demagnify the incident probe, eventually reaching nanometer size probe. The purpose of the objective lens is to bring the various diffracted electron beams into the cross-over.

Magnification or post-specimen lenses and projection system usually composed of 3 or more lenses. The post-specimen part of the objective lens is introduced in order to magnify the image. Following these lenses are diffraction, intermediate, and projector lenses. A diffraction lens is needed in order to reduce combined effects of lens aberrations. The intermediate lens is used to regain control over the magnification of the system. A projector lens is needed in order to achieve variable magnification.

Detection system

Detector (viewing screen or CCD camera), which should be sensitive down to single electron and characterized by high spatial resolution and low noise level as well as reproducibility.

Mentioned above are just main parts of TEM, however, energy dispersive analyzer for x-rays (EDS) or electron energy loss spectrometer (EELS), imaging energy filters, etc can be added.

Lens Defects

Astigmatism occurs due to the electron beam deflection, which can arise because condenser lens 2 aperture is imperfectly machined, dirty and charging up or it is misaligned. Image distortion caused by astigmatism is defined as:

$$r_{ast} = \beta \, \Delta f \qquad \text{(Equation 33)}$$

where β is the semiangle of collection of the lens aperture and Δf represents the maximum difference in focus caused by astigmatism. This distortion can be corrected by using condenser stigmators that introduce compensating field.

Spherical aberration defines the minimum probe size achievable. It is caused by the lens field non-homogeneity. The electron that is far away from the axis will experience stronger bending towards the axis. This aberration is of most concern in the objective lens since the image seen by the microscopist is directly influenced by it. Spherical aberration disc radius r_{sph} is defined as:

$$r_{sph} = C_s \, \beta^3 \qquad \text{(Equation 34)}$$

where C_s is the spherical aberration coefficient and it is a constant for particular lens and

β is the semiangle of collection of the lens aperture [62] .

6.2.3 Major TEM techniques

These include bright (BF) and dark field (DF) imaging, selected area electron diffraction (SAED), convergent beam electron diffraction (CBED), high-resolution TEM (HRTEM), Z-contrast technique, energy-dispersive x-ray spectroscopy (EDS) and electron energy loss spectroscopy (EELS).

Bright field (BF) image is created if only transmitted beams (electrons) are passed through the objective aperture.

Dark field (DF) image is created if some of the diffracted electrons are passed through the objective aperture.

Contrast in BF and DF images is usually "diffraction contrast" or the variations in intensity of diffraction across the sample. Diffraction contrast depends on Laue condition satisfaction, active diffraction and the value of the deviation parameter s [62].

6.2.4 TEM Sample Preparation-Experimental

Cross-sectional TEM samples were prepared by cutting 2 mm strips out of oxidized square samples of Si , gluing these peaces face- to -face using Gatan G-1 epoxy, placing them in the grooved copper rod 2.3 mm in diameter and finally placing the rod into the

copper tube. The samples were then cut from the copper tube assembly, ground (mechanically polished) to 100 μm using hand grinder. Double side dimpling was done until central the thickness 20-25 μm was reached and dimple grinder model 656 was used. Samples were finally ion polished using Gatan PIPS model 691 to obtain the electron transparent area.

Plan view TEM samples were prepared by cutting a 3 mm discs using an ultrasonic disc cutter, one side hand ground to 50 -μm thickness, one side dimpled and finally ion polished to obtain electron transparent area.

6.3 HIGH RESOLUTION TRANSMISSION ELECTRON MICROSCOPY (HRTEM)

The high-resolution technique uses phase-contrast imaging to form images of columns of atoms. The phase of the diffracted electron wave is preserved and interferes constructively or destructively with the phase of transmitted wave. This type of imaging is based on coherent elastic scattering.

An HRTEM image represents an interference pattern between the forward-scattered and diffracted electron waves from the sample. If ψ_o and ψ_g represent amplitude of the forward scattered and diffracted beams respectively, then the resulting image amplitude obtained by the superposition of the two waves in the image plane will be given as:

$$\Psi = \psi_o + \psi_g e^{-iW(\theta_g)} \qquad \text{(Equation 35)}$$

where $W(\theta_g)$ is the wave aberration in the diffracted beam , or instrumental phase shift (distortion) which depends on the spherical aberration and focus of the objective lens [62] . The magnitude of $W(\theta_g)$ is the largest for the waves that are bent further from the optical axis. Recently, spatial (point) TEM resolution reached 1.5 A^o, and this limit has recently decreased below 1.35 A^o using spherical aberration constant C_s corrected objective lens [63].

Distribution of the atoms in the material is determined by the scattering factor distribution, ρ(r).The diffracted wave is actually the Fourier transform of the scattering factor distribution in the medium. The expression for the Fourier transform of ρ(r) of the atoms distribution within the sample is:

$$F(\rho(r)) = \frac{1}{\sqrt{2\pi}} \int_{-\infty}^{+\infty} \rho(r) e^{-i\Delta k \cdot r} d^3 r \qquad \text{(Equation 36)}$$

where $\Delta k = k_o - k$ is a diffraction vector and has units A^{o-1}, and therefore, represents atom periodicities in the material [60] . This means that short periodicities of ρ(r) are associated with a Fourier transform having large vectors Δk .

High-resolution images are affected by focus and specimen thickness. Also, instrumental conditions such as high electronic stability of acceleration voltage and lens currents, vibrational-free mechanical stability, high gun brightness, already mentioned low spherical aberration constant C_s, etc. influence HRTEM [61] .

HRTEM method was used to precisely determine silicon-oxide thickness. Except the oxide thickness determination, this method enables us to visualize and conclude about the oxide morphology and microstructure. Since its capability is atom columns imaging, it gives excellent insight in the Si/SiO_2 interface properties.

6.3.1 High Resolution Transmission Electron Microscopy (HRTEM) - Results

HRTEM was used in order to determine thicknesses of the oxide and Si/SiO_2 interface formed by atomic and molecular oxidation of Si(100) single crystal.

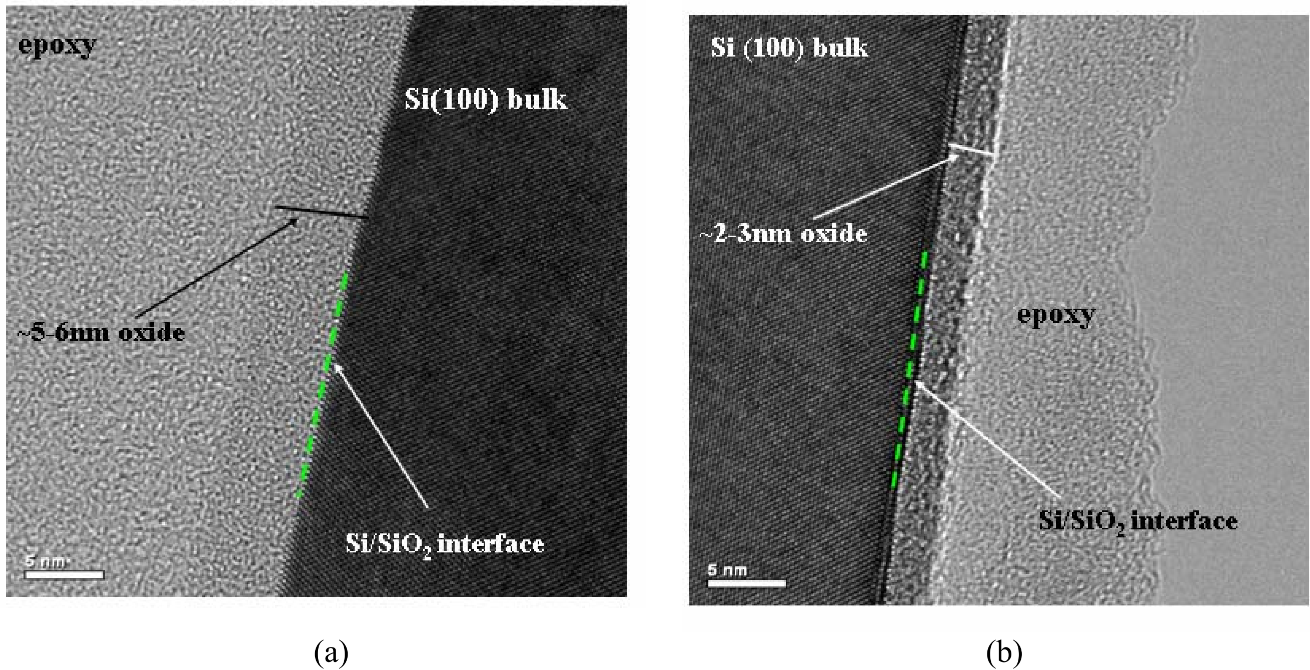

(a) (b)

Figure 16. Cross-sectional HRTEM micrographs of the silicon oxide layer formed on Si(100) oxidized by a) atomic oxygen b) molecular oxygen.

The silicon oxide created by atomic oxygen on Si(100) has an average thickness of 5nm, while the passivated layer formed by molecular oxygen was only 3nm thick. Oxide created with atomic oxygen appeared uniform in thickness and the Si/SiO_2 interface was found to be very sudden and abrupt. No clear evidence of secondary phases, cavities or voids was found [64].

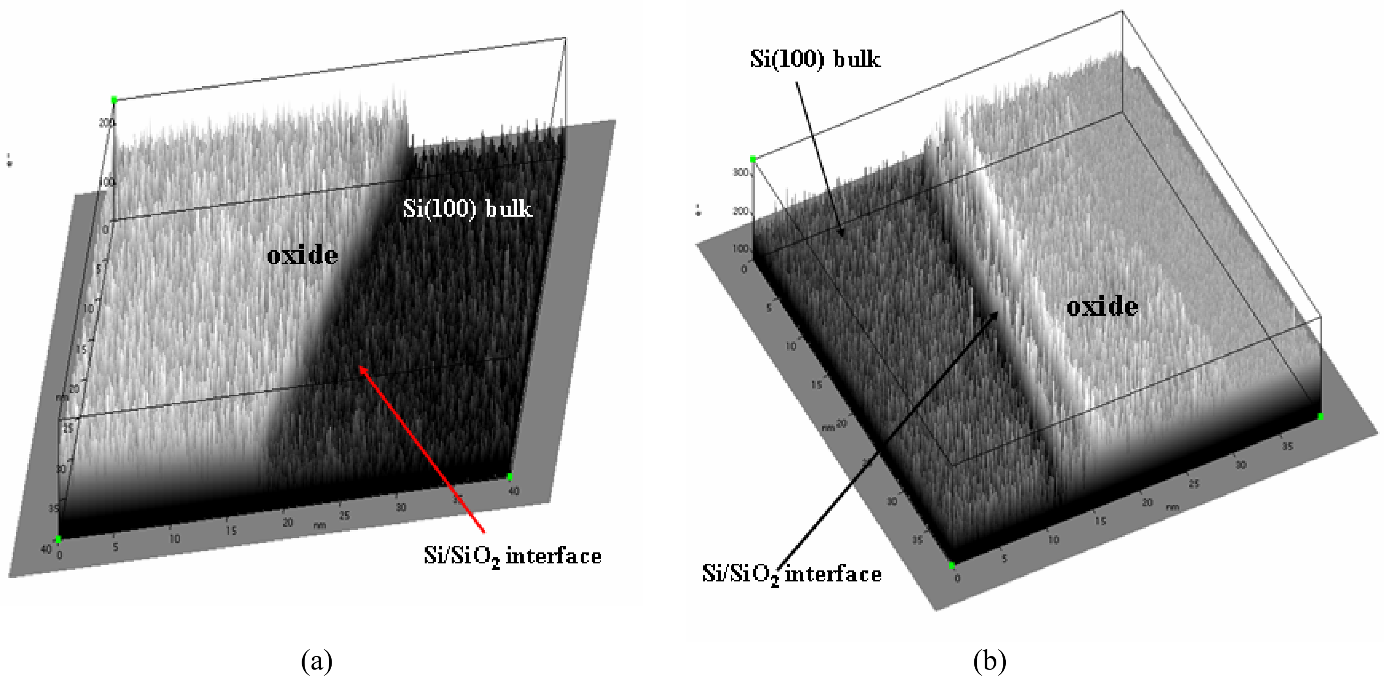

Figure 17. 3D view of cross-sectional HRTEM micrographs of the silicon oxide layer formed on Si(100) oxidized by a) atomic oxygen b) molecular oxygen .

From 3D representations of cross-sectional images, it appeared that Si/SiO_2 interface formed with atomic oxygen is very smooth and abrupt while molecular oxygen oxidation creates thick interface region. Sampled area was 40x40nm and 35x35nm for Si(100) oxidized by atomic and molecular oxygen, respectively.

In order to determine the thickness of the transitional interface region, intensity profiling method was used on HREM micrographs.

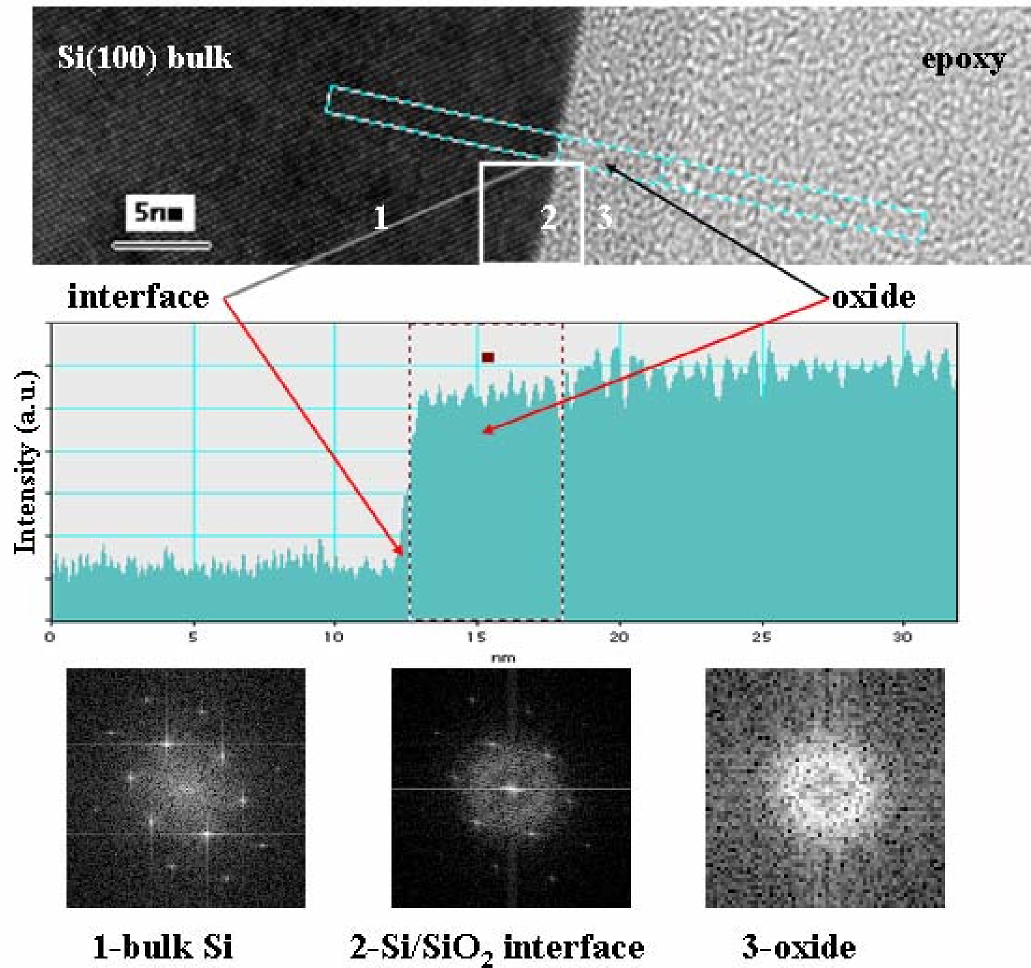

Figure 18. Intensity profiles and Fourier transforms obtained from cross-sectional HRTEM micrographs of the silicon oxide layer formed on Si(100) oxidized by atomic oxygen.

Fourier transforms are done on the areas of the sample enclosed by the square shown on the HRTEM micrograph. Position 1 in Figure 18 refers to the bulk Si, position 2 to Si/SiO_2 interface and position 3 is taken in the bulk oxide.

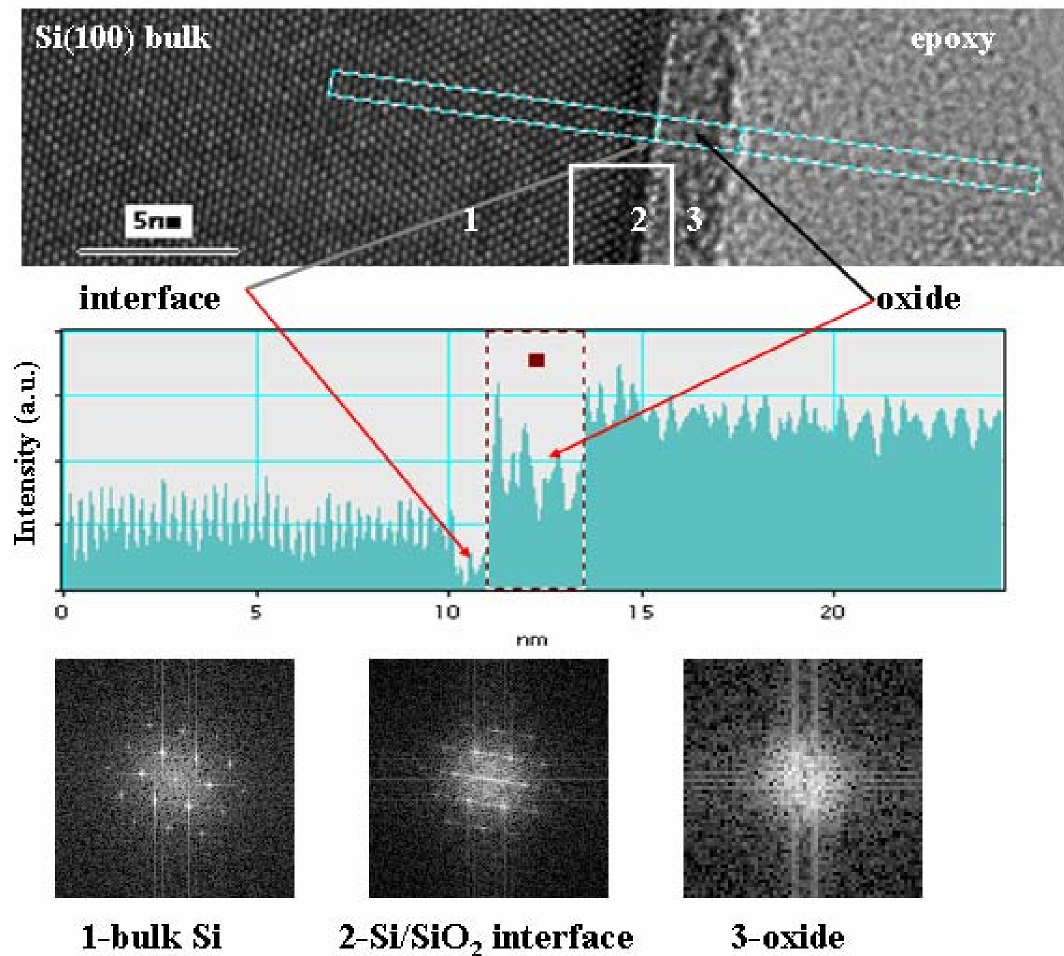

Figure 19. Intensity profiles and Fourier transforms obtained from cross-sectional HRTEM micrographs of the silicon oxide layer formed on Si(100) oxidized by molecular oxygen.

Intensity profiles across the Si/SiO_2 interface created by atomic and molecular oxygen on Si(100) are given in Figure 18 and Figure 19, respectively. Intensity plots are obtained by averaging intensities vertically in the area enclosed by the rectangle. This analysis carried out using Gatan Digital Micrograph software features [65]. Profile imaging of the HRTEM micrographs technique was used by Takeguchi et al. to study structure and growth kinetics of the Si(001) surface of a nanometer-sized Si multiply

twinned particle [66] . Intensity profiling across the Si/SiO_2 interface shows that almost no interfacial layer is present for atomic oxygen oxidized Si(100) (Figure 18), whereas ~1 nm interfacial layer is found to exist for O_2 oxidized Si(100) (Figure 19).

The oxide layer formed on a Si(111) single crystal by atomic and molecular oxygen oxidation is shown in Figures 20-a and 20-b, respectively. The silicon oxide created by atomic oxygen on Si(111) has an average thickness of 7-8nm, while a passivated layer formed by molecular oxygen was 3-5nm thick. This result is in agreement with the well known fact that reaction rate for the (111) orientation is 1.7 times higher than the reaction rate of (100) orientation.

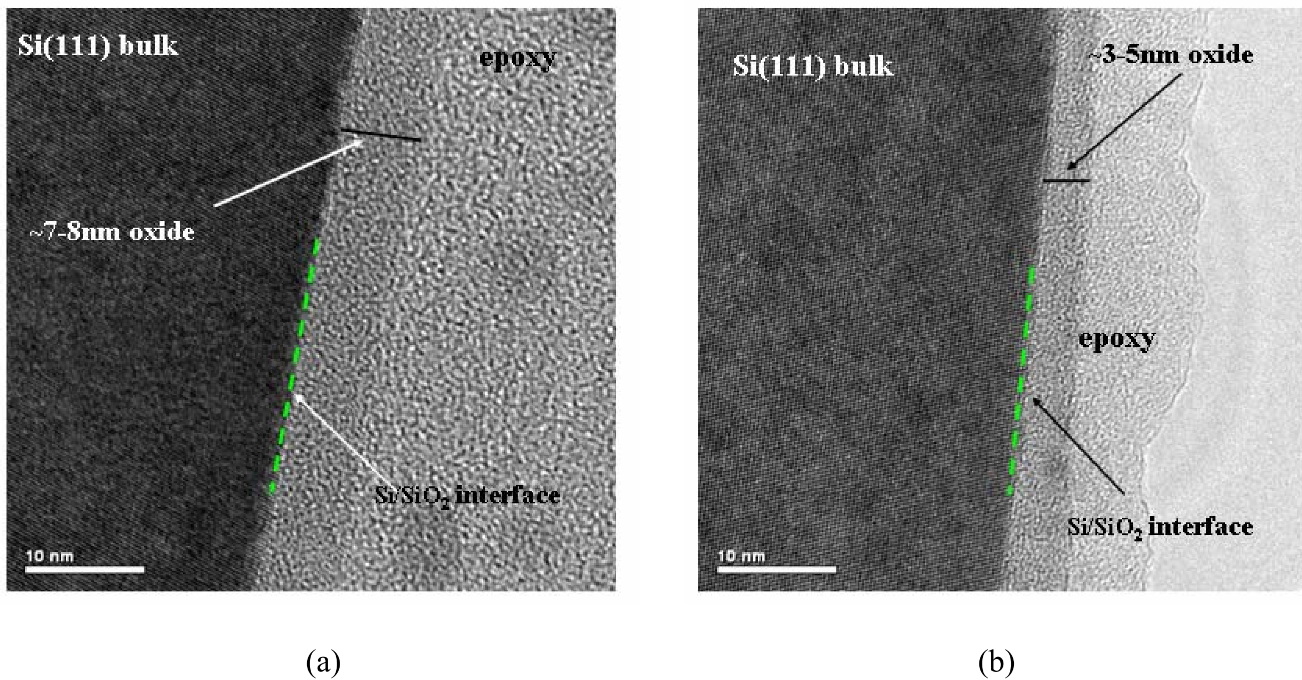

Figure 20. Cross-sectional HRTEM micrographs of the silicon oxide layer formed on Si(111) oxidized by a) atomic oxygen b) molecular oxygen.

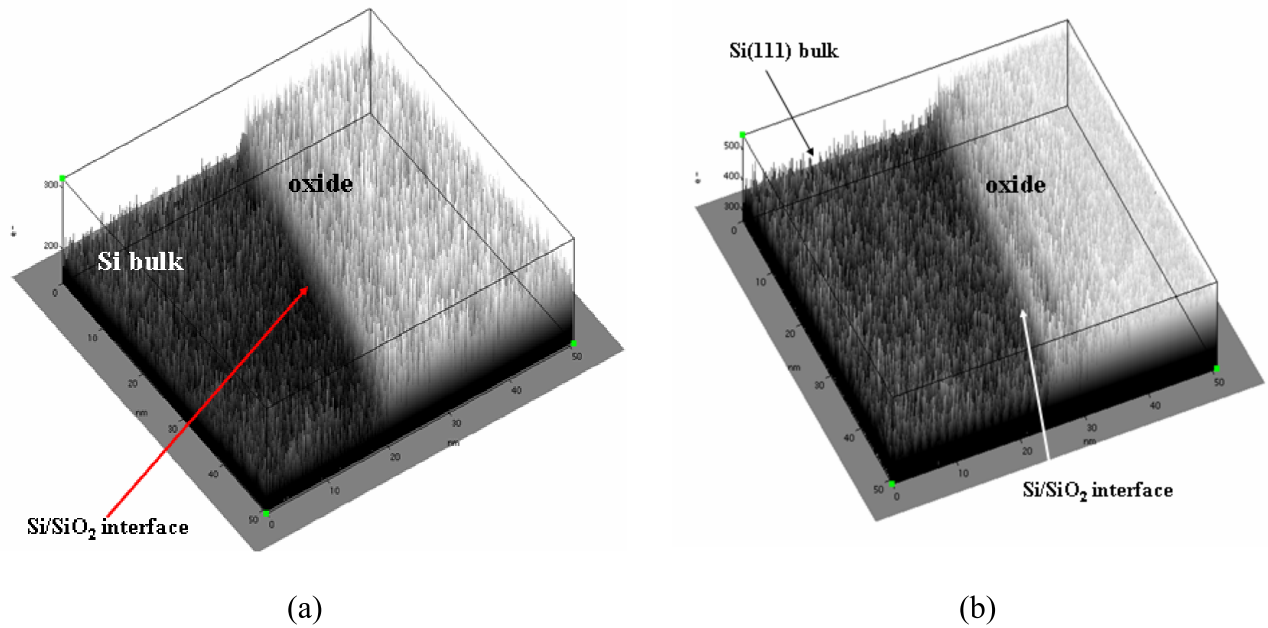

(a) (b)

Figure 21. 3D view of cross-sectional HRTEM micrographs of the silicon oxide layer formed on Si(111) oxidized by a) atomic oxygen b) molecular oxygen.

Sampled area shown on 3D representations of X-TEM micrographs, in Figure 21, was 50x50nm for Si(111) oxidized by atomic and molecular oxygen.

Si/SiO_2 interface formed with atomic oxygen on Si(111) is smooth and abrupt (similar to the (100) orientation), but molecular oxygen oxidation creates not so thick interface region as compared to the ~1nm thick interface formed on Si(100).

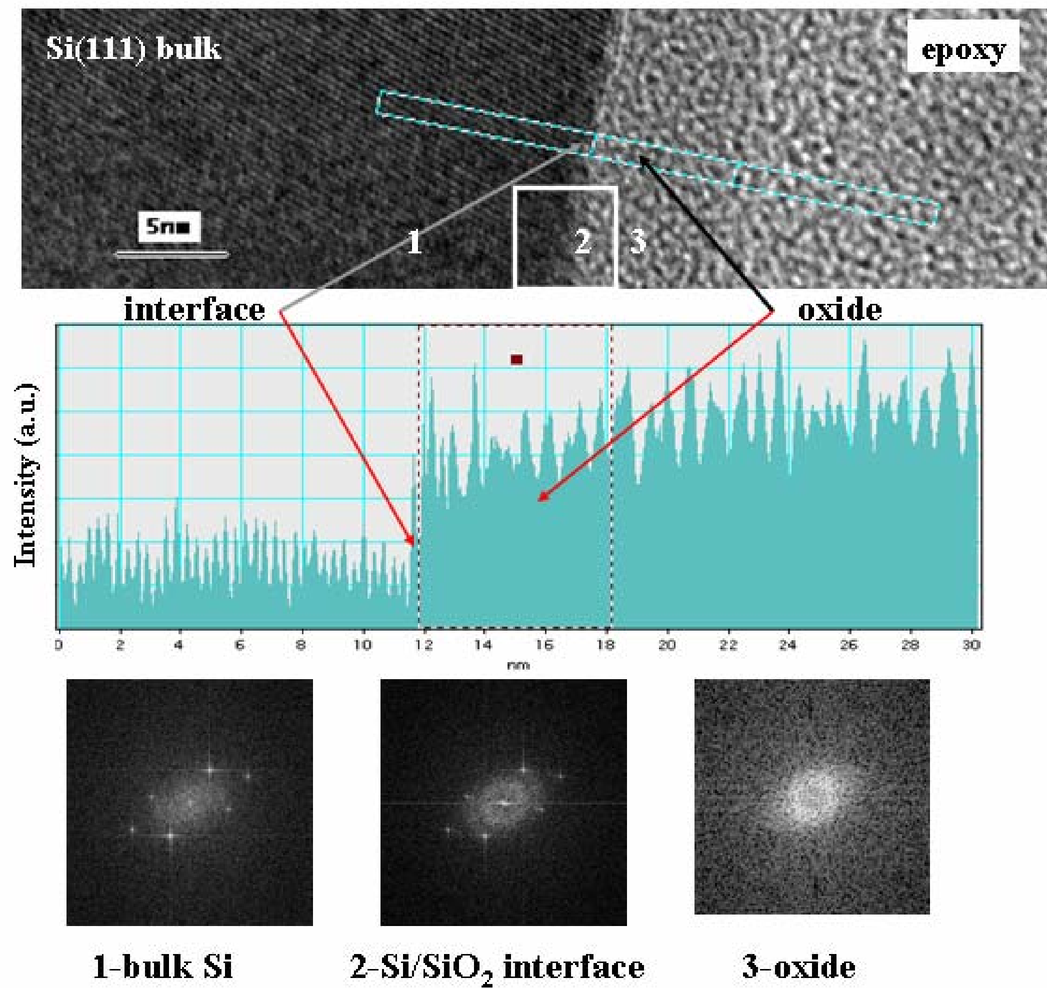

Figure 22. Intensity profiles and Fourier transforms obtained from cross-sectional HRTEM micrographs of the silicon oxide layer formed on Si(111) oxidized by atomic oxygen.

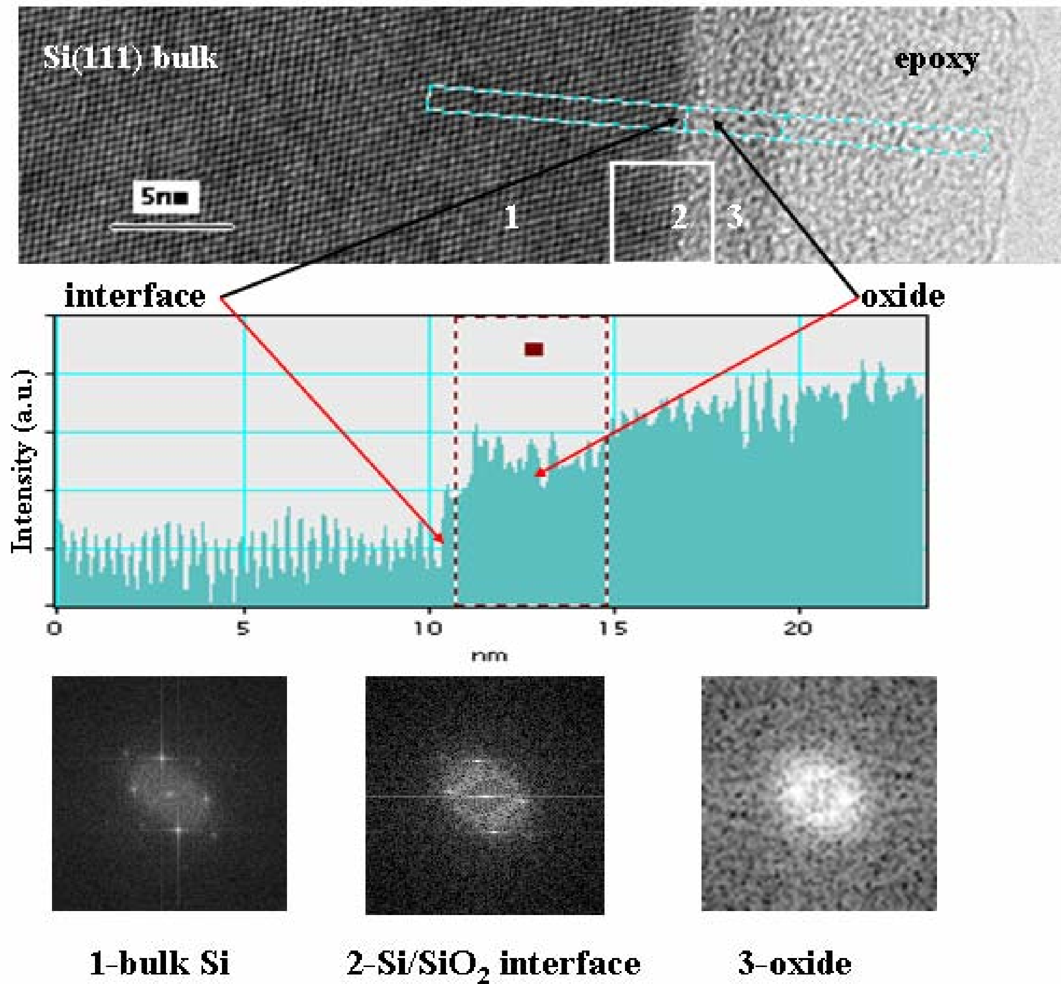

Figure 23. Intensity profiles and Fourier transforms obtained from cross-sectional HRTEM micrographs of the silicon oxide layer formed on Si(111) oxidized by molecular oxygen.

Intensity profiling of HRTEM micrographs showed that AO forms smooth and abrupt Si/SiO_2 interface on Si(111), but this effect is more pronounced for (100) orientation-rather abrupt interface is created both by AO and O_2 species on a Si(111) single crystal.

6.4 SELECTED AREA ELECTRON DIFFRACTION (SAED)

SAED is used to create a diffraction pattern from the selected area on the specimen. TEM allows observation of both an image, corresponding to information in the real space, and an electron diffraction pattern representing material information in reciprocal space. An intermediate aperture is used to ensure that the signal is coming only from the selected feature of interest in the imaging mode.

In the case when the incident beam is scattered only once by the matter, it can be interpreted by kinematical diffraction approximation. On the other hand, electrons can be scattered many times and diffracted beam scattered again goes into the direction of either the transmitted or different diffracted beam. This multiple scattering can be described by the dynamical diffraction theory.

Different kinds of diffracted patterns can be created depending on the structure of the analyzed material. Single-crystal, polycrystalline material and amorphous material produce spot, ring and diffuse haloes pattern, respectively [60, 61, 62].

Diffraction phenomena

Only coherent scattering can lead to diffraction and a precise relationship between the phases of the incident and scattered wave is required. Constructive or destructive interference of the phases from different atoms along different angles in the sample takes place in diffraction.

Constructive interference occurs when the path difference is an integer number n of wavelengths λ, so that Bragg's law, $2d\sin\theta=n\lambda$, is satisfied. For only certain values of θ scattering from all parallel planes will add up in phase resulting in a strong diffracted

beam. Bragg's law represents a consequence of lattice periodicity not referring to the basis of the atom. Relative diffraction intensity is determined by the basis (motif) composition.

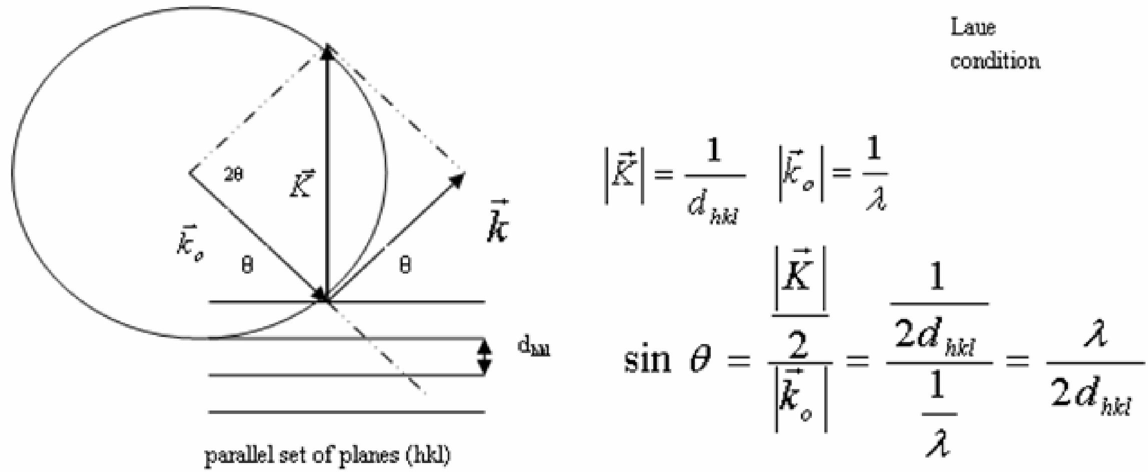

Figure 24. Ewald sphere construction [60].

Center of the Ewald sphere is at the origin of the incident beam.

Bragg's law $\lambda = 2d_{hkl} \sin\theta$ (Equation 37)

gives the necessary geometric condition for constructive interference (diffraction).

The condition for constructive interference is that the reciprocal lattice point, $\vec{r}^{\,*}_{hkl}$ lies on the Ewald sphere. The total amplitude of electron wavelets scattered coherently and elastically from the unit cell is:

$$F = A_c = \sum_j \Delta A_j = \sum_{j=1}^{n} f_j e^{2\pi i \Delta \vec{k} \vec{r}_j}$$ (Equation 38)

and it is known as Structure Factor F.

ΔA_j is amplitude scattered from the jth atom with the fractional coordinates u_j, v_j and w_j, at the position r_j.

$$\Delta A_j = f_j e^{i\phi_j} \qquad \text{(Equation 39)}$$

where ϕ_j is the phase factor for the jth atom represented as

$$\phi_j = 2\pi\Delta\vec{K}\vec{r}_j \qquad \text{(Equation 40)}$$

If $$r_j = u_j\vec{a} + v_j\vec{b} + w_j\vec{c} \qquad \text{(Equation 41)}$$

then the total amplitude scattered by the unit cell is given as:

$$F_{hkl} = \sum_j f_j e^{2\pi i\left(hu_j + kv_j + lw_j\right)} \qquad \text{(Equation 42)}$$

which is the structure factor given by equation 38.

SAED technique was used to obtain diffraction patterns from the oxide formed by atomic and molecular oxygen. SAED patterns give structural information about the crystal structure from the particular location of the specimen. These patterns can be used to conclude about the crystallinity and ordering of the analyzed material.

6.4.1 Selected Area Electron Diffraction (SAED) – Results

Plan view high-resolution transmission electron micrographs of Si(100) oxidized by molecular oxygen and Si(100) and Si(111) oxidized by atomic are shown in Figure 25-a, 26-a and 27-a respectively, and corresponding selected area electron diffraction patterns are given as inserts in the upper left corner of the micrographs.

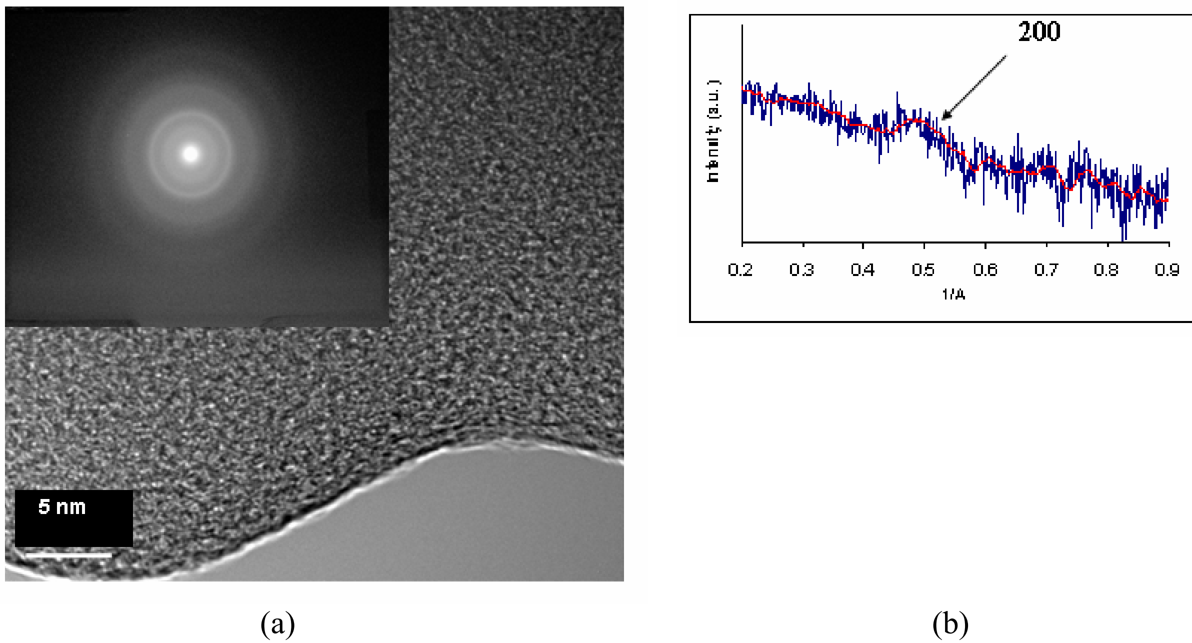

Figure 25. (a)Plan-view HRTEM micrographs and corresponding SAED pattern of the silicon oxide layer formed on Si(100) oxidized by molecular oxygen (b) Intensity profile taken across the diffraction pattern.

Using Gatan Digital Micrograph, profiling of intensities was done across the diffraction patterns and they are shown in Figures 25-b, 26-b and 27-b. This technique enables one to better see the appearance of certain "peaks" representing diffraction intensities from the particular sets of planes.

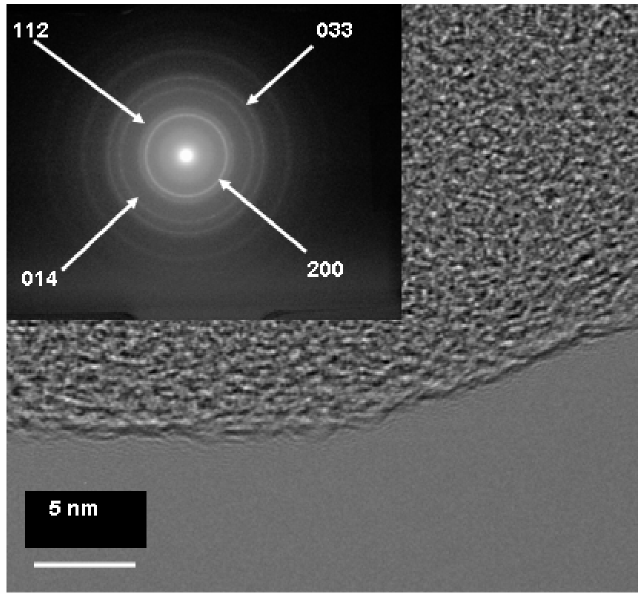

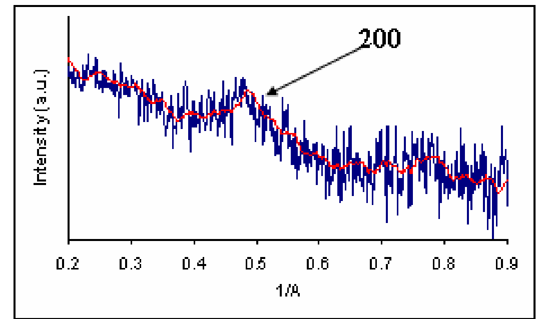

(a) (b)

Figure 26. (a) Plan-view HRTEM micrographs of the silicon oxide layer formed on Si(100) oxidized by atomic oxygen (b) Intensity profile taken across the diffraction pattern.

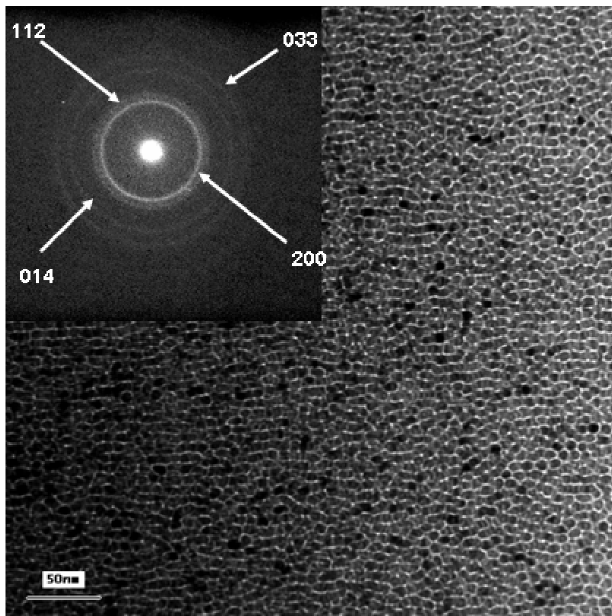

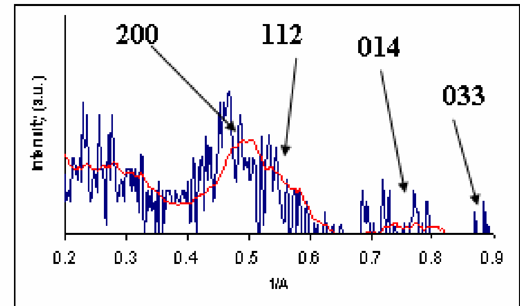

(a) (b)

Figure 27. (a) Plan-view HRTEM micrographs of the silicon oxide layer formed on Si(111) oxidized by atomic oxygen (b) Intensity profile taken across the diffraction pattern.

Selected area diffraction pattern of the Si(100) oxidized by molecular oxygen showed diffused haloes rings, characteristic for non-ordered, amorphous materials. In contrast, much sharper and resolvable diffraction rings are present in the diffraction pattern of both Si(100) and Si(111) oxidized by reactive atomic oxygen species.

Due to their sharpness, certain diffraction rings can be identified and indexed as diffractions from (200), (112), (014) and (033) sets of planes and d-spacing of these planes were determined. These experimental d-spacings for the oxide created by reactive atomic oxygen species (d_{200}=2.070A^o, d_{112}=1.783A^o, d_{014}=1.282A^o and d_{033}=1.085A^o) correspond to that of alpha-quartz (d_{200}=2.1275A^o, d_{112}=1.8178A^o, d_{014}=1.2879A^o and d_{033}=1.1144A^o) [67].

6.5 ELECTRON ENERGY LOSS SPECTROSCOPY (EELS)

The Electron Energy Loss Spectroscopy technique measures energy loss of the beam electrons that interact with the specimen. It measures energy transfer between the electrons in the incident beam and atomic electrons. Information regarding the local environment of the atomic electrons and nearest neighbor atoms can be obtained. Electrons interacted and passed through the sample travel through the microscope lenses eventually reaching the spectrometer. EELS spectrometer is mounted after the projector lens. The magnetic prism is the main component of the spectrometer and it is used to resolve energies of the electrons. Gatan Imaging Filter (GIF) possesses both imaging and spectral possibilities. When electrons enter the magnetic prism spectrometer, they are

deflected by the magnetic field. The level of deflection is determined by the energy loss that electrons experienced and the greater the energy loss of the electron, the further is the deflection. The electron beam first goes into the scintillator and the photons are generated inside it and directed to 1024 photodiode arrays. The resulting spectrum represents electron intensity (counts) versus energy loss and it is read out as pulses and the height of the pulse.

Dark current background arises from thermal leakage current which varies form each CCD camera. It contributes to the acquired image and, generally, should be removed. This is done by subtraction of a 'dark reference' image. This image should be acquired under the same conditions as the real image, only with no beam on the detector. Dark current is reduced by detector cooling.

Sample drift may be present as the result of the instability of either the microscope or specimen, or both. Minimization of the sample drift is done before the data acquisition since the drift during the sample acquisition cannot be removed and the image will be blurred. This is of importance if a number of core-loss images are represented as spatially aligned.

There are two basic designs of the EELS spectrometers, serial and parallel. The serial method is rather inefficient since it requires a long time but it is mostly free of artifacts since all energy loss channels are recorded by the same detector. The parallel method is characterized by much shorter spectra acquisition time and it is the preferable method in EELS analyses.

The spectrometer can operate in the image or diffraction mode. In the diffraction mode, a diffraction pattern is displayed on the screen and the spectrometer is image

coupled. A small image of the specimen illuminated is contained in the cross-over of the projector lens of the spectrometer.

In the imaging mode, the image is displayed on the screen and the spectrometer is diffraction coupled. A small diffraction pattern of the sample is contained in the projector lens cross-over.

In the case when dedicated Scanning Transmission Microscope (STEM) is used in EELS analyses, the spectrometer is image coupled. The sample is placed in the field of the probe-forming objective lens and between the sample and spectrometer; there are no lenses for imaging.

Acquiring the EELS spectrum includes choosing a collection angle and checking of the zero-loss peak width since it gives a direct estimate of the spectrometer energy dispersion [68].

6.5.1 Scanning Transmission Electron Microscopy (STEM) Spectrum Imaging (SI)

Changes in composition of the materials take place at the nanometer level; therefore it is important to use a technique that is able to determine accurately the chemical distribution on such a small scale. Spatial resolution of EELS Spectrum Imaging is approximately 1nm, giving a variety of possibilities to study multilayer properties of the miniature semi-conductor devices.

Acquiring a spectrum image requires using Scanning Transmission Electron Microscope (STEM) and parallel recording detector. A nanoscale probe is produced at particular point coordinates, (x,y) on the sample. The probe is scanned across predefined

investigated region and the EELS spectrum is acquired at each of the probe positions. EELS spectrum is acquired and recorded at each pixel.

Actually, electron intensity within a 3-D volume of (x,y and E) is recorded. For example, if the size of the image is 20x20 pixels, it will contain 400 acquired spectra [68, 69].

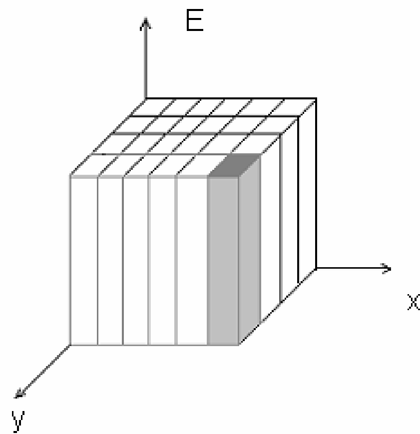

Figure 28. STEM analyses with Spectrum Imaging (SI).

It is also possible to create a background subtracted spectrum image and to follow a particular edge progression over the range of probe position.

6.5.2 Electron Energy Loss Spectrum

In the Electron Energy Loss Spectroscopy, electrons which experienced inelastic interaction with the sample are analyzed. Not all of the beam electrons have interacted with the specimen inelastically-EELS spectrum contains information about both elastically and inelastically scattered electrons.

All features except zero-loss peak result from the inelastic scattering of the incident electron beam. Elastic scattering origin is Coulomb attraction of the beam electrons by atomic nucleus. The term elastic means that there is no change in energy, but there is the change in the deflection angle.

Inelastic scattering refers to the beam electrons that are scattered by the inner or outer shell atomic electrons, caused by Coulomb repulsion. We are primarily interested in inelastically scattered electrons. Inelastic interaction carries information about the nature of the atoms, their electronic structure and bonding effects with the surrounding atoms. Different energies are involved in inner and outer-shell scattering; therefore, these losses occupy different parts of the EELS spectrum [61, 68].

Regions of the EELS spectrum are:

Zero - loss peak is the most intense feature in the spectrum and contains elastic forward-scattered and electrons that experienced very small energy losses. Therefore, these electrons have approximately the same energy as the electron beam.

Generally, zero-loss peak is not a useful feature in the spectrum; it is a potential danger to the scintillator due its huge intensity.

Low-Loss spectrum appears adjacent to the zero-loss peak and is much less intense. It contains electrons that interacted with the weakly bound outer shell electrons of the sample resulting in low energy losses (up to ~50eV).

Surface and bulk mode plasmon oscillations are produced dominating low-loss spectrum.

High-Loss part of the spectrum contains electrons that interacted inelastically with tightly bound inner shell (core) electrons and it appears above 50 eV.

The basic ionization edge shapes found in this part of the spectrum are determined by atomic physics, independent of the bonding and environment of the atom and can be expressed using the single atom model. The energy needed for the atom ionization process is transferred from the electron beam to the particular shell electron. The amount of the energy lost by the electron beam is the same energy which is required for the atom ionization and is called ionization energy.

Therefore, the ionization process is a characteristic of an atom and particular shell ionization. The K shell is closest to the attractive positive nucleus and requires the highest energy to be ionized. Therefore, a feature that corresponds to the transition of electron from the K shell will appear at the highest energies in the EELS spectrum. Ionization of L, M, N and O shells requires much less energy since these shell electrons are farther away from the nucleus.

Ionization cross-section and the basic core-loss profile are determined by the generalized oscillator strength (GOS) which is defined as the probability of a transition of a bound electron from its ground state to a particular state in continuum [68].

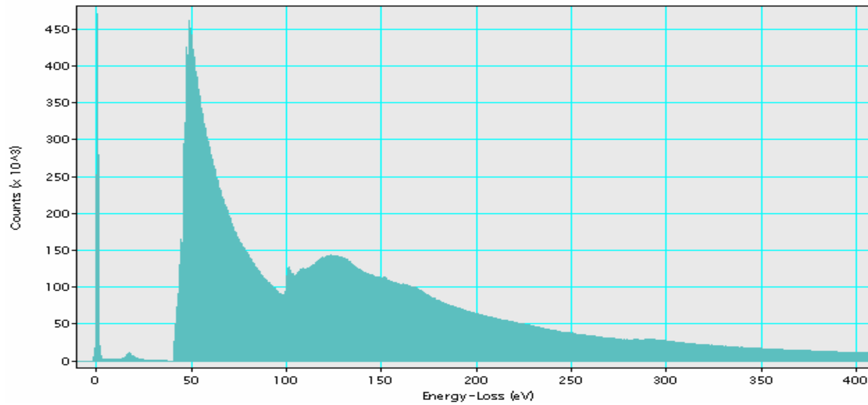

Figure 29. Characteristic EELS spectrum of SiO_2 as-acquired containing the most intense zero-loss peak, low-loss and high-loss region characterized with core-loss edges.

For this particular spectrum, there is a sharp rise appearing at the ionization threshold and the energy loss corresponds to the binding energy of the atomic shell. Presence of certain elements can be determined from the appearance of the edges in the spectrum. Background to ionization edges ratio will increase if the sample is not thin enough and these edges will be hard to resolve. Generally, specimens thinner than 50nm should be used in EELS experiments. Effects of plural and multiple scattering can distort the shape of the EELS spectrum; therefore, great care has to be taken in the specimen preparation step. Plural (more than 1 scattering event) and multiple scattering (more than 20 scattering events) arise when specimen thickness is more than the mean free path of the inelastic scattering phenomena. The term mean free path refers to the average distance between scattering events.

If intensity of the plasmon peak is less than 10% of the intensity of zero-loss peak that means that the specimen is adequate for EELS analyses. Superimposed on the monotonically decreasing background are ionization edges characterized by their fine structure. By the comparison of the experimental edges fine structure with the EELS

Atlas database or edges library, it is possible to determine the particular element [70]. This fine structure changes for the element when it undergoes phase transition or changes valence state. Therefore, spectra must be processed and near edge fine structure revealed.

6.5.3 Electron Loss Near Edge fine Structure (ELNES)

ELNES corresponds to fine peaks around core-loss edges (<50eV). It is very sensitive to the chemical and structural surrounding around the particular excited atom. Chemical shift of the ionization threshold usually accompanies the ELNES and this shift originates from the changes in chemical bonding. For the particular case of the SiO_2 compound, a molecular orbital diagram (shown in Figure 30) is very useful in explaining the origin of the Si edge shift from 99.5eV in bulk silicon to 103.5eV in silica. The chemical shift or the displacement of the edge onset occurs when the atom environment is changed since there is a change in the inner shell binding energies [71, 72, 73].

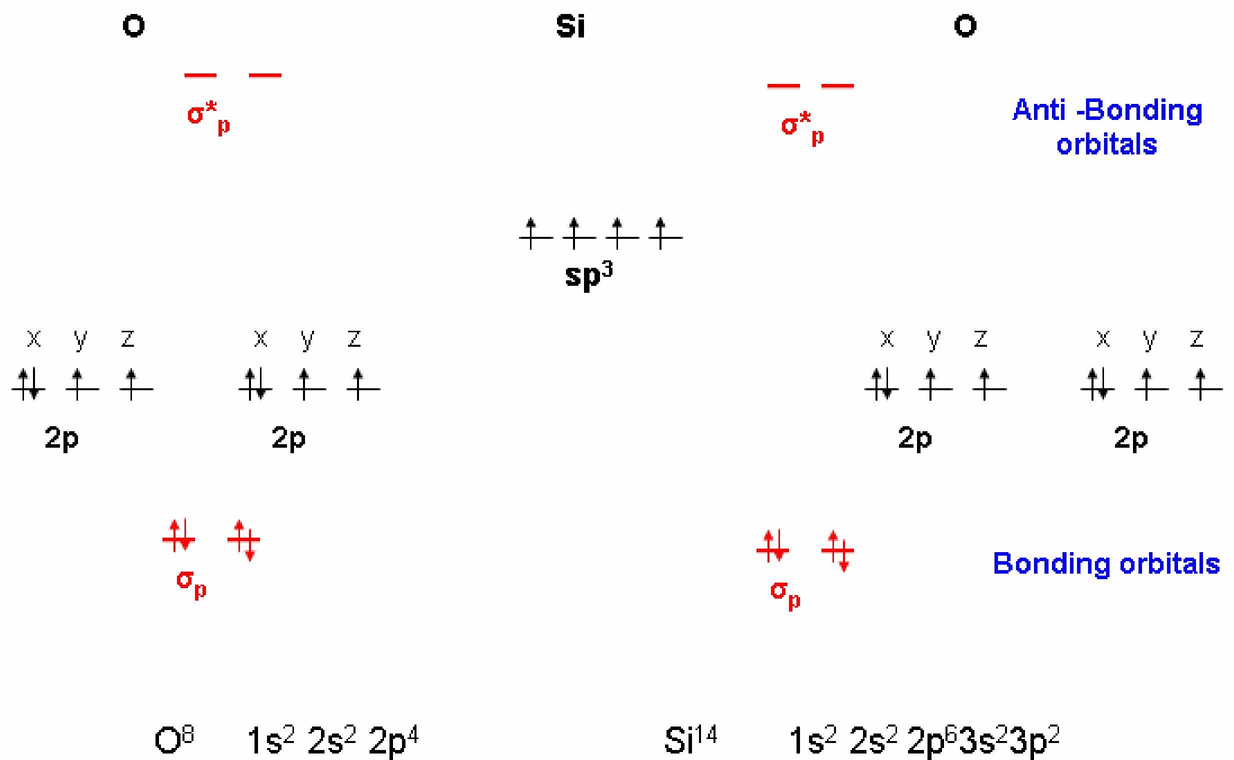

Figure 30. Molecular orbital (MO) diagram for SiO_2.

In the pure silicon, four sp^3 orbitals are formed by hybridization between Si s and p orbitals. Pure silicon structure can be visualized as a central Si atom which is sp^3 hybridized bonded with other 4 Si atoms consequently forming two kinds of molecular orbitals. Antibonding molecular orbitals have higher energy levels than atomic orbitals and therefore do not contribute to the bonding. On the other hand, bonding molecular orbitals have an energy level that is decreased when compared to the atomic orbitals, and they are filled with electrons which contribute to the bonding. Since all four Si ligand

atoms surrounding the central Si atom are identical, there will be a small decrease in the energy level of formed bonding molecular orbitals.

In the case of SiO_2, the Si central atom is bonded to four O atoms which represent electronegative ligands having lower energy of their atomic orbitals when compared to the Si atom. Overlap of the hybridized sp^3 orbitals of Si with 2p orbitals of O produces σ bonds [74]. Therefore, formed bonding SiO_2 molecular orbitals will have decreased energy when compared to the bonding orbitals of pure silicon.

The $SiL_{2,3}$ edge represents transition of an electron from the 2p core state to the unoccupied states. These unoccupied states are 3d and 4s, and transfer of electron in these states is determined by the "dipole selection" rule. The p state has a principal quantum number n=2, and the angular quantum momentum number l=1. The dipole selection rule requires the angular momentum quantum number change, Δl, between the initial and final state to be ±1. According to that, l must be equal to 0 or 2 in the unoccupied state, which suggest that s (l=0) or d (l=2) orbital will be the final electron states.

Formation of hybridized sp^3 orbitals produces "dipole allowed" $p \to p$ transitions since 2p core electrons can be transferred into the s-like part of the sp^3 hybrid [54, 68].

It was found that SiL near-edge structure (ELNES) depends on atom surrounding and chemical environment of the silicon atom. ELNES change was observed, reflecting change in the ionization threshold energy and edge profile. It was concluded that these changes result from the bond-induced changes in the valence shell electronic structure [72, 75, 76, 77].

Above mentioned interpreting the near edge structure is known as the 'fingerprint approach' where common features from the elements in similar environments are

identified. The "fingerprint method" is particularly useful to determine the atom surroundings and its valence.

It was found that electronegativity and type of bonding directly influence the core loss edge shape, therefore giving rise to the unique features that are recognizable as a fingerprint of the material [68, 72, 78, 79, 80, 81]. For example, ELNES of $SiL_{2,3}$ and SiK edge of quartz is quite different from ELNES of stishovite, which is characterized by 6-coordinated Si [82] .

6.5.4 EELS Spectra Processing

In order to extract either qualitative or quantitative data, acquired EELS spectrum must be processed. Signal to background ratio becomes very small if the specimen is too thick and spectra obtained from such specimens must be first deconvoluted. Generally, deconvolution should be avoided since one can easily introduce many artifacts and errors and finally get the spectrum that is even worse representation of the actual data than the originally collected, unprocessed spectrum.

1. The very first step is input of experimental conditions, such as beam energy [keV], convergence and collection semi-angles [mrad].
2. Calibration of the energy scale is usually done using known edge position
3. Large, monotonically decreasing background signal is present and must be removed to allow ELNES determination and quantitative analyses of the core-loss signal I_k.

$$I_k = I_t - I_b \quad \text{(Equation 43)}$$

where I_t is the total integrated intensity over the core-loss integration range and I_b is background contribution to the total intensity.

This background intensity has to be removed since it originates from valence-electron excitations, plural inelastic scattering and the tails of preceding core-loss edges and it is often comparable or even greater than the core-loss signal of interest. In order to minimize the effect of plural scattering, very thin specimens should be used for EELS studies, and their thickness is typically supposed to be significantly less than the inelastic mean free path, λ, of the material of interest [68]. There are several models available in the EELS package for background extrapolation and one should choose the model that provides the most accurate fit. A simple energy-loss function, I(E), is fitted to a background region immediately before the edge of interest. Generally, 50eV offset should be used not to lose information from the pre-edge region.

Polynomial, log-polynomial or power-law models can be used for this operation [65]. An inverse power-law is the most commonly applied and produces the most satisfactory results in a broad range of analyses.

Inverse power law function has the form:

$$I(E) = AE^{-r} \quad \text{(Equation 44)}$$

where **I(E)** - the expected or true background, **A** –the scaling constant

r - pre-edge slope exponent

Since only two fit parameters are present, inverse power-law gives accurate fit in most cases. While the value of the scaling coefficient, A, can vary widely depending on the intensity of the background –fitting region, the value of the pre-edge slope exponent is usually between 2 and 6 [68].

Background extrapolation errors

As a consequence of deviations in the recorded background intensity from the power-law background model, systematic errors can occur.

The derivation of equations that evaluate the variance of I_b for the power-law background is given in reference 56. Signal-to-noise (SNR) ratio for the core-loss signal I_k is given as:

$$SNR = \frac{I_k}{\sqrt{\text{var}(I_k)}} = \frac{I_k}{\sqrt{I_k + hI_b}} \qquad \text{(Equation 45)}$$

$$h = 1 + \frac{\text{var}(I_b)}{I_b} \qquad \text{(Equation 46)}$$

h accounts for the statistical uncertainties associated with the background removal and it is dimensionless and value of $\text{var}(I_b)$ is estimated from the pre-edge fitting region.

h represents the increase in the background dependent part of $\text{var}(I_k)$ which is the consequence of the background fitting and errors in extrapolation. The value of h is actually the measure of the background extrapolation step quality [68].

4. Partial ionization cross-section represents the probability of a scattering event to occur in the interaction of the beam electron and an atom electron.

Energy-differential cross-section, dσ /dE is calculated for a particular edge and integrated over the chosen signal integration energy-window in order to obtain partial cross-section. Using this procedure, raw edge counts are converted into a number proportional to the actual concentration of the associated atomic species [81].

Depending on the shell type, different models should be used for cross-section calculation.

Egerton's SIGMAK and SIGMAL computer's programs are used only for K and L shells modeling and they are embedded in GATAN EELS software [69].

SIGMAL and SIGMAK use the calculation of the generalized oscillator strength (GOS) and ionization cross-section according to hydrogenic model. This model is the simplest one since it assumes isolated hydrogen atom, neglecting outer shell electrons, so it is best for K shell electrons. It gives a very good fit to the experimentally observed edge, but it also neglects near and post edge fine structure since it does not take into account any other electrons present.

Beside hydrogenic model, Hartree-Slater model can also be used. This model assumes that the elements are in atomic form and can be treated using single-electron inner-shell wave function undergoing transition to a final state. This model is much more complicated than the hydrogenic model and better for L and M edges and generally can be applied for any edge that is beyond the range of SIGMAL.

The edge intensity integration window should be such that E_{finish} ~1.5 E_{start}, since fit parameters A and r in the power law function (Equation 44) are valid and constants over ~100eV. There is a trade-off between using the large integration window and improving statistics and validity of A and r over certain energy range.

5. Quantification

Elemental composition information for present edges can be extracted for known GOS and ionization cross-sections. Parameters such as signal window and background window are easy to adjust and the change is displayed interactively on the spectrum. We were most interested in the relative quantification since it outputs each element

concentration as a ratio to the element of the highest concentration and also as a percentage of the total species analyzed and quantified. Quantification is based on the relationship:

$I_K = N\, I\, \sigma_K$ (Equation 47)

I_K – edge intensity or sum of all counts in the particular background subtracted edge

I – total integrated intensity or total integrated number of counts

N – area concentration [atoms/nm^2] of the atoms giving rise to the ionization edge K

σ_K – cross-section for ionization of an electron for the particular shell K [68, 69].

6.5.5 EELS Acquisition Conditions and Spectra Processing-Experimental

1. Beam energy was 200 keV and 100 keV for JEOL 2010F and VG-HB501 respectively. Convergence and collection angles used were 12 mrad and 30 mrad for JEOL 2010F and 8 mrad and 20 mrad for VG-HB501 microscope.
2. Calibration of the energy scale was done using known carbon K edge position at 284 eV. The major source of the carbon is epoxy used for the preparation of cross –sectional TEM samples. Generally, C edge is undesired feature in the spectrum, but on the other hand, it is very useful to calibrate the energy scale.
3. Background removal was done using power-law. Power law profile is fitted in the pre-edge region and extrapolated to the post edge region and subtracted. Fitting was done in a chosen background window (<50eV in width) in the pre-edge region. Since Si L edge ionization energy is low (~99 eV), background fitting window was very small while it was larger for O K edge which appears

on 532eV. Generally, the smaller the energy window, the better the power law fit. Background is subtracted when both sharp rise in the edge intensity and the best fit in the pre-edge region were achieved during the fitting procedure.

Figure 31 shows EELS spectrum as -acquired from Si(100) and background fitting using the power law revealing SiL2,3 edge fine structure. C K edge is also noticeable at ~284eV.

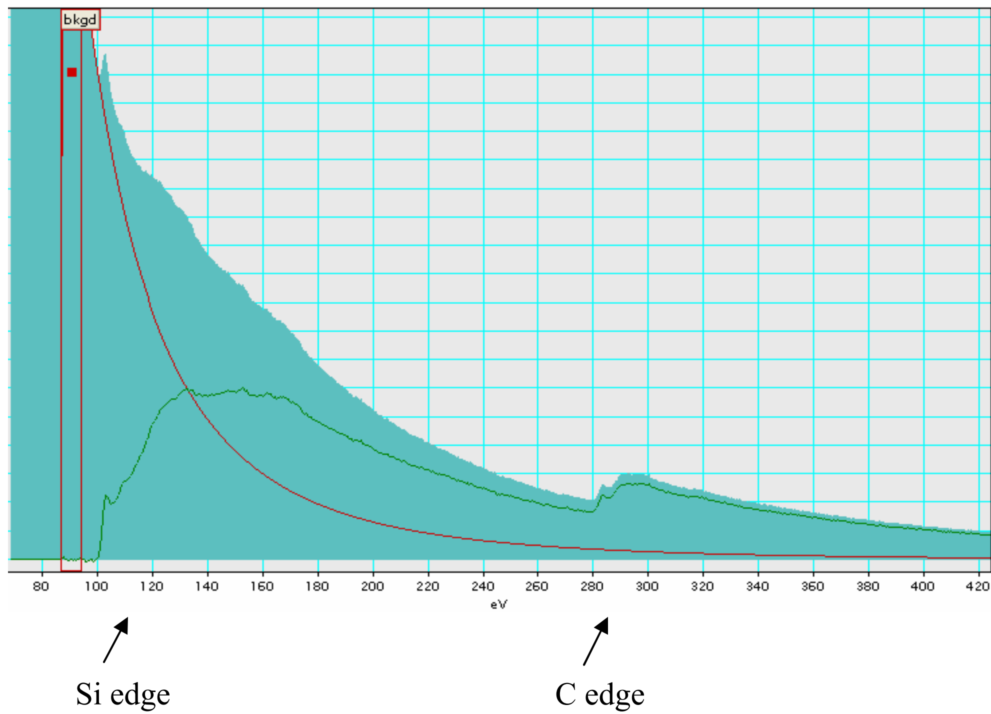

Figure 31. As - recorded EELS spectrum and background fitting to $SiL_{2,3}$ edge.

4. Partial ionization cross-section was calculated using Hartree-Slater model both for SiL and O K edges since it seemed to be very good approximation of the experimentally observed edges [69].

EELS technique enables determination of valence states of the analyzed element. Chemical shift of the characteristic ionization edge reflects the change in the oxidation state of the particular element. We used this method to get information about the oxidation states of Si within the bulk silicon-oxide and at the Si/oxide interface. This technique also allows determination of a stoichiometry of the formed oxide.

Fingerprint method was used to conclude about the oxide crystallinity.

6.5.6 Electron Energy Loss Spectroscopy (EELS) – Results

6.5.6.1 Spectrum Imaging –Results

Spectrum Imaging data obtained from Si(100) oxidized by atomic and molecular oxygen are shown in the Figures 32 and 33, respectively. Spectra were background subtracted using power law in order to extract only characteristic, core-loss ionization edges.

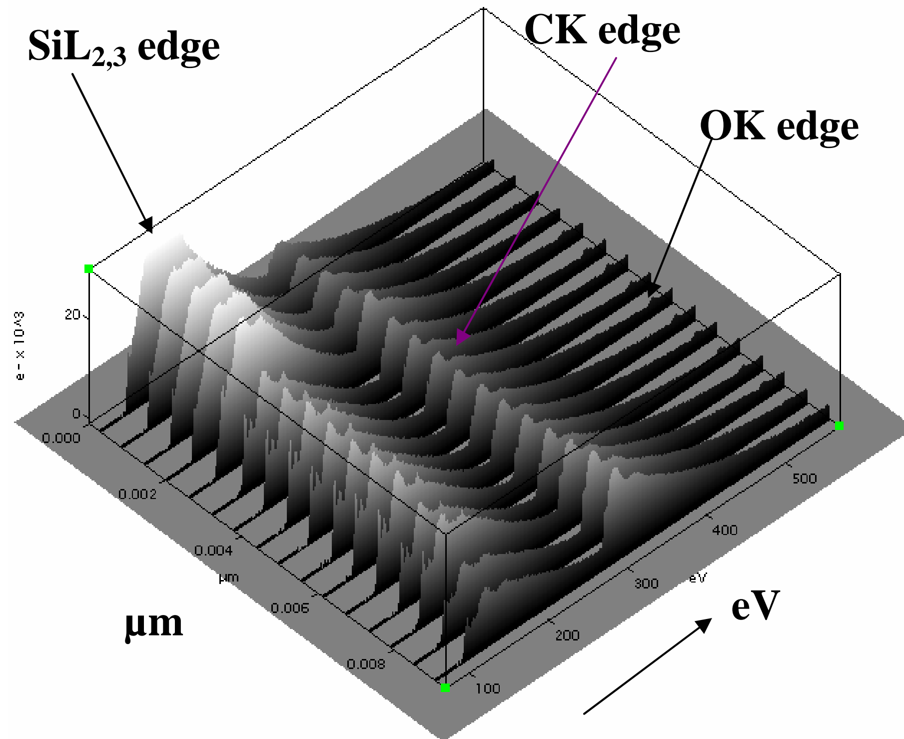

Figure 32. Overall background subtracted EELS spectra obtained from Si(100) oxidized by atomic oxygen.

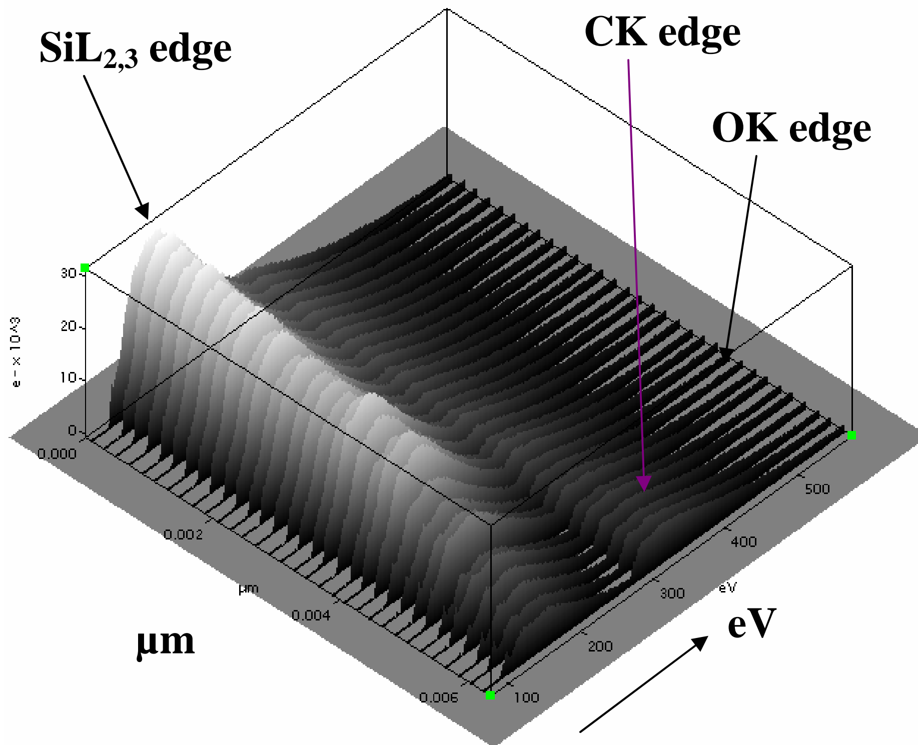

Figure 33. Overall background subtracted EELS spectra obtained from Si(100) oxidized by molecular oxygen.

It can be seen that more pronounced core-loss edges are present for the Si(100) oxidized by atomic oxygen species. Silicon $L_{2,3}$ ($SiL_{2,3}$) , carbon K (CK) and oxygen K (OK) core-loss edges can be seen at their characteristic ionization energies of ~99.5-103.5eV, 284eV and 532eV, respectively. Signal of the carbon edge at 284eV is very strong for both atomic and molecular oxygen oxidized sample and the main reason of its appearance is epoxy used in cross-sectional TEM sample preparation. There is a clear difference in the shape of the $SiL_{2,3}$ edges for Si(100) oxidized by atomic and molecular oxygen as well as in the oxygen edge intensity. $SiL_{2,3}$ and OK edges are more pronounced for the Si oxidized by atomic oxygen (Figure 32) when compared to the Si oxidized by molecular oxygen (Figure 33).

Characteristic $SiL_{2,3}$ and OK background subtracted edges obtained from Si(100) single crystal oxidized by atomic oxygen by Spectrum Imaging technique are shown in Figures 34 and 35, respectively. The length of the scan was 95 A^{o}.

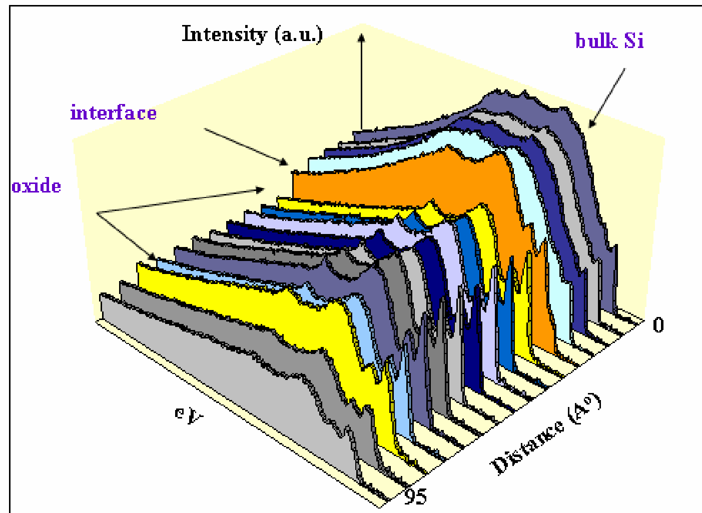

Figure 34. Characteristic core-loss ionization $SiL_{2,3}$ edge for Si(100) oxidized by atomic oxygen.

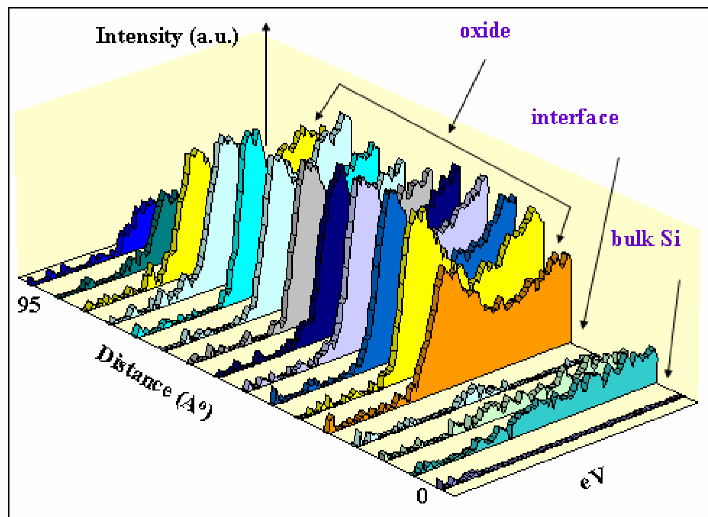

Figure 35. Characteristic core-loss ionization OK edge for Si(100) oxidized by atomic oxygen.

Characteristic $SiL_{2,3}$ and OK background subtracted edges obtained from Si(100) single crystal oxidized by molecular oxygen by the Spectrum Imaging technique are shown in Figures 36 and 37, respectively. The length of the scan was 64 A^o.

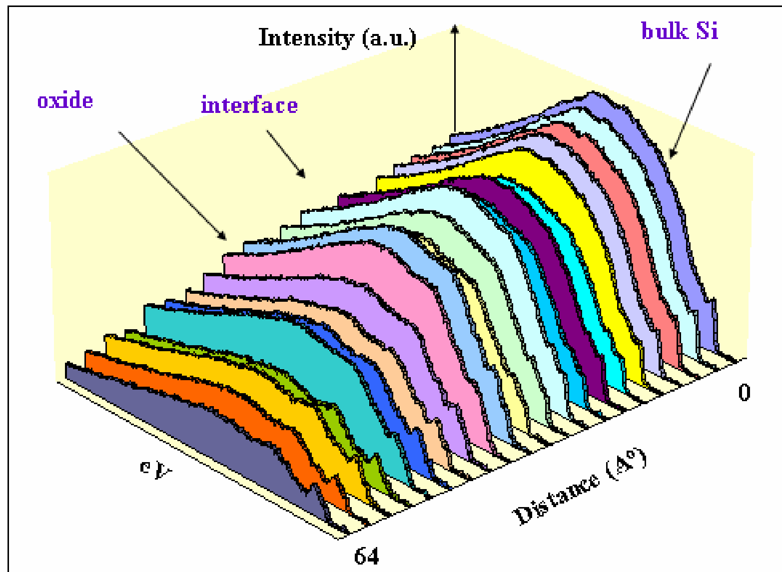

Figure 36. Characteristic core-loss ionization $SiL_{2,3}$ edge for Si(100) oxidized by molecular oxygen.

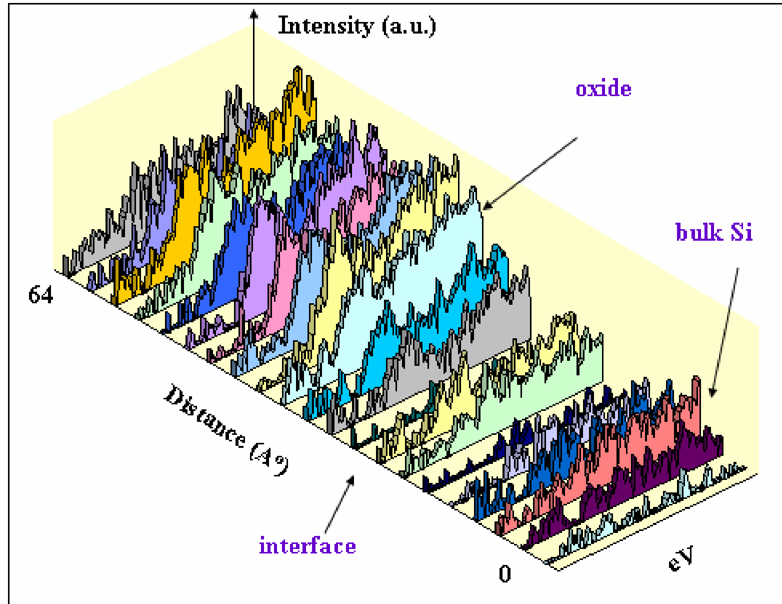

Figure 37. Characteristic core-loss ionization OK edge for Si(100) oxidized by molecular oxygen.

The evolution of the $SiL_{2,3}$ edge from the scan start in the bulk silicon (Si^o), across the Si/SiO_2 interface to the scan end in silica bulk oxide (Si^{4+}) shows that only peaks corresponding to Si^o and Si^{4+} valence states are present (Figure 34). Both $SiL_{2,3}$ and OK ionization edges reveal very abrupt Si/SiO_2 interface for the Si(100) sample oxidized by atomic oxygen (Figures 34 and 35). From this spectrum image it is evident that going from the Si bulk, once the Si/SiO_2 interface is reached, there is no change in the ELNES of $SiL_{2,3}$ core loss edge. $SiL_{2,3}$ edge onset shift from Si^o (99.5eV) to Si^{4+} (103.5eV) valence state is very abrupt, without showing any additional peaks which appear when the suboxides are present (Figures 34 and 35). Probe size used was 1.2nm.

Results from Spectrum Images of Si(100) oxidized by molecular oxygen reveal that there is no sharp interface and that transition from Si^o to Si^{4+} state is very gradual, with a number of intermediate states (Figures 36 and 37).

These results are in very good agreement with our HRTEM results where intensity profiling showed that almost no interfacial layer is present for Si(100) oxidized by atomic oxygen (Figure 18) and that ~1nm thick interface layer is present for Si(100) oxidized by molecular oxygen (Figure 19).

6.5.6.2 $SiL_{2,3}$ Energy Loss Near Edge Structure (ELNES) -Results

Figures 38-a, 39-a and 40-a show annular dark field images obtained from Si(100) oxidized by molecular and atomic oxygen and Si(111) oxidized by atomic oxygen, respectively. Background subtracted $SiL_{2,3}$ edges are recorded in the bulk Si, Si/SiO_2 interface and bulk oxide.

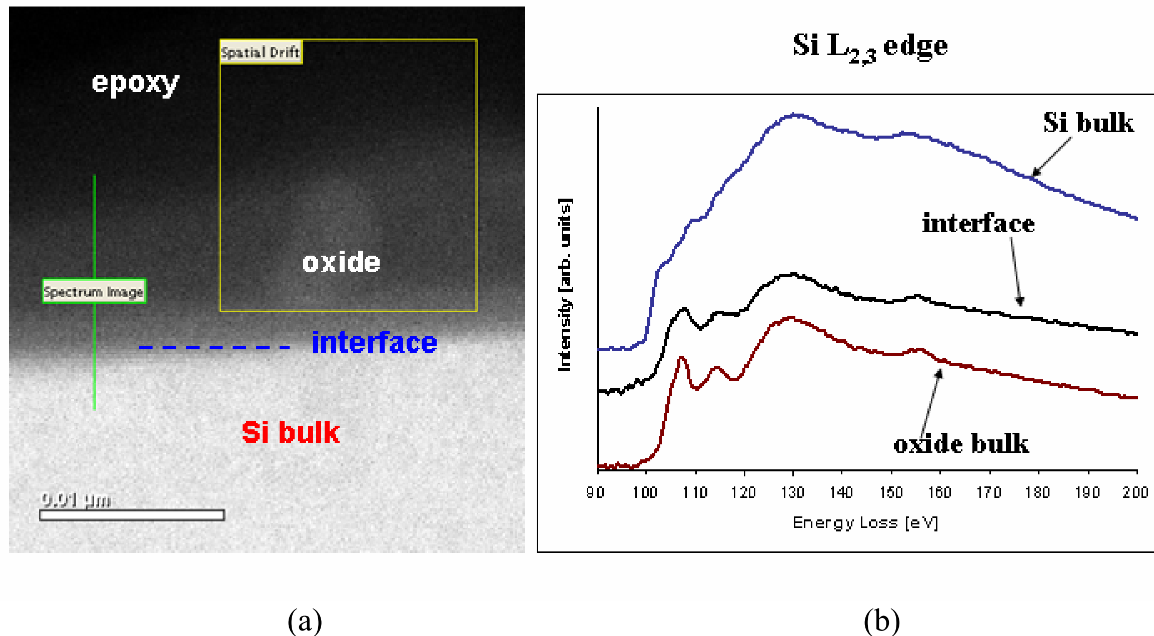

(a) (b)

Figure 38. Si(100) oxidized by molecular oxygen (a) Annular dark field image (b) $SiL_{2,3}$ background stripped edge recorded in Si bulk, Si/SiO_2 interface and oxide bulk.

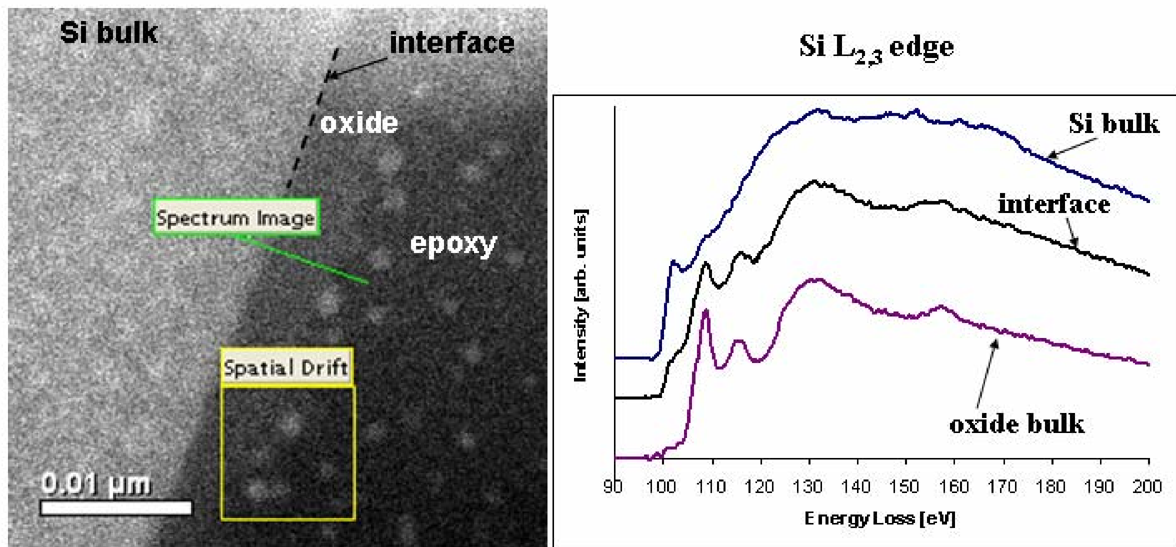

(a) (b)

Figure 39. Si(100) oxidized by atomic oxygen (a) Annular dark field image (b) $SiL_{2,3}$ background stripped edge recorded in Si bulk, Si/SiO_2 interface and oxide bulk.

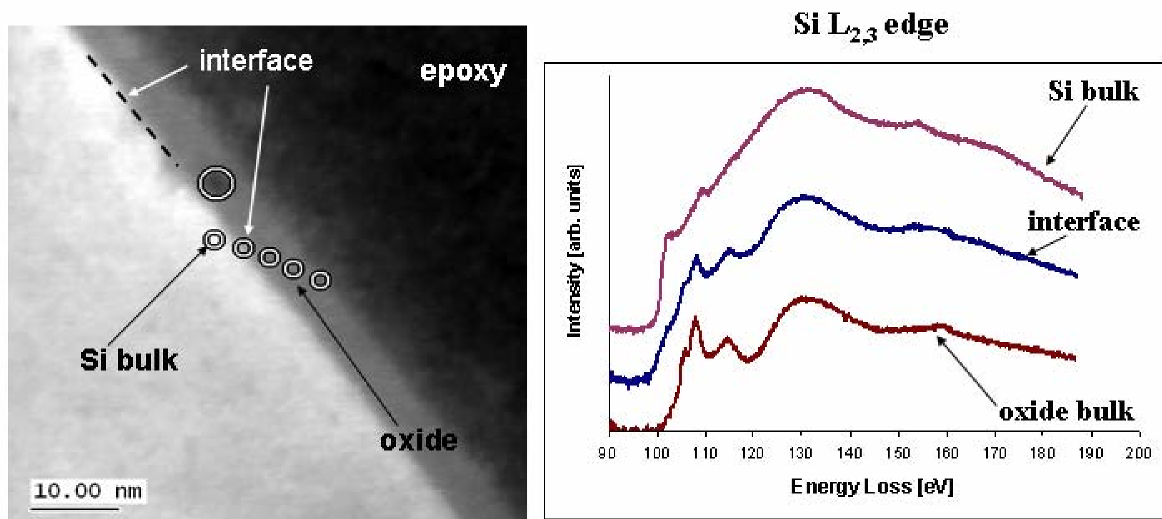

(a) (b)

Figure 40. Si(111) oxidized by atomic oxygen (a) Annular dark field image (b) $SiL_{2,3}$ background stripped edge recorded in Si bulk, Si/SiO_2 interface and oxide bulk.

Atomic oxygen oxidized samples show much sharper peaks (Figures 39-b and 40-b) when compared to the molecular oxygen oxidized one (Figure 38-b). $SiL_{2,3}$ edge in

bulk Si exhibits its onset at ~99.5eV while this edge onset is shifted to ~103.5eV in the bulk oxide as the result of band gap expansion from semiconductor to insulator. Transition of the electrons from the 2s to p orbitals gives rise to the L_1 edge and the ejecting of the electron from the 2p orbitals causes the L_2 or L_3 edge [74].

In silicon and silicon oxide, the L_2 and L_3 edges exist as a one edge, in fact, they are not resolvable when existing on the lower ionization energies causing appearance of only one, $L_{2,3}$ edge [68]. The $SiL_{2,3}$ edge in the bulk oxide is characterized by the peaks at 108eV, 115eV and 130eV. Due to the better energy resolution (~1nm) of the VG-HB501 microscope used for the collection of data represented in Figure 40, the peak at 106eV can be seen. This observed peak is under the resolution limit of the JEOL 2010F microscope (~1.5nm), that is used for acquiring the data represented in Figures 38 and 39. Its existence is implied by the existence of a shoulder just before the peak at 108eV. At ~160eV, a higher energy loss L_1 edge can be seen.

Figure 41 shows a comparison of Electron Loss Near edge Fine Structures (ELNES) of $SiL_{2,3}$ edges obtained from Si(100) oxidized by atomic and molecular oxygen and Si(111) oxidized by AO with the results of Garvie et al.[83].

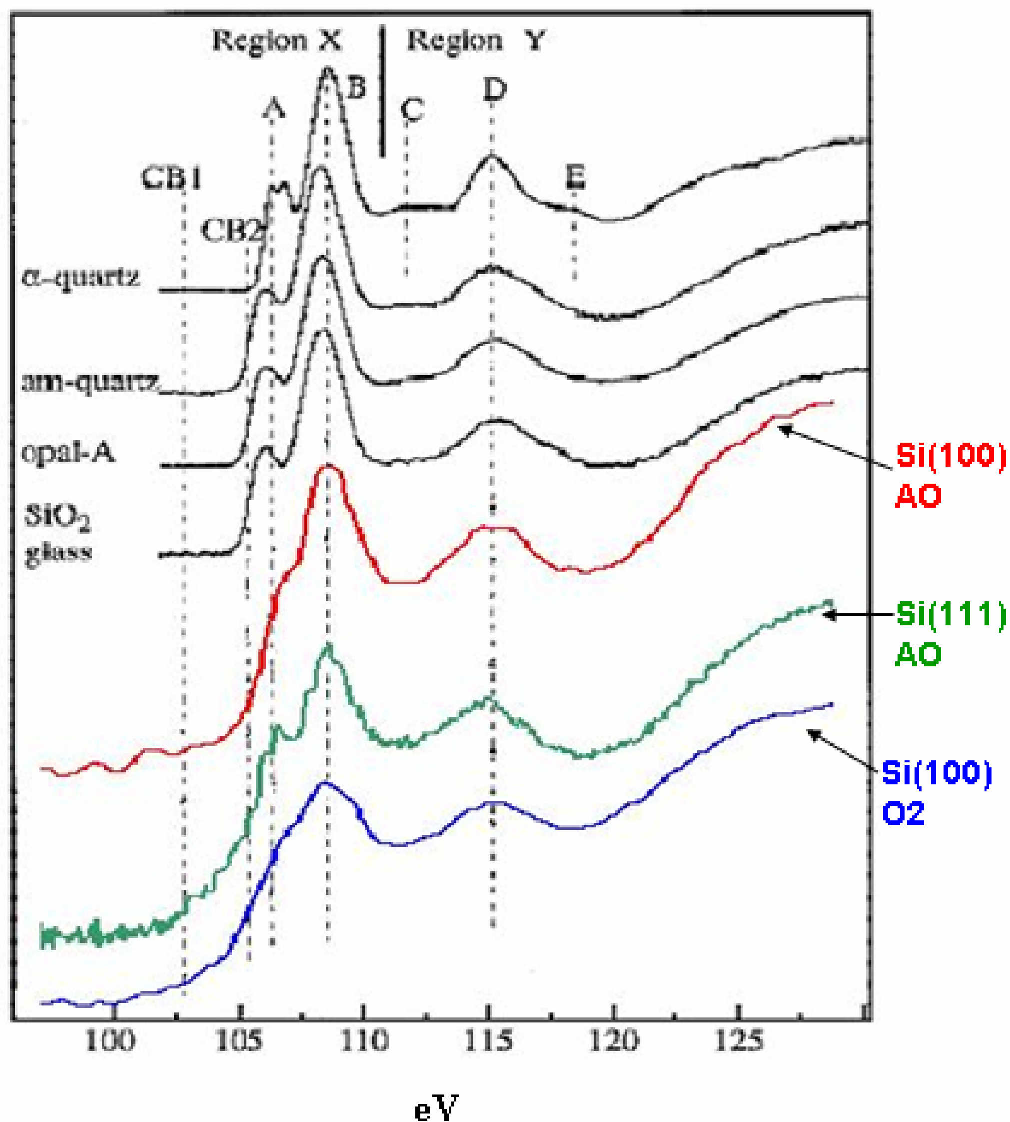

Figure 41. ELNES comparison of $SiL_{2,3}$ edges of Si(100) oxidized by atomic and molecular and Si(111) oxidized by atomic oxygen with results of Garvie et al.

$SiL_{2,3}$ core-loss edges from Si(100) and Si(111) oxidized by two different oxidizing species are superimposed on the $SiL_{2,3}$ edge ELNES for different forms of silica, obtained by Garvie et al. Comparison is made using the fingerprint method and comparing our results with ELNES features in $SiL_{2,3}$ edge of alpha-quartz, amorphous quartz (electron beam damaged quartz), opal A (SiO_2 x nH_2O) and SiO_2 glass. The characteristic ELNES peaks/features are marked as A, B, C, D and E.

Garvie et al. found that it is possible to conclude whether the structure is crystalline or amorphous from the closer examination of peaks width and position [83].

Higher energy edge onset, sharper peaks and peak in position E are characteristic features that are present in the crystalline form of silica, alpha-quartz. Amorphous silica is found to have lower energy of the edge onset, broader peak maxima and lower energy ELNES maxima.

Generally, $SiL_{2,3}$ core-loss edges in silica exhibit their onset at 103.5eV, characteristic larger peaks at 108eV, 115eV followed by delayed maxima at 130eV. As mentioned before, due to the better resolution of the VG-HB501 microscope, peak at 106eV can be resolved for the Si(111) oxidized by atomic oxygen.

It can be seen that the core-loss edge onset of the Si (100) oxidized by atomic oxygen is slightly shifted towards higher energies when compared to the edge onset for Si (100) oxidized by molecular oxygen. $SiL_{2,3}$ edge recorded on silicon oxide created by atomic oxygen shows higher edge onset energy and sharper peak B when compared to the $SiL_{2,3}$ edge obtained from silica layer formed by molecular oxygen oxidation. Also, small peak E around 118 is noticeable for Si(100) oxidized by atomic oxygen whereas such a peak is completely unresolved for amorphous silica formed by molecular oxygen oxidation.

It can be concluded that oxidation of Si by hyperthermal atomic oxygen produces more ordered silica structure, very similar to that of alpha-quartz while oxidation by molecular oxygen created amorphous, non-ordered oxide.

Figures 42, 43 and 44 are shown for the purpose of comparing the $SiL_{2,3}$ edge ELNES for Si oxidized with atomic and molecular oxygen with the results of Batson given in Figure 45 [84] .

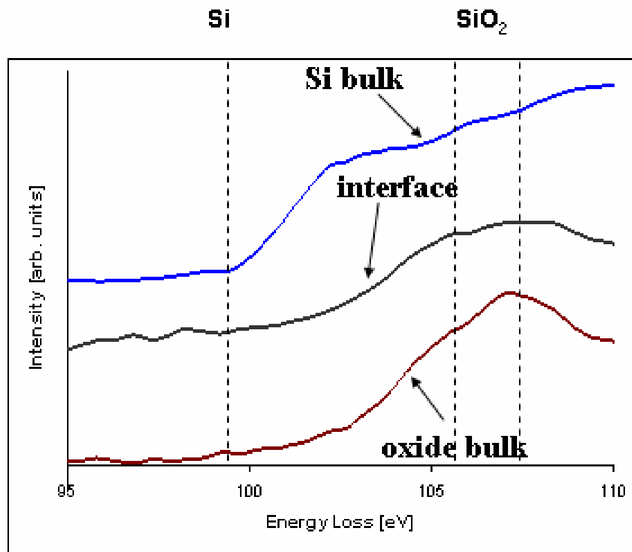

Figure 42. $SiL_{2,3}$ ELNES obtained from Si(100) oxidized by molecular oxygen.

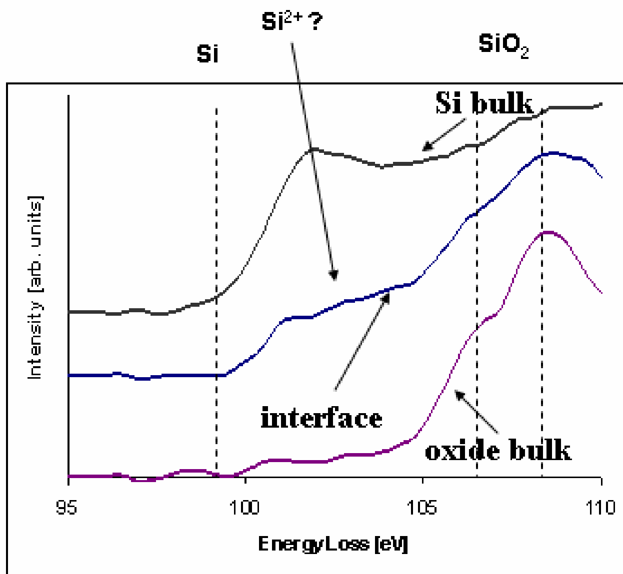

Figure 43. SiL2,3 ELNES obtained from Si(100) oxidized by atomic oxygen.

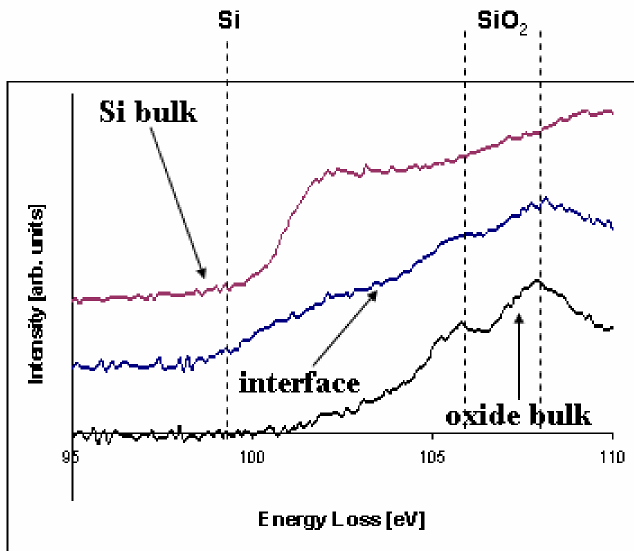

Figure 44. $SiL_{2,3}$ ELNES obtained from Si(111) oxidized by atomic oxygen.

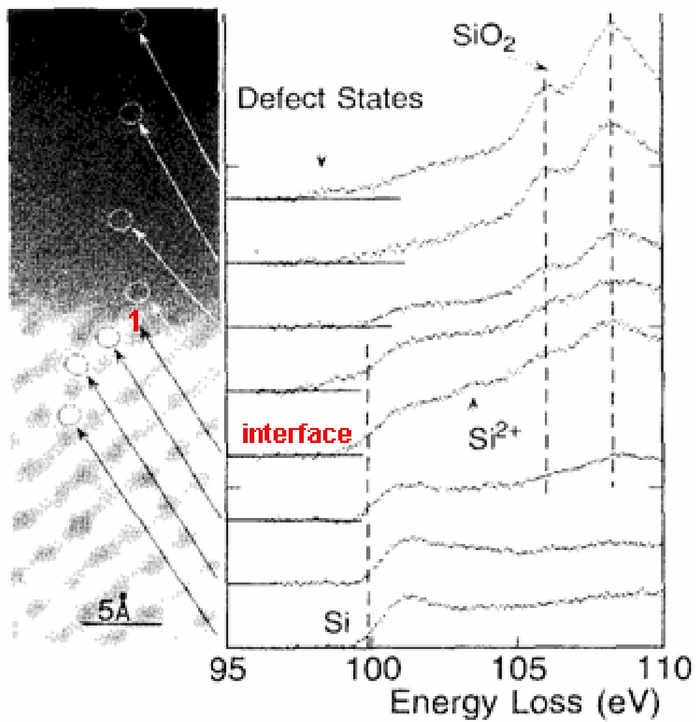

Figure 45. $SiL_{2,3}$ EELS spectra obtained from the Si/SiO_2 interface by Batson. The probe positions are indicated on the left micrograph [84].

The presence of a smooth increase in scattering intensity between the 99.5 eV (Si^o onset) and SiO_2 characteristic peak on 106 eV for Si(100) oxidized by molecular oxygen (differently resolved depending on the spectrometer resolution) can be due to the oxygen sub-stoichiometry, as Batson suggested. This effect is very much reduced in the atomic oxygen oxidized Si(100) (Figure 43) when compared to the Si(100) oxidized by molecular oxygen (Figure 42), therefore implying significantly less defect states present when oxidation is done by atomic oxygen [84]. Batson also observed the feature with its onset at ~103eV in the $SiL_{2,3}$ edge at the interface (position 1 in Figure 45) which can be assigned to the divalent silicon oxidation state where silicon is coordinated by two oxygen and two silicon atoms. The energy difference between the core and vacant level determines the energy position at which the feature occurs. Batson's experiment was done with the 0.2nm probe size, on the VG HB501 STEM.

For the analyzed samples, there might be a small peak with its onset at ~103eV for Si(100) oxidized by atomic oxygen (Figure 43), and this peak is not resolvable for the Si(100) oxidized by molecular oxygen (Figure 42). The possible finding of Si^{2+} state on the interface of Si(100) oxidized by atomic oxygen suggests that transition from Si^o state to the Si^{4+} state occurs through the Si^{2+} state.

Aoto et al. analyzed electronic structure and chemical bonding of the Si/SiO_2 interface both with low-energy loss spectroscopy (LEELS) and XPS [85]. They reported the existence of the Si^{2+} suboxide state very close to the interface. They recorded Si^{2+} peak at the 105eV, in the 2-3A^o thick interface region while Batson is reporting the peak onset at 103eV. This peak has its origin in the transition of electron to the final state from the Si 2p core level state that is shifted deeper about 2eV from the Si 2p core level of Si.

6.5.6.3 OK Energy Loss Near Edge Structure (ELNES) -Results

Oxygen K edge gives information about unoccupied O-p electronic states. The $SiL_{2,3}$ edge is much more subjected by the excitonic effect than the O-K edge, and therefore to the spectrum distortion. The excitonic effect arises from the interaction between the excited electron and the core left behind in the core level. In the case of O-K edge, 1s core hole distorts the edge very weakly which is not the case for the 2p core hole influence on the $SiL_{2,3}$ edge [68] . Therefore, an OK edge gives very good insight about the central O atom surrounding.

Figures 46, 47 and 48 represent background subtracted OK edges ELNES recorded in the bulk oxide and at the Si/oxide interface. Generally, OK edge has its onset at 532eV followed by the sharp maxima at 538eV and smaller maxima at ~560eV.

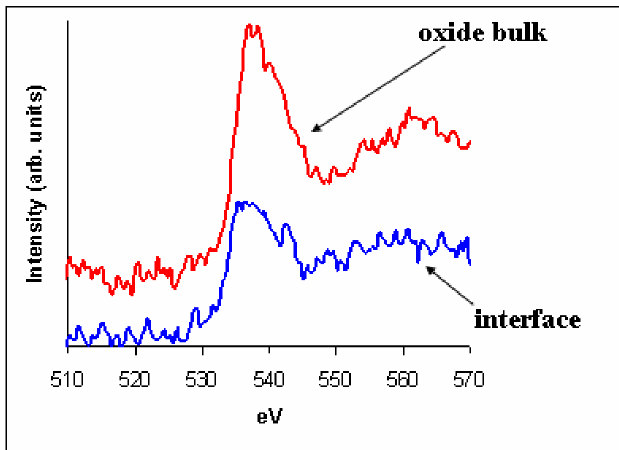

Figure 46. OK ELNES obtained in the bulk oxide and at the Si/oxide interface from Si(100) oxidized by molecular oxygen.

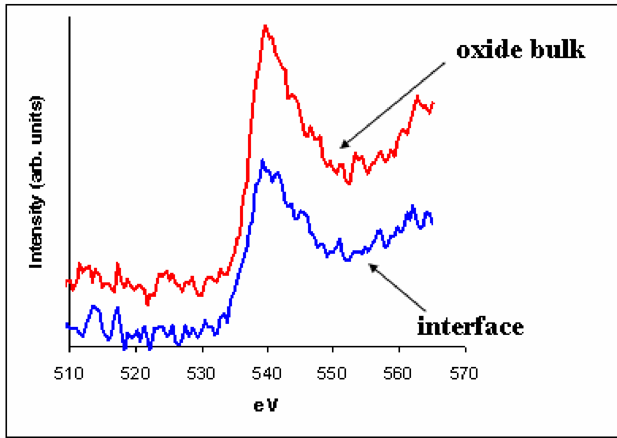

Figure 47. OK ELNES obtained in the bulk oxide and at the Si/oxide interface from Si(100) oxidized by atomic oxygen.

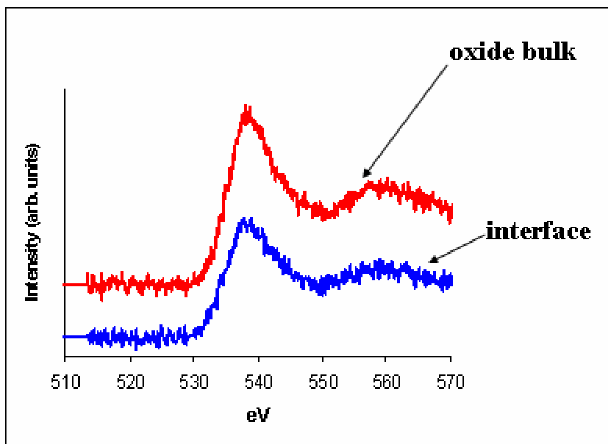

Figure 48. OK ELNES obtained in the bulk oxide and at the Si/oxide interface from Si(111) oxidized by atomic oxygen.

It can be seen that OK edges at 538eV in the bulk oxide are much sharper for atomic oxygen oxidized Si(100) and Si(111) (Figures 47 and 48 respectively), when compared to the molecular oxygen oxidized Si(100) (Figure 46).

The sharp peak of the OK edge arises from the O-O scattering and its intensity decreases as the number of oxygen 2nd nearest neighbors around the central/excited O

atom decreases [86]. Therefore, we can conclude that more O 2nd nearest neighbors are present in the bulk oxide of the atomic oxygen oxidized samples, and this result represents good agreement with the EELS quantification results presented in the next chapter.

OK edges at the interfaces exhibit quite different ELNES for atomic and molecular oxygen oxidized Si. Even at the perfect interface, the last O atom will always be missing some portion of the O nearest neighbors and this will reduce interface peak sharpness. The more O nearest neighbors that are missing, the greater reduction in the peak sharpness and intensity will be. We can see that this is exactly the case for Si(100) oxidized by molecular oxygen (Figure 46) where OK edge recorded on the interface shows quite different ELNES than the OK edge from the bulk oxide. This suggests that the last O atom is in a Si rich environment, implying possible existence of oxygen deficient, suboxide states present on the interface.

It can be seen that the OK edge peak arising from O-O scattering is very intense for both bulk oxide and interface for the atomic oxygen oxidized samples (Figures 47 and 48). This implies that the last O atom is in the O rich environment (like in the bulk oxide) and therefore, the investigated interface is very likely to be abrupt. This obtained result is supported by the previously shown HRTEM results in the chapter 6.3.1.where it was found that interface formed by atomic oxygen oxidation of Si(100) is abrupt and sudden.

6.5.6.4 EELS Quantification -Results

EELS quantification results of $SiL_{2,3}$ and OK edges for Si(100) oxidized by atomic and molecular oxygen are shown in the Figures 49 and 50, respectively, giving

continuously relative percent contents of Si and O in the bulk silicon, across the Si / oxide interface and in the bulk oxide.

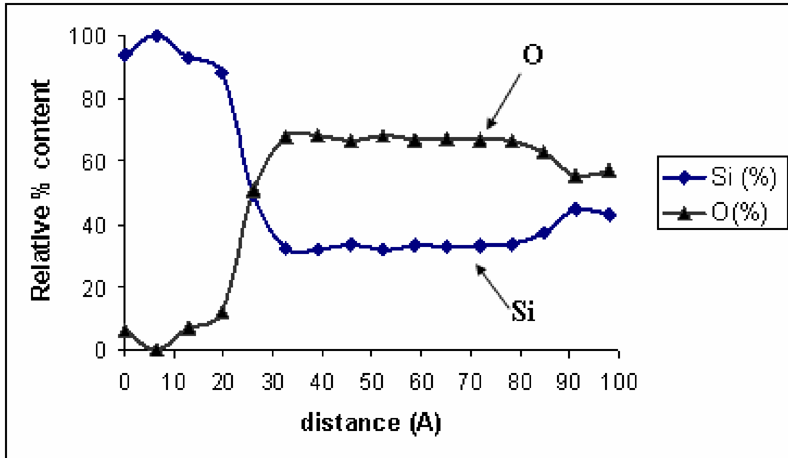

Figure 49. EELS quantification shows relative % contents of Si and O across the Si/oxide interface for Si(100) oxidized by atomic oxygen.

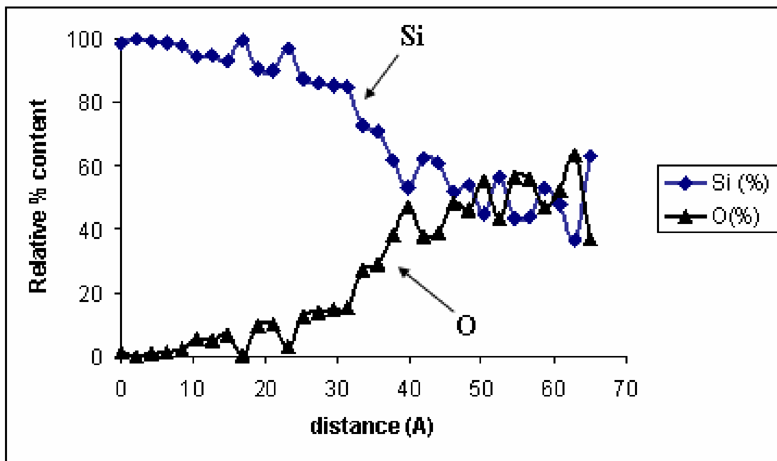

Figure 50. EELS quantification shows relative % contents of Si and O across the Si/oxide interface for Si(100) oxidized by molecular oxygen.

The trend of the lines of Si and O relative percent contents indicates very abrupt interface represented by the data point at ~27A^o from the scan start in the bulk Si. After

this point characterized by ~49%Si and~ 51%O, there is a sudden increase and decrease in the oxygen and silicon content, respectively leading directly to the bulk silicon oxide.

It is easily observed (Figure 49) that there is no significant change in the Si and O percent contents in the bulk oxide region and this region is found to be most frequently characterized by 32.0 % Si and 68.0% O, indicating slightly higher O content than in the stoichiometric silica (33.3%Si and 66.6%O). Even higher oxygen and lower silicon contents than mentioned above are found in certain points characterized by 28.9%Si and 71.07% O, indicating that more oxygen is incorporated and an oxygen richer structure is formed by oxidation in reactive atomic oxygen.

Many more fluctuations in percent contents of Si and O were found in Si(100) oxidized by molecular oxygen (Figure 50), indicating non-stoichiometric silica structure and the presence of suboxide states.

6.6 ATOMIC FORCE MICROSCOPY (AFM)

AFM can be classified in three categories according to the interaction between the tip and the surface of the sample. Contact mode is based on the repulsive force while noncontact mode uses attractive force.

In the **contact mode**, the tip scans the sample in close contact with the surface and the magnitude of repulsive force is 10^{-9} N. The measured cantilever deflection is converted into the height of the features on the sample surface. The problem with this kind of mode can be seen particularly in insulators and semiconductors that can trap

electrostatic charge and consequently create larger attractive forces between the probe tip and the sample surface. **Non-contact mode** utilizes the tip that scans 50-150A^{o} above the surface of the specimen. Attractive Van der Waals forces between the probe tip and the sample surface are measured, along with the change in amplitude, frequency or phase of the cantilever [87].

Tapping mode is the most advanced AFM mode, particularly suitable for the delicate samples that are easy to damage or alter in other modes. Probe tip is placed on the specimen surface to obtain high resolution surface morphology and then lifted from the surface in order not to damage it by dragging. The cantilever oscillates until it reaches the surface when its oscillations start to decrease due to the contact of the tip and the surface and energy loss.

AFM method was used in order to determine the surface roughness of the silicon-oxide formed by the atomic and molecular oxygen. The silicon-oxide surface roughness is supposed to mirror the roughness at the Si/SiO_2 interface. Therefore, determination of surface roughness is very important.

6.6.1 Atomic Force Microscopy (AFM) – Results

The AFM investigation was performed on a Dimension 3100 Digital instruments AFM and images were acquired in the tapping mode. AFM images of Si(100) oxidized by molecular and atomic oxygen at 220°C are given in Figures 51 and 52, respectively. Oxide surface roughness measurement showed that mean square roughness (RMS) is

~0.830nm (Figure 51) and ~1.536nm (Figure 52) for the oxide created by molecular and atomic oxygen, respectively.

Atomic oxygen forms 2 times rougher oxide layer than molecular oxygen on the Si(100) substrate.

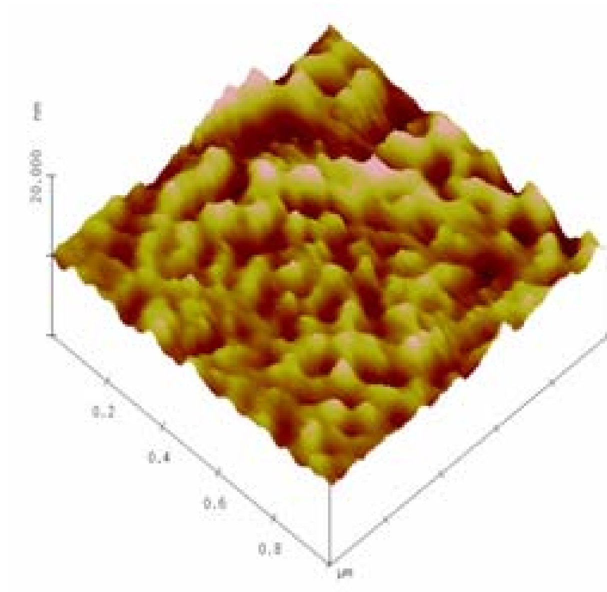

Figure 51. AFM image of Si(100) oxidized by molecular oxygen at 220°C; RMS≅0.830nm.

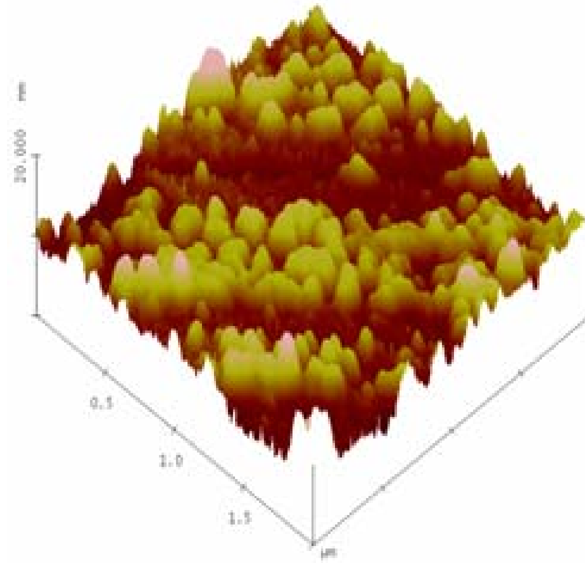

Figure 52. AFM image of Si(100) oxidized by atomic oxygen at 220°C ;RMS≅1.536nm.

Si(111) atomic oxygen oxidized showed 7 times rougher oxide surface (mean square roughness=3.681nm) when compared to the oxide formed by molecular oxygen (mean square roughness=0.479nm). AFM images of Si(111) oxidized by molecular and atomic oxygen at 220°C are shown in Figures 53 and 54, respectively.

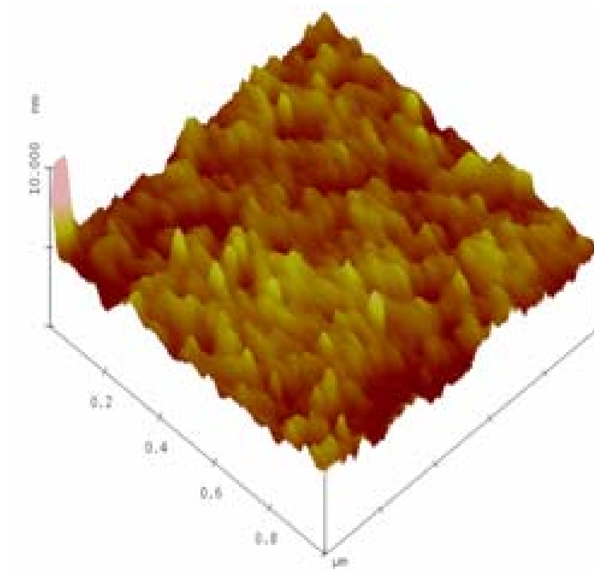

Figure 53. AFM image of Si(111) oxidized by molecular oxygen at 220°C; RMS≅0.479nm.

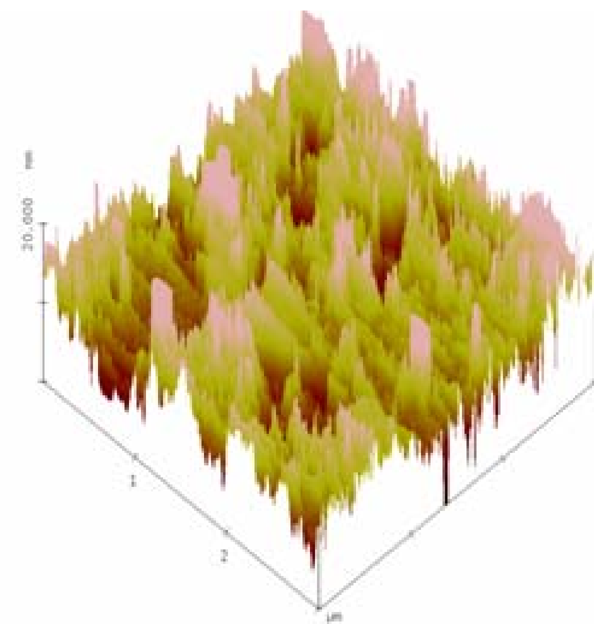

Figure 54. AFM image of Si(111) oxidized by atomic oxygen at 220°C; RMS≅3.681nm.

AFM study of Si(100) oxidized by O_2^+ source at 25°C (Figure 55) revealed very rough oxide surface and mean square roughness was found to be 66.25nm.

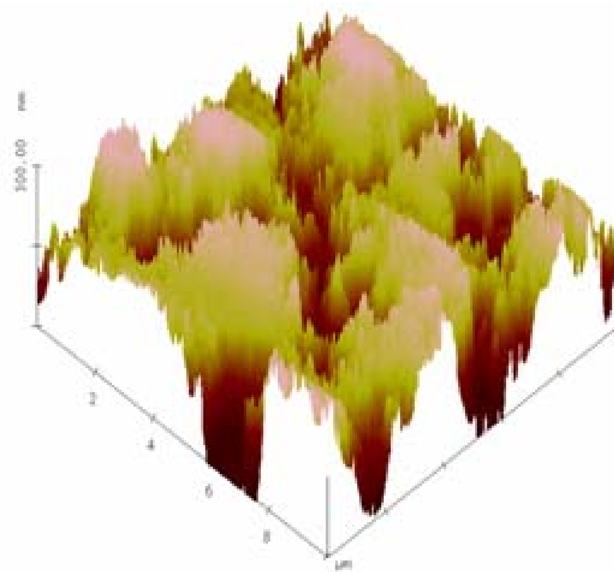

Figure 55. AFM image of Si(100) oxidized by O_2^+ at 25°C; RMS≅ 66.25 nm.

Table 4. Mean square roughness values as determined by AFM.

Sample	RMS (nm)
Si(100) O_2 oxidized	0.830
Si(100) AO oxidized (LDS)	1.536
Si(111) O_2 oxidized	0.479
Si(111) AO oxidized (LDS)	3.681
Si(100) oxidized in O_2^+ source	66.25

A rough oxide observed on this sample could be the result of surface preparation since the oxide removal was by thermal annealing. As mentioned before, in the experimental part (chapter 5.5.1.), the flash anneal treatment at 1400K creates large, pyramidal protrusions on the surface and some investigators also saw etch pits by SEM after this treatment [48, 55]. Flash annealing at 950°C that produces a chemically clean

surface was suggested, but it was also found that impurities such as C and O are present [56].

6.7 X-RAY PHOTOELECTRON SPECTROSCOPY (XPS)

X-ray photoelectron spectroscopy (XPS) is widely used in surface science to study chemical properties of materials. The principle of the XPS is that photons with certain energy are absorbed by a system and core electrons are emitted. The electron is excited from the core state, but it can escape only from the top atomic layers due to low energy of incident photoelectrons. Consequently this is a surface sensitive technique.

Incident photon of energy $h\nu$ causes electron to be ejected from the material with kinetic energy E_k. This process can be described by the formula:

$$E_k = h\nu - E_b \qquad \text{(Equation 48)}$$

where E_b defines binding energy of electron in the particular core state.
Binding energy represents the amount of energy needed to remove an electron from the attraction field of a nucleus [88].

In XPS, the ejected electron final state is independent of bonding effects and it is determined only by E_b. This is a contrast to the EELS, where the final state of the electron is not independent of bonding effects and electron is not free of nucleus attraction.

Energy analyzer measures the kinetic energy of these electrons. Kinetic energy of an electron measured depends on the binding energy and the work function of the spectrometer.

Peaks in the XPS spectrum correspond to the occupied energy levels in atoms, while EELS probes unoccupied states. Intensity of the peaks depends on the number of atoms present.

Knowing that binding energy of core electrons is determined by the chemical environment, it is possible to determine composition of the sample or the valence state of a certain element. By chemical shift measurement, it is possible to determine local coordination in a system [72].

XPS method was used to determine oxidation states of the silicon in the oxide created by the atomic and molecular oxygen. Since this technique is limited to the surface information, EELS was used as the complementary method.

6.7.1 X-Ray Photoelectron Spectroscopy (XPS) - Results

Kratos Axis ULTRA Imaging X-ray Photoelectron Spectrometer was used to obtain information about the valence state of silicon in the oxide. This instrument has monochromated X-ray sources for high-energy resolution analysis and is capable of small area detection.

Since it is a high-resolution analytical spectrometer, it allows sample tilting for depth resolved analysis. This surface technique enables us to obtain spectral information that is collected from a depth of 10-100 A^o.

Figures 56-61 are XPS spectrums obtained from three Si samples oxidized by laser detonation atomic oxygen source (LDS) and O_2^+ source.

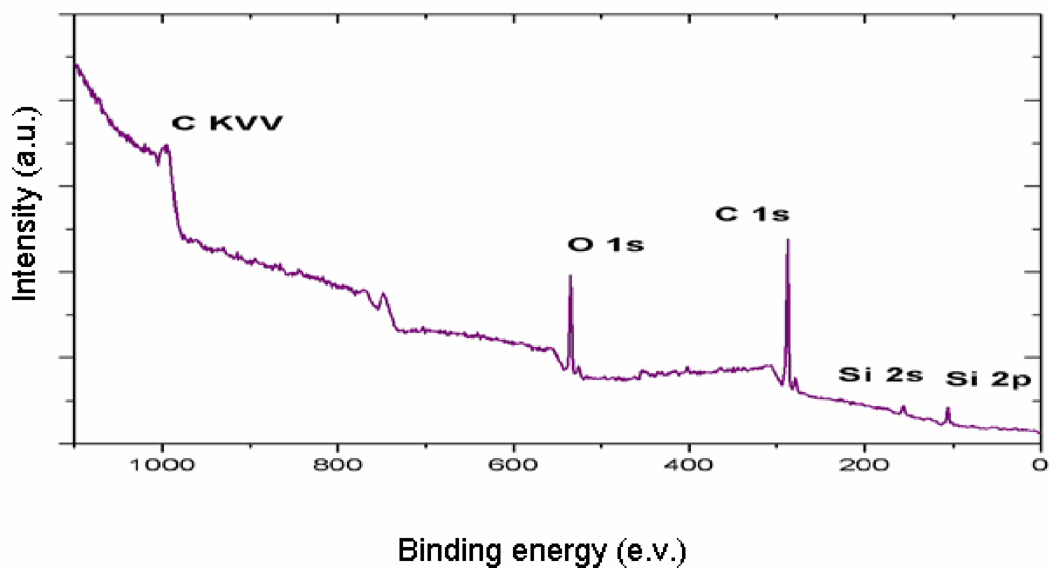

Figure 56. XPS spectrum obtained from Si(100) oxidized by atomic oxygen at 220°C.

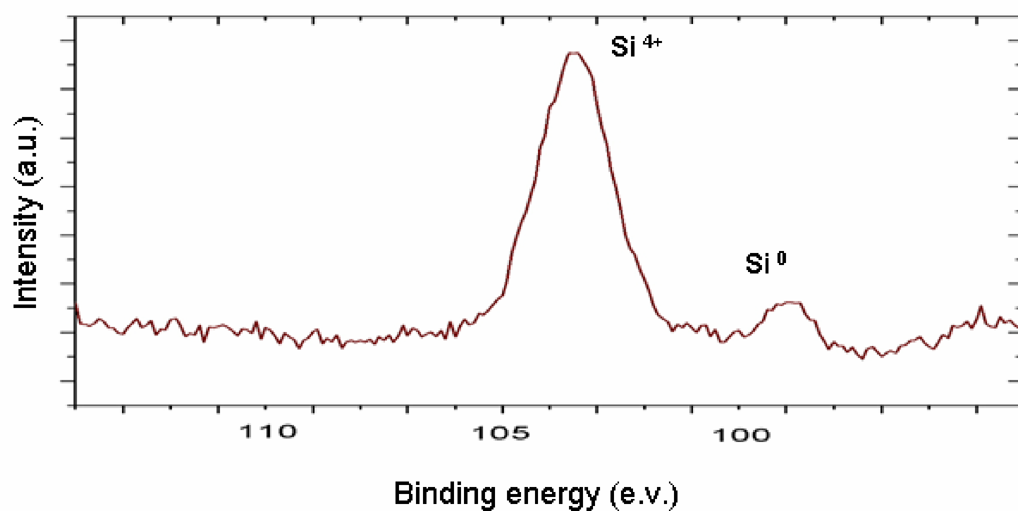

Figure 57. Si^{4+} and Si^{0} valence states observed in XPS spectrum obtained from Si(100) oxidized by atomic oxygen at 220°C in LDS.

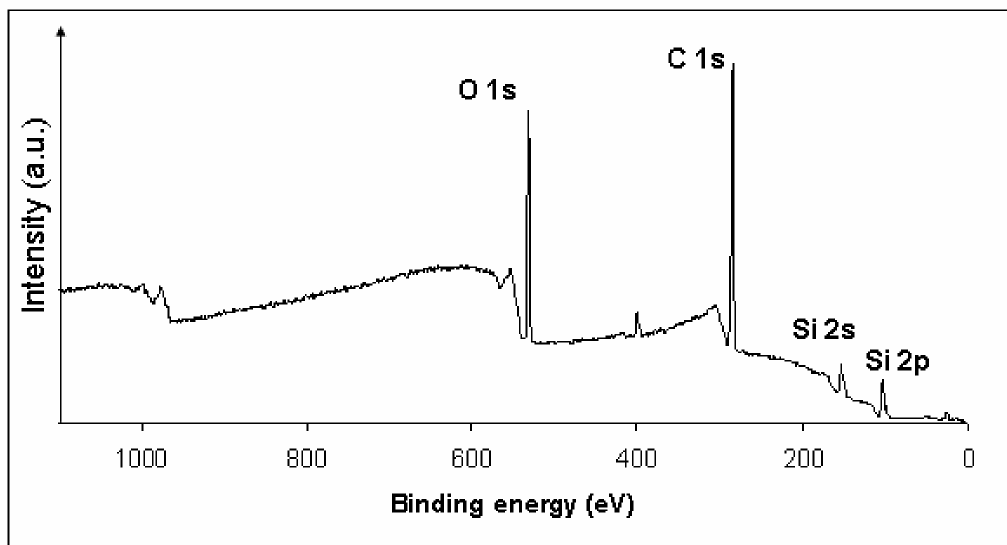

Figure 58. XPS spectrum obtained from Si(111) oxidized by atomic oxygen at 220°C in LDS.

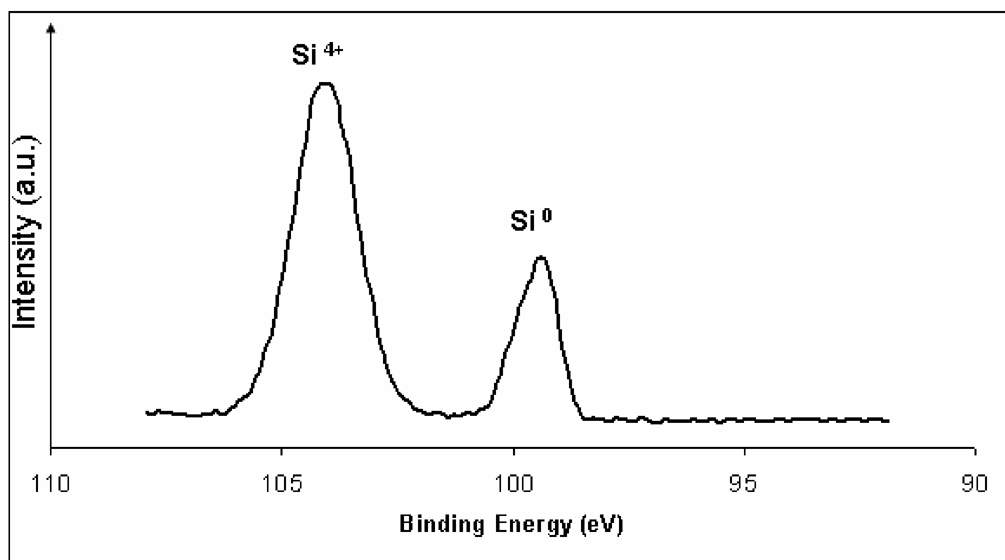

Figure 59. Si^{4+} and Si^{0} valence states observed in XPS spectrum obtained from Si(111) oxidized by atomic oxygen at 220°C in LDS.

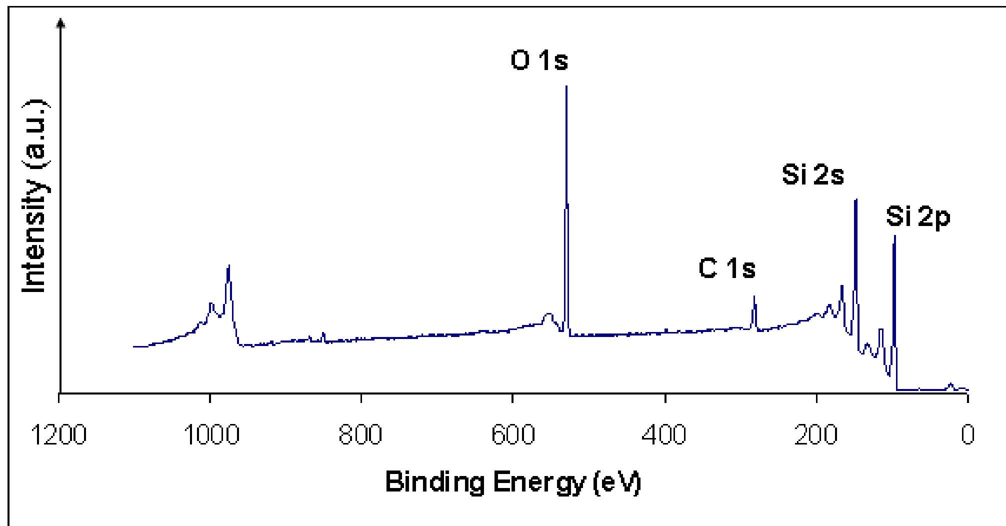

Figure 60. XPS spectrum obtained from Si(100) oxidized in O_2^+ source at 25°C..

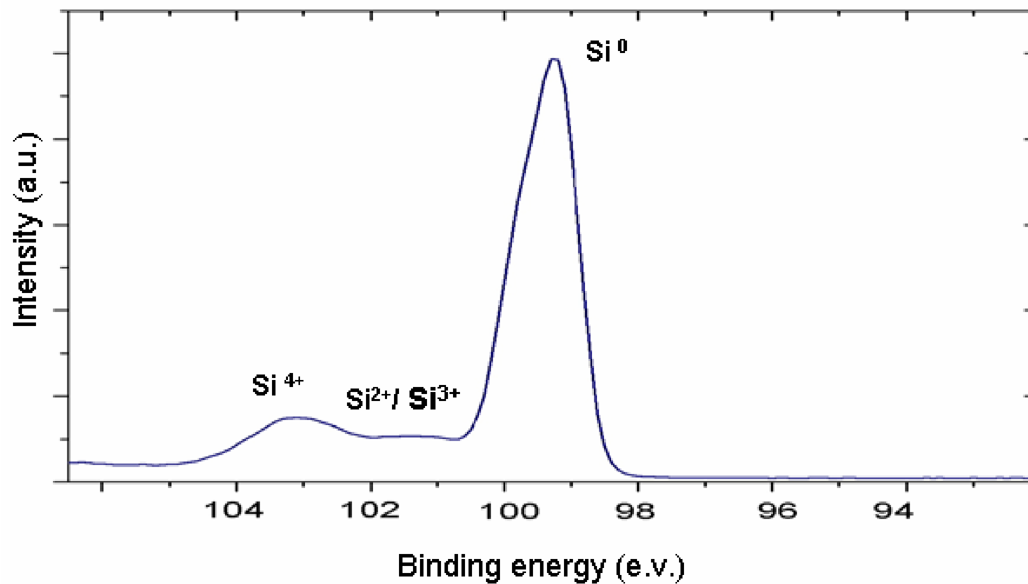

Figure 61. Si^{4+}, Si^{2+}/Si^{3+} and Si^0 valence states observed in XPS spectrum obtained from Si(100) oxidized in O_2^+ source at 25°C.

Figure 56 shows an XPS spectrum of elements detected in Si(100) oxidized by atomic oxygen in a laser detonation source at 220^oC. O 1s, C1s and Si edges are clearly visible in this spectrum. The presence of the carbon could be due both from the laser detonation source and sample handling. The position of this peak is at 285eV. The OK peak is present at 532eV and that is its characteristic position in the oxide compounds. Si2p peak is at 99.3eV while the Si2s peak can be found at ~151eV.

A closer look at the Si 2p peak is shown in Figure 57. One can see that a small peak is present at 99.3 eV and originates from the Si substrate. The area of the large peak present at 103.5eV is proportional to the silicon oxide coverage and its position reveals that Si^{4+} oxidation state is present within the oxide.

Figure 58 represents XPS spectrum of Si(111) oxidized in the laser detonation source by atomic oxygen at 220^oC. Similarly to Figure 56, one can see that OK (532eV), CK (285eV), Si2p (99.3eV) and Si2s (151eV) peaks are present. More details about the Si2p peak can be seen in Figure 59. Only two peaks corresponding to Si^0 (99.3eV) and Si^{4+} (103.5eV) oxidation states are visible, suggesting that no suboxide states are present.

An XPS spectrum of Si(100) oxidized in O_2^+ source is shown in Figures 60 and 61. From these spectra, it can be seen that Si2s and Si2p peaks originated from the silicon substrate are very intense as compared to the Si peaks of the silicon oxidized in LDS. The Si^o peak is at 99.3eV while the Si^{4+} peak is at 103.5eV. The intense peaks from the underlying substrate suggest that the O_2^+ source produced oxide that partially covered the silicon substrate. Also, a small hill is present between the peaks at positions 99.3eV and 103.5eV, thus indicating that suboxides are very likely to be present in this sample.

However, decreased intensity of C edge in O_2^+ oxidized sample as compared to the oxidation in LDS is detected.

7.0 DISCUSSION

The agreement of the experimental results with the hypotheses presented in the chapter 4 will be discussed here.

The oxide created by AO on Si(100) has an average thickness of 5-6nm, while a passivated layer formed by MO was only 2-3nm thick, as determined by HRTEM and confirmed by RBS (5.8nm for AO oxidized Si(100)).The silica layer created by AO on Si(111) is 7-8nm thick, as determined by HRTEM and checked by RBS (8.73nm for AO oxidized Si(111)). It is 3-5 nm thick when formed by O_2.

From the above thickness numbers, we can see that RBS and HRTEM methods give excellent agreement and should be used as complementary techniques for precise thickness determination of the thin oxide layers.

Oxidation proceeds considerably faster on Si (111) than on Si (100) due to the 1.7 times larger linear constant rate for Si(111). Our oxide thicknesses obtained are in good agreement with this fact.

A model for the oxidation of Si by 5eV AO, based on the thermionic emission, is presented here. This model can explain the differences between the oxidation mechanism of Si by the atomic and molecular oxygen. The thermionic emission model for the low temperature oxidation by O_2 was described previously, in chapter 2.4.2. Here we present

a modified thermionic emission oxidation model to describe the oxidation of Si by 5eV AO.

Thermionic emission model for Si oxidation by 5eV AO

Oxidation by 5eV AO at low temperature differs from the oxidation by O_2 described by the thermionic emission model presented in chapter 2.4.2. This model is modified as follows:

1a. e^- (conduction band of Si) $\rightarrow$ e^- (Si surface)

2a. e^- (Si surface) $\rightarrow$ e^- (free in SiO_2)

3a. e^- (in SiO_2) +O (on the surface) $\rightarrow$ O^-(chemisorbed)

4a. Si^+ (at Si surface) + O^- + O $\rightarrow SiO_2$

Step 1a is the flux of electrons to the Si surface

Step 2a is emission of electrons over the energy barrier

Step 3a is electron attachment to O

Step 4a is reaction of atomic and charged species.

The critical step is step 2, which was rate - limiting for the oxidation by O_2, is now more rapid (step 2a). A possible reason for this is the kinetic energy of AO, which provides local heating of the substrate, since 5eV would correspond to thermal energy of T $\approx$ 58000K. As the temperature increases, the number of charge carriers increases because there is more thermal energy available. More electrons can get enough energy to break free. This is known as intrinsic conductivity and it is based on the electron-hole pairs created by thermal excitation.

For each electron transferred from valence to conduction band, a hole is formed in the valence band and that leads to increase in both electron and hole concentration. As temperature increases, band gap energy decreases due to the expansion of crystal lattice and weakening the interatomic bonds. Hence less energy is required to break these bonds and produce an electron in the conduction band. Significantly more electrons will be present in the silicon conduction band and more electrons will be transferred by thermionic emission to the SiO_2 conduction band. The effect of local heating will affect thermionic emission in such a way that it will enable overcoming larger energy barrier. Consequently, the oxidation reaction will continue.

In step 4 -the decomposition of O_2^- into the neutral and charged species is not present in the mechanism for AO oxidation and this will also contribute to the increase of the reaction rate. Steps 3a and 4a are modified as compared to the oxidation by O_2. Monoatomic species already present. It does not need to be created by the dissociation of O_2^- ions, as in the model for oxidation by O_2. This could increase the reaction rate in the linear oxidation regime.

The parabolic step is most probably affected by the diffusion of O atoms through the oxide film. This diffusion will be much faster due to the smaller size of the O atoms, and can continue for longer time. O and O_2 would be the diffusing species in the case of AO and MO oxidation, respectively.

There are additional effects that could facilitate oxidation rate by 5eV AO in the parabolic regime as compared to the oxidation by O_2:

1. 5eV AO can break the bonds upon arrival at the SiO_2 surface. This will create defect states (non-bridging O atoms in the form –Si-$O^{\delta-}$) that can act as a new

source of electrons. This will lead to continued electrons supply, thus causing extension of parabolic regime. (It was noticed that limiting thickness in parabolic regime does not saturate even at 10ML for AO while it saturates at 1.5ML for O_2) [9].

2. Creation of the more ordered structure observed for Si oxidized by AO (EELS and SAED results) can provide high diffusivity paths for monoatomic AO species. More ordered structure is formed by AO since the 5eV provides energy for the oxide to transform towards the more thermo dynamical stable oxide form.

   It was suggested earlier that enhanced oxidation rate in the linear regime could be affected by structural channels formation, by providing easy diffusivity paths [89].

In a conclusion, the hypothesis I from chapter 4 is supported by the HRTEM and RBS experimental results on the oxide thickness. The modified thermionic emission model is able to explain enhanced oxidation rate in the initial, linear oxidation regime.

It was assumed that silica layer formed by AO should be more ordered and homogeneous when compared to the oxide created by O_2. This hypothesis is supported by the obtained SAED and ELNES results.

ELNES is very sensitive to the chemical and structural environment surrounding the particular excited atom. Chemical shift of the ionization threshold usually accompanies the ELNES. Interpreting the near edge structure can be achieved by the 'fingerprint approach' where common features from the elements in similar environments are identified. The "fingerprint method" is particularly useful in determining the atom surrounding and its valence [68].

$SiL_{2,3}$ edge ELNES obtained from Si(100) oxidized by AO showed similarities with the results of Garvie et al., suggesting that structure similar to alpha-quartz is formed by AO reaction on silicon while amorphous silica is created by MO oxidation. Clearly resolvable diffraction rings in HRTEM, with the d-spacings corresponding to that of alpha-quartz for the AO formed oxide, strongly support ELNES results.

Those findings indicate that AO reacts with silicon dramatically differently than MO, introducing order into the formed silicon oxide layer. This additional order could be due to the AO specific reaction with certain atomic sites on the Si substrate. EELS quantification and Spectrum Imaging data showed no fluctuations in the Si and O percent content from the interface to the oxide surface, therefore suggesting very homogeneous structure for the AO oxide formed on Si(100). Si(111) also showed larger % of O in the bulk oxide when compared to the stoichiometric silica.

SAED and EELS data on the silica created by hyperthermal AO agree very well with the ozone created silica, which is logical since the ozone is a strong oxidant due to the decomposition on the atomic oxygen and oxygen molecule.

The HRTEM, EELS and XPS results support interface abruptness and suppression of suboxide states, assumed in the hypothesis III.

Our Si/SiO_2 interface thickness measurement by intensity profiling of HRTEM micrographs revealed that the thickness of the AO formed interface on Si(100) was greatly reduced as compared to the MO formed one, that was found to be ~1nm.

We obtained confirming results from the EELS measurements where $SiL_{2,3}$ edge onset shift from Si^{o} (99.5eV) to the Si^{4+} (103.5eV) valence state was found to be very

abrupt, without showing any additional peaks that appear when the suboxide states are present. These results were confirmed by XPS.

The $L_{2,3}$ edge ionization is caused by the transfer of the 2p electrons mainly to the 3d final states. Going from the semiconductor (bulk Si) to the insulator (SiO_2), an energy band gap is introduced, raising the first available empty state and therefore increasing the ionization threshold energy by ~4eV [68].

The reduction in the Si/SiO_2 interface thickness and clear presence of only Si^{4+} valence state for Si(100) oxidized by ozone was noted by the other investigators. They also found that suboxides formation was greatly suppressed [30].

The interface thickness for Si(111) was found not to be hardly affected by the reactive AO. It appeared fairly smooth for both molecular and atomic oxygen oxidizing species.

The reduction of interface thickness and suboxide states formed on Si(100) can be explained by the different initial oxidation steps for AO and MO oxidation, further discussed in the following paragraph.

The effect of the initial Si-O bonding on interfacial morphology

It was found that adsorption of ozone is not affected by the defect sites which are favorable locations for the initial adsorption of oxygen molecules [90]. Also, less than 10% of the O atoms are located at the bridge site between the Si dimers and the majority of the O atoms are inserted into the backbonds below the Si dimer [41].

Molecular oxygen oxidation is characterized by the chemisorption of O on the bridge or top site of the upper layer of the Si substrate, which is energetically favorable since the energy release enables O atom migration into the first back-bonds [91].

Figure 62 shows the initial oxidation steps for molecular oxygen oxidation of Si(100), proposed by Watanabe et al. [91]. These authors were investigating initial oxidation steps by scanning reflection electron microscopy (SREM). From the change in oxygen peak intensity monitored by Auger Electron Spectroscopy (AES), the kinetics of the initial oxidation steps was determined.

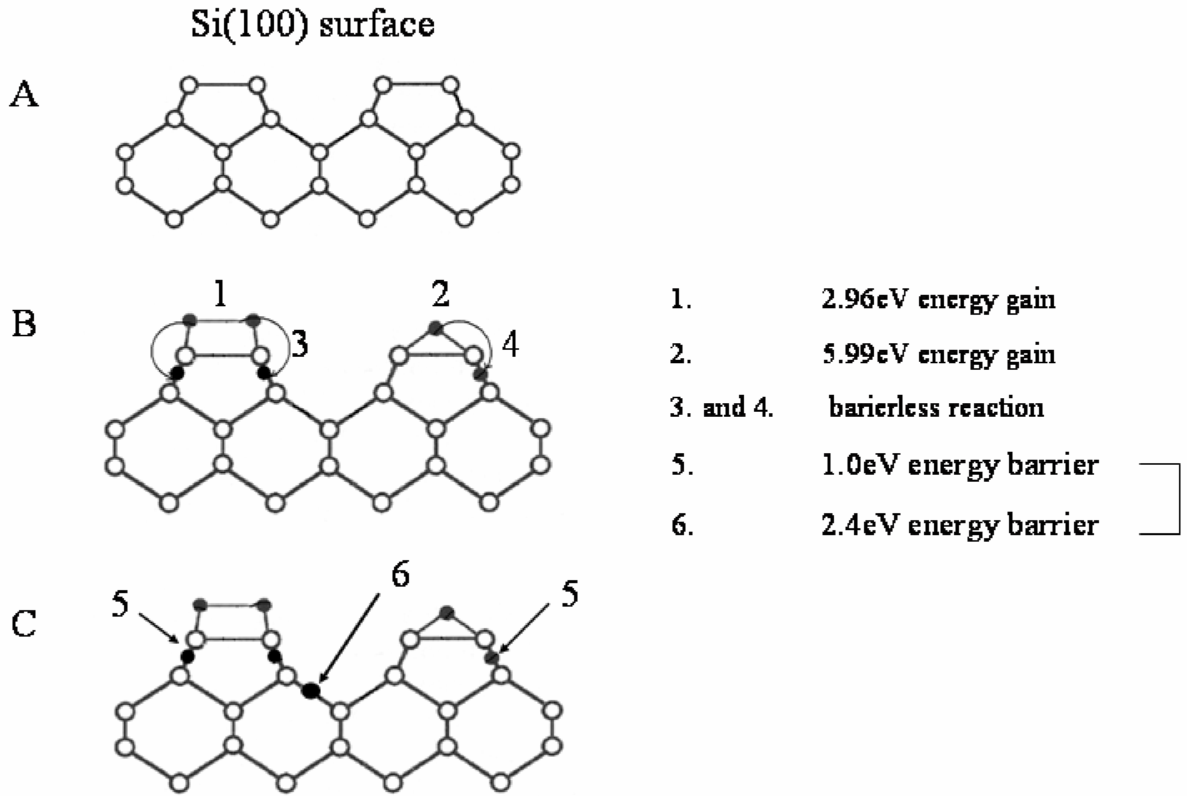

Figure 62. Schematic of initial oxidation steps of Si(100) surface by molecular oxygen [91].

The steps 1-6 shown in the figure above represent the following:

Step 1 and 2 –O chemisorption on the top and bridge site and metastable configurations forming

Step 3 and 4 – O atom migration from the uppermost to the first layer backbond

Step 5- O atom insertion into the first subsurface layer

Step 6- O atom insertion into the second subsurface layer

The very first step is O atom chemisorption on the uppermost layer resulting in energy gain and metastable configuration formation. Since this formation is not stable, it migrates through steps 3 and 4, therefore represented as barrierless reactions. If O atom was inserted directly in this first layer backbond (positions 3 and 4), the energy of 1.0eV must be supplied (step 5). O atom insertion into the second backbond layer requires energy of 2.4eV and the occupation of this position can be achieved only through the heating. Positions 3 and 4 are available through the metastable species migration, while direct O insertion in positions 5 and 6 requires energy.

Figure 63 represents our modification of the model of Watanabe et al. for the oxidation by 5.1eV atomic oxygen species.

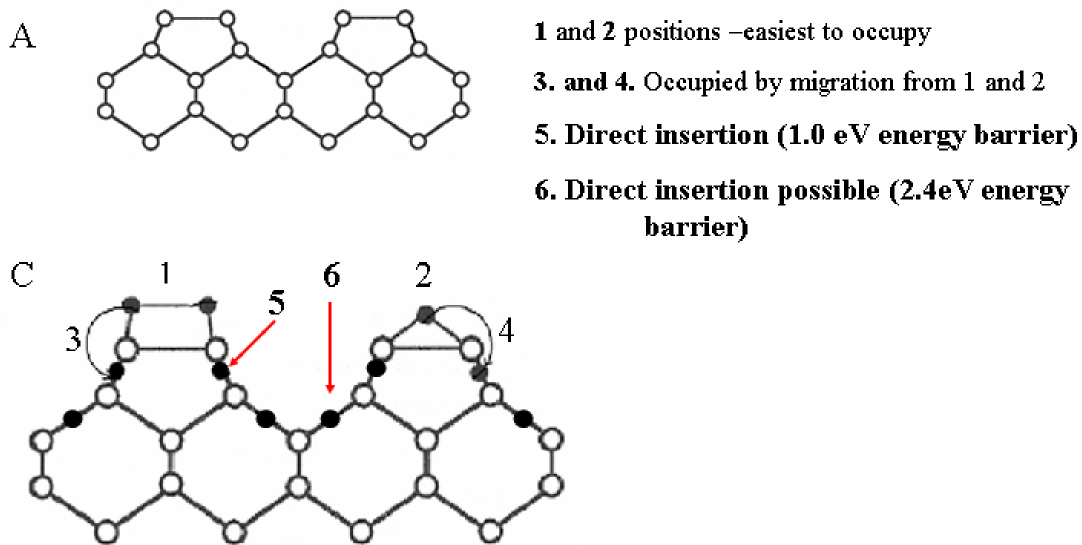

Figure 63. Schematic of initial oxidation steps of Si(100) surface by hyperthermal atomic oxygen.

Since atomic oxygen possesses 5.1eV, uppermost, first and second backbond layer are easily occupied in the first, initial oxidation step-interface reaction is very rapid. Positions 1 and 2 are still easiest to occupy. Positions 3 and 4 can be occupied both by migration of metastable adsorption species from 1 and 2, or by direct atomic oxygen insertion. Positions 5 and 6 also can be occupied by the direct insertion of atomic oxygen.

In conclusion, many more positions for direct insertion in the first step are available to the energetic atomic oxygen. Three monolayers can be oxidized by atomic oxygen instead of only one by the molecular oxygen in the very first step.

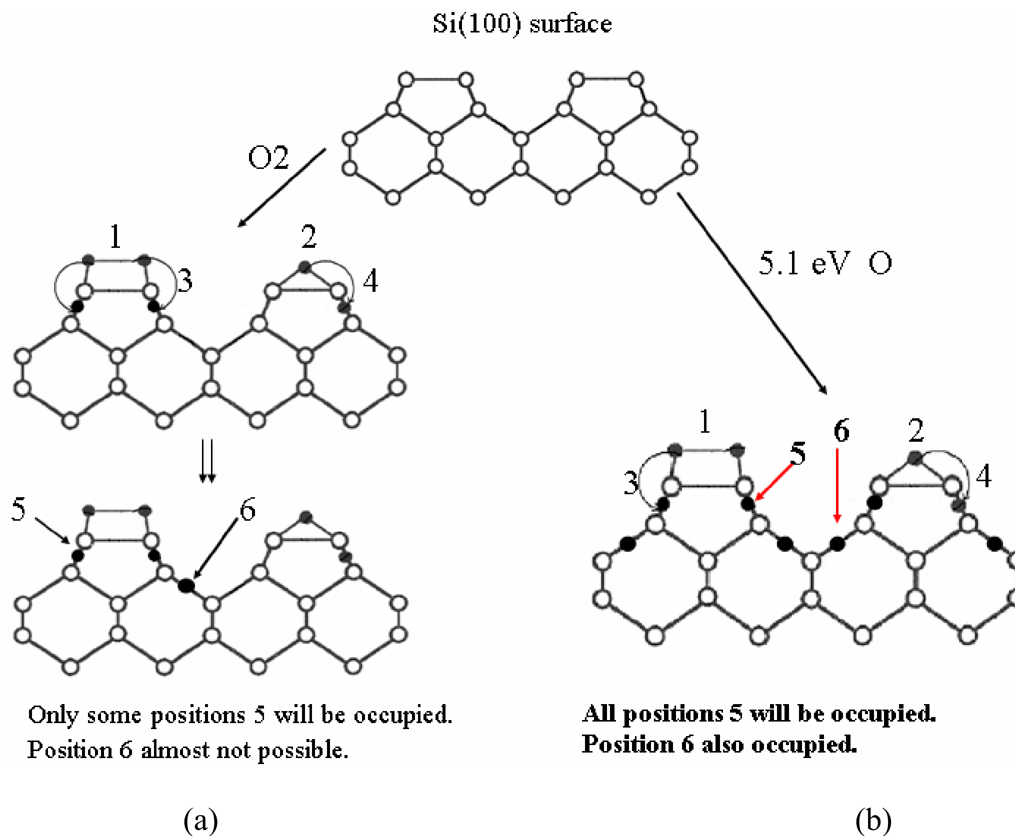

Figure 64. Comparison of initial oxidation steps of Si(100) surface by (a) molecular oxygen (b) hyperthermal atomic oxygen.

From Figure 64, it is obvious that the initial adsorption for molecular oxygen will occur mostly at the uppermost layer and energy released can be used for the conversion of metastable adsorbed species into the more thermodynamically stable species that will be inserted in the first or second backbond layer (Figure 64-a).

Atomic oxygen is supplied with 5.1eV energy and it has no bonds to be broken; it can directly attack backbonds in the first and even second subsurface layer of Si, without a need to go through the chemisorption process first in order to gain necessary energy to finally reach backbonds. More sites (1, 2, 3, 4, 5, and 6) are available to the direct atomic oxygen adsorption as opposed to the molecular oxygen species (1 and 2) (Figure 64-b).

Direct consequence of the above mentioned assumptions would be the increased rate of oxidation for atomic oxygen as compared to molecular oxygen, as was observed experimentally.

At the same time, facile, direct adsorption of reactive atomic oxygen on the uppermost, first and second backbonds layers will create much more abrupt interface. This interface has less transitional states, as confirmed by presented experimental results.

Additionally, this amount of energy gives the possibility to atomic oxygen to even attack the H-terminated Si atoms that are much less reactive when subjected to molecular oxygen.

Interestingly, AFM studies revealed that AO forms a rougher silica layer (mean square roughness ~1.536nm) than MO (mean square roughness ~0.830nm) on Si(100) substrate [64] .

Roughness increase due to AO is much more pronounced for (111) orientation-7 times. We obtained mean square roughness=3.681nm for AO oxidized sample, whereas the oxide formed by O_2 had a mean square roughness=0.479nm.

Si(100) oxidized by O_2^+ showed the roughest oxide layer, with the mean square roughness of 66.25nm. The reason for such an increased roughness could be native oxide removal by thermal annealing.

The increase in the oxide surface roughness due to AO oxidation is quite surprising. This is due to the fact that the Si/oxide interface is very flat, and this interface morphology should be mirrored on the oxide surface. More experimental work is needed in order to account for this observation.

8.0 CONCLUSIONS

The structure of the oxide and interface layer formed on Si(100) and Si(111) at 493K by hyperthermal AO or MO were compared by a variety of experimental techniques including AFM, RBS, HRTEM, SAED,EELS and XPS.

Thickness, surface roughness and valence states of the oxide layer formed in O_2^+ source on Si(100) substrate were investigated by RBS , AFM and XPS.

- As predicted in the hypothesis I, the thickness of the oxide layer formed by AO were found to be almost doubled when compared to the MO formed interface on Si(100).

  Similarly, the thickness of the oxide layer formed by AO were found to be almost doubled in comparison to the oxide layer formed by MO on Si(111).

  Oxidation model based on thermionic emission was modified. New model is able to explain increased oxidation rate in the initial, linear oxidation regime. The enhanced electronic transfer, due to 5.1eV AO, from Si to SiO_2 is proposed to influence the linear oxidation regime.

  The diffusion of smaller O atoms, as compared to the O_2 molecules, was speculated to be responsible for the extended parabolic regime during the AO oxidation. Also, structural channels effect and increased availability of electrons

are proposed to be the possible reasons for the extension of the parabolic regime in AO oxidation.

The oxide layer formed on Si(100) by O_2^+ was found to be very thin and non-uniform. XPS investigation of this silicon oxide showed that the suboxides are produced when silicon is oxidized in O_2^+ source.

- Hypothesis III is confirmed, since the Si/SiO_2 interface formed by AO on Si(100) in LDS was found to be very abrupt. Also, the presence of suboxide transitional states was greatly reduced. Only the presence of Si^{4+} state was clearly detected by EELS and XPS. This is in good agreement with the previous studies on the Si oxidized by ozone.

  The interface formed by MO on Si(100) revealed transitional states.

  Oxidation of Si(111) by both AO and MO created flat and abrupt interface, indicating that AO species impact on (111) orientation is not so pronounced as far as interface abruptness is concerned.

- The interface abruptness due to AO oxidation was explained by the ability of AO to equally attack uppermost, first and second backbond layers. An analysis of the possible bond breaking along with the bond energies consideration was given.
- The oxide scale formed by AO on Si(100) was found to be very homogeneous and uniform, with no fluctuations in the Si and O content from the interface to the oxide surface. More oxygen than in stoichiometric silica was incorporated (28.9% Si and 71.07% O). Fluctuations in percent content of Si and O were recorded in the oxide layer formed when Si(100) was oxidized in O_2.

Si(111) oxidized by AO showed more oxygen incorporated in the bulk oxide, similar to the (100) orientation oxidized by the same species.

This was found to be in excellent agreement with the hypothesis II and homogeneous oxide structure observed for the oxidation of Si by ozone.

- As predicted by the hypothesis II, the oxide layers formed by AO on both silicon orientations were found to be less random. More ordered –structure, similar to that of alpha-quartz, was identified as opposed to the amorphous silica formed by MO. Differences in the AO and MO initial oxidation steps were proposed to be responsible for the observed phenomena. The ability of hyperthermal AO to equally attack uppermost, first and second backbonds layer seems to be the most possible explanation for the results reported in this work.
- The oxide surface roughness was determined to be 2 times larger for the Si(100) oxidized by AO, as compared to the silica layer formed by MO. The surface roughness of the oxide formed on Si(111) by AO was found to be 7 times larger in comparison to the oxide layer formed by the MO on Si(111).

  The oxide layer formed on Si(100) by O_2^+ was found to be the roughest of all investigated oxides. These roughness results cannot be explained at this point, additional experiments are needed.

9.0 FUTURE WORK

Work presented in this thesis was based on ex-situ investigations that provided valuable information about the structural properties of the oxide scales and silicon/oxide interfaces formed by atomic and molecular oxygen. Future work will include in-situ TEM, which will give better insight in the real-time oxide formation. The synergistic effect of in-situ Si oxidation and UV irradiation is the ultimate goal in order to gain fundamental understanding of silicon oxidation in an LEO environment. Combination of different factors present in LEO and in-situ study of their effect on materials degradation can result in smarter protective coatings design.

BIBLIOGRAPHY

1. Banks B. Ruthedge S. and Groh K. "Low Earth Orbital Atomic Oxygen, Micrometeoroid and Debris Interactions with Photovoltaic Arrays" presented at the *11th Space Photovoltaic Research and Technical Conference* (SPRAT XI), Cleveland, Ohio, May 7-9, 1991

2. Banks B. and LaMoreaux C. "Performance and properties of atomic oxygen protective coatings for polymeric materials" presented at the *24th International SAMPLE Technical Conference*, Toronto, Canada, October 20-22, 1992

3. Minton T. and Garton D. "Dynamics of atomic- oxygen-induced polymer degradation in low earth orbit. Chemical dynamics in extreme environments." *Advanced series I physical chemistry*. ed. Dressler R. A. World Scientific. Singapore (2000)

4. Leger L. "Atomic Oxygen Reactions with Shuttle Materials at orbital Altitudes", NASA TM-58246, 1982

5. Tagawa M. Yokota K. Ohmae N. and Kinoshita H. "Volume diffusion of atomic oxygen in alpha-SiO_2 protective coating" *High Perform Polym.*12, 53-63 (2000)

6. Banks B. Rutledge S. de Groh K. and Auer B. *NATO Advanced study institute conference* Pitlochry, Scotland, July 7-19 (1991)

7. Banks B. Rutledge S. and Auer B. "Atomic Oxygen Undercutting of Defects on SiO_2 Protected Polyamide Solar Array Blankets" *119th TMS Annual Meeting* and Exhibit, Anaheim, February 18-22 (1990)

8. Engstrom J. and Engel T. "Atomic versus molecular reactivity at the gas-solid interface: The adsorption and reaction of atomic oxygen on the Si(100) surface" *Physical Review B*, vol 41, 2, pg 1038-1041 (1989)

9. Engstrom J. Nelson M. and Engel T." Reactive atom-surface scattering: The adsorption and reaction of atomic oxygen on the Si(100) substrate" *J.Vac.Sci.Technol.*A7(3), pg 1837-1840, (1988)

10. Tagawa M. Yokota K. Ohmae N. Kinoshita H. and Umeno M. "Oxidation properties of hydrogen-terminated Si(100) surface following use of hyperthermal broad atomic oxygen beam at low temperatures" *Jpn.J.Appl.Phys.Vol* 40, pg 6152-6156, (2001)

11. Nakazawa M. Nishioka Y. Sekiyama H. and Kawaze S. "Investigation of the SiO_2/Si interface. II. Oxidation of an HF cleaned Si(100) surface using photoemission spectroscopy with synchrotron radiation" *J. Appl. Phys*. 65(10) 4019-4023 (1989)

12. Engstrom J. Bonser D. and Engel T. "The reaction of atomic oxygen with Si(100) and Si(111) II. Adsorption, passive oxidation and the effect of coincident ion bombardment" *Surf. Sci*. 268, pg 238-264 (1992)

13. Deal B. and Grove A. "General Relationship for the Thermal Oxidation of Silicon" *Journal of Applied Physics* 36, 12, 3770-3778 (1965)

14. Evans U. "The Corrosion and Oxidation of Metals", *St. Martins Press, New York,* p. 826 (1960)

15. Revesz A. *Phys. Stat. Sol*. 19 (1967), 193

16. Irene E. "Si oxidation studies; A revised model for thermal oxidation" *J. Appl Phys.* 54, 5416, 1983

17. Doremus R. "Oxidation of Silicon: Strain and linear kinetics" *Thin Solid Films*, 122, 191-196, 1984

18. Fargeix A. "A revised analyses of dry oxidation of Si" *J. Appl. Phys*. 54, 2878, 1983

19. Murali V. and Murarka S. "Kinetics of ultrathin SiO_2 growth" *J. Appl. Phys*. 60, 2106, 1986

20. Cabrera N. and Mott N. F. "Theory of the Oxidation of Metals" *Rept. Progr. Phys*. 12, 163, 1948

21. Fehlner F. "Low Temperature Oxidation", *The Electrochemical Society, INC.* Pennington, New Jersey (1986)

22. Mott N., *Trans. Faraday Soc*. 36 (1940), 472; 43(1947), 429

23. Mott N., *Trans. Faraday Soc*. 35 (1939), 1175

24. Fehlner F. and Mott N. *Oxid. Metals* 2 (1970), 59

25. Fromhold A. T. “Theory of Metal Oxidation” Vol. I-Fundamentals, North Holland, 1976

26. Helms C.R. and Deal B. “The Physics and Chemistry of SiO_2 and the Si-SiO_2 interface” Plenum Press, New York, 1988

27. Irene E. “Thermal oxidation of silicon: New experimental results and models” *Applied surface science* 30(1987) 1-16

28. Irene E. “ Thermionic emission model for the initial regime of Si oxidation” *Appl. Phys Lett* 51(10) (1987)

29. Kuznetsova A. , Zhou G. , Chen X. , Yang J. , Yates J. T., Jr., “Making a superior oxide corrosion passivation layer on Al using Ozone”, *Langmuir*, (2001), 17, p. 2146-2152

30. Ichimura S. Kurokawa A. Nakamura K. Itoh H. Nonaka H. Koike K. “Ultrathin SiO_2 film growth on Si by highly concentrated ozone” *Thin Solid Films* 377-378. 518-524 (2000)

31. Zachariasen W.H. “The Atomic Arrangement in Glass” *Journal of American Chemical Society,* 54, 3841-3850 (1932)

32. Mozzi R.L. and Warren B.E. “The Structure of Vitreous Silica” *Journal of applied Crystalogarphy* 2, 164-172 (1969)

33. Bell R.J. and Dean P. “The Structure of Vitreous Silica: Validity of the Random Network Theory” *Phil. Mag*. 25, 1381-1389 (1972)

34. Gerber T. and Himmel B. “The Structure of Silica Glass” *Journal of Non-Crystalline Solids*, 83, 324-334 (1986)

35. Wright A.C. “Diffraction Studies of Glass Structure” *Journal of Non-Crystalline solids* 123, 129-148 (1990)

36. Wright A.C. “The structure of amorphous Solids by X-ray and Neutron Diffraction” *Adv. Struc. Res. Diff. Meth.*, 5, 1-84 (1974)

37. Wright A.C. “Neutron Scattering from Vitreous Silica. The structure of Vitreous Silica: What Have We Learned from 60 Years of Diffraction Studies?” *Journal of Non-Crystalline Solids* 179, 84-115 (1994)

38. Narten A.H. “Diffraction Pattern and Structure of Non-crystalline BeF_2 and SiO_2 at 25^oC” *J. Chem. Phys.* 56 1905-1909 (1972)

39. Revesz A. *Phys. Stat. Sol*. 19 (1967), 193

40. http://www.unb.ca/courses/geol21142/LEC-31.html

41. Itoh H. Nakamura K. Kurokawa A. Ichimura S. "Initial oxidation process by ozone on Si(100) investigated by scanning tunneling microscopy". *Surface Science* 482-485. 114-120 (2001)

42. Caledonia G.E. Krech R.H. and Green B.D. "High flux source of energetic oxygen atoms for material degradation studies" *AIAA J*. 25, 59-63 (1987).

43. Oakes D.B. Krech R.H. Upschuete B.L. and Caledonia G.E. "Oxidation of polycrystalline silver films by hyperthermal oxygen atoms" *J.Appl. Phys*.77,2166-2172 (1995)

44. Popova I. Muha R. Chen Z. and Yates J. "Construction and Performance of a Low Energy Ion Gun" *J. Vac. Sci. Technol*. A 21, 401 (2003)

45. Takahagi T. and Nagai I. "The formation of hydrogen passivated silicon single-crystal surfaces using ultraviolet cleaning and HF etching" J. *Appl. Phys*. 64(7), 3516-3521 (1988)

46. Trucks G.W. Raghavachari K. Higashi Y. and Chabal Y. "Mechanism of HF etching of silicon surfaces: A theoretical understanding of hydrogen passivation" *Physical review Letters,* vol. 65 (4) (504-507) (1990)

47. Tromp R. Rubloff G. and Balk P. "High-Temperature SiO_2 decomposition at the Si/SiO_2 interface" *Physical Review Letters,* vol. 55(21) (2332-2335) 1985

48. Wentink D. Kuijper M. and Wormeester H. "Etching behavior of Si(100)-2x1 studied with optical anisotropy" *Physical Review B,* vol. 56(12) (7679-7686) 1997

49. http://www.mticrystal.com

50. Eaglsham D. Higashi G. and Cerullo M. "370 C clean for Si molecular beam epitaxy using HF dip". *Appl. Phys. Let*t. 59(6) 685-687 (1991)

51. Nakazawa M. Nishioka Y. Sekiyama H. and Kawaze S. "Investigation of the SiO_2/Si interface. II. Oxidation of an HF cleaned Si(100) surface using photoemission spectroscopy with synchrotron radiation" *J. Appl. Phys*. 65(10) 4019-4023 (1989)

52. Thompson P. Twigg M. Goodbey D. Hobart K. and Simons D. "Low temperature cleaning processes for Si molecular beam epitaxy" J. Vac. Sci. Technol. B 11(3) 1077-1082 (1993)

53. Higashi G. Becker R. Chabal Y. and Becker A. “Comparison of Si(111) surfaces prepared using aqueous solution of NH_4F versus HF” *Appl. Phys. Lett*. 58(15) 1656-1658 (1991)

54. Hollering R. Dijkkamp D. and van der Heide A. “Cleaning of Si(001) surfaces studied by optical second-harmonic generation and X-ray photoelectron spectroscopy” *J. Vac. Sci. Technol.* B9(4), (1967-1969) Jul/Aug 1991

55. Pic N. Glachant A. and Autran J. “Determination of the electrical properties of 2.5nm thick silicon-based dielectric films: thermally grown SiO_x” *Journal of Non-Crystalline Solids* 280 (69-77), 2001

56. Hanbucken M. Neddermeyer H. and Venables J. “Surface cleaning of Si(100) and Ag/Si(100): Characterization by SEM, AES and RHEED” *Surf. Sci. Lett*. 137 (L92-L96), 1984

57. Chu W. Mayer J. and Nicolet M. “Backscattering Spectrometry” Academic Press, New York, 1978

58. www.hongserver.com/specon

59. Thomas G. “Transmission Electron Microscopy of Materials” Willey and Sons (1981)

60. Fultz B. and Howe J. “Transmission Electron Microscopy and Diffractometry of Materials” Springer (2000)

61. Reimer L. “Transmission Electron Microscopy” 4th edition, *Springer* (1997)

62. Williams D. and Carter B. “Transmission Electron Microscopy” Plenum Press, New York, 1996

63. Tanaka N. Yamasaki J. Usuda K and Ikarashi U. “First observation of SiO_2/Si(100) interfaces by spherical aberration corrected high-resolution transmission electron microscope” *Journal of electron Microscopy* (52) 69-73 (2000)

64. Randjelovic M. and Yang J. C., “Structural comparisons of passivated Si(100) by atomic and molecular oxygen”, . *Materials at High. Temp.* , vol. 20,281-285, (2003).

65. Gatan Inc. (2002) “Digital Micrograph user’s guide”

66. Takeguchi M. Tanaka M. YasudaH. and Furuya K. “Real time high-resolution transmission electron microscopy observation of the growth process of (001) surfaces on a nanometer-sized Si multiply twinned particle”, *Surface Science* 493, (414-419) 2001

67. PCPDF files

68. Egerton R.F. (1996) “Electron Energy loss Spectroscopy in the electron microscope” 2nd edn. Plenum Press, New York and London

69. Gatan Inc. (2002) “Digital Micrograph EELS analyses user’s guide”

70. Ahn C. and Krivanek O.(1983) “EELS Atlas” Gatan Inc. and ASU HREM Facility

71. Hofer F. and Golob P.(1987) “ New examples for near-edge fine structures in electron energy loss spectroscopy” *Ultramicroscopy* (21) 379-384

72. Keast V. Scott A. and Brydson R. “ Electron energy-loss near- edge structure – a tool for the investigation of electronic structure on the nanometer scale” *Journal of Microscopy* 203(2) 135-175 (2001)

73. Auchterlonie G. McKenzie D. and Cockayne D. (1989) “Using ELNES with parralell EELS for differentiating between a-Si:X thin films” *Ultramicroscopy* 31 217-222

74. Garvie L. and Rez P. (2000) “Bonding in alpha-quartz (SiO_2): A view of the unoccupied states” *American Mineralogist* , 85, 732-738

75. Skiff W. Carpenter R. and Lin S.(1985) “ SiL core edge fine structure in an oxidation series of silicon compounds: A comparison of microelectron energy loss spectra with theory” *J. Appl. Phys*. 58(9) 3463-3469

76. Weng X. Rez P. and Batson P.(1990) “ Single electron calculations for the $SiL_{2,3}$ near edge structure” *Solid State Communications*, Vol 74, No.9 1013-1015

77. Batson P. “Silicon $L_{2,3}$ core adsorption obtained at the buried Al/Si(111) interface” *Physical Review B* 44 (15) 5556-5561

78. Ahn C. and Rez P.(1985) “Inner shell edge profiles in electron energy loss spectroscopy” *Ultramicroscopy* 17 105-116

79. Dori L. Bruley J. DiMaria D. and Batson P. “ Thin-oxide dual –electron –injector annealing studies using conductivity and electron energy loss spectroscopy” J. *App. Phys*. 69(4) 2317-2323 (1991)

80. Batson P. and Kavanagh K. "Local bonding and electronic structure obtained from electron energy loss scattering" *Ultramiscrocopy* 22 89-102 (1987)

81. Auerhammer J. and Rez P. and Hofer F. (1989) "A comparison of theoretical and experimental L and M cross sections" *Ultramicroscopy* 30 365-370

82. Li D. Bancroft G. and Feng X. (1993) " High –resolution SiK and $L_{2,3}$ –edge XANES of α-quartz and stishovite" *Solid State Commmunications* 87(7) 613-617

83. Garvie L.A.J. and Buseck P.R. "Bonding in silicates: Investigation of the SiL2,3 edge by parallel electron energy-loss spectroscopy" *American Mineralogist* 84, 946-964(1999)

84. Batson P.E. "Simultaneous STEM imaging and electron energy-loss spectroscopy with atomic-column sensitivity" *Nature* 366, 727-728 (1993)

85. Aoto N., Ikawa E., Endo N. and Kurogi Y. "In-depth profiling of the SiO_2/Si interface electronic structure using low-energy electron energy loss spectroscopy" *Surface Science* 234, 121-126 (1990)

86. Muller D. and Neaton J. "Evolution of the interfacial electronic structure during thermal oxidation" ed. Chabal Y. Fundamental aspects of silicon oxidation; *Springer*, New York, 2001

87. Cohen S. (ed) Atomic force microscopy/Scanning tunneling microscopy 2, Plenum Press, New York, 1997

88. Brundle R.(ed) "Encyclopedia of Materials Characterization" *Butterworth-Heinemann* 1992

89. Revesz A. and Evans R. "Kinetics and mechanism of thermal oxidation of silicon with special emphasis on impurity effects" *J. Phys. Chem. Solids* 30, 551-554, 1969

90. Uchiyama T. and Tsukada M. "Scanning-tunneling-microscopy images of oxygen adsorption on the Si(001) surface" *Phys. Rev.B* 55 (15) 9356, (1997)

91. Watanabe H. Kato K. Uda T. Fujita K. and Ichikawa M. "Kinetics of Initial Layer-by-Layer Oxidation of Si(001) Surfaces" *Phys. Rev. Lett.* 80, 345, 1998